University of Potsdam – Institute for Physics and Astronomy

Transits in the young system PTFO 8-8695, is there a planet?

Masterthesis

For the acquirement of the scientific degree
Master of Science (M.Sc.)
in the discipline Astrophysics

handed in by
S. Marzieh Hosseini
Student number: 790188

University of Potsdam

Leibniz-Institute for Astrophysics

Potsdam, April 29, 2021

Supervisor & first referee: Prof. Dr. Katja Poppenhäger
Second referee: Prof. Dr. Stefan Geier

"Somewhere, something incredible is waiting to be known."

– Carl Sagan

Abstract

Among the observed planet population, the intriguing class of close-in gas giants, also known as *hot Jupiters*, makes up about 10% of all confirmed planets. Understanding the formation and evolution of hot Jupiters is of great interest in exoplanet research particularly due to our solar system lacking any equivalents. Finding and studying young hot Jupiters provide the opportunity to study and understand the time scale of hot Jupiter's formation, which contributes notably to the solution of their mysterious formation process.

In this work, we study the young pre-main-sequence T Tauri star, PTFO 8-8695, which has been recognized as one of the first T Tauri stars with a planet candidate. This star exhibits transit events that were attributed to a putative hot Jupiter, PTFO 8-8695 b, with a period of 0.5 d and a mass of less than $5.5 M_{\mathrm{Jup}}$. However, its existence is still under debate. A Confirmation of the planetary origin of this signal would enable us to put constraints on the time scales of giant planet formation.

We present new observational data of this key system taken with the ground-based STELLar Activity telescope (STELLA) and the Las Cumbres Observatory (LCO). We combine these data with space-based observations of the Transiting Exoplanet Survey Satellite (TESS) and knowledge from past studies of the system for a comprehensive picture of the system.

We investigate whether the observed dips in brightness represent the occultation of the planet PTFO 8-8695 b by fitting a transit model with the available planetary parameter from literature. Additionally, we performed timing analysis to determine the phase of the observed dimming events. We report a transit in the LCO data that has similar properties to the reported flux dips in the literature, and transit model fitting yields a similar radius ratio to the one derived by Raetz et al. (2016). The timing analysis shows that the phase of the LCO transit is roughly half a period shifted from the originally reported dips.

Close inspection of the TESS data reveals that this system exhibits multiple dips with different properties. Additionally, one of the dips, despite its differences with the LCO dip otherwise, appears to be in phase with the LCO transit.

The phase shift of the LCO dip, the non-existence of a similar dip in the TESS data, and the lack of concrete evidence for the existence of the planet in the previous papers and our data show that the existence of PTFO 8-8695 b is improbable. By comparing the observed dips in the LCO and TESS data with the other reported ones from the literature, we found similarities between the brightness dips in our data to those that have been attributed to dust clumps and accretion hotspots.

Despite this, non of the proposed scenarios can describe the observed phenomena to full extent. Based on the present facts and dip properties, we suggest that the dips are most likely due to the warm gas clouds that are co-rotating with the star.

Contents

1 Introduction

The universe we are living in is full of mysteries and its vastness confronts us with open questions. One of the most profound and interesting questions humans have ever asked is whether we are alone in the universe. For many years philosophers and curious scientists have asked similar questions, whether our earth is the only planet that is able to support life in the way we know it. In recent years with the advancements and innovations in satellite and telescope technologies, we can explore the universe more deeply and answer these questions with scientific tools and observations. During the last decades, tremendous effort and research have been done to discover and study planets. The launch of several satellites, such as TESS or Kepler, resulted to discovery of thousands of planets which paved the path for us to study exoplanets and their diversity. Since we can establish today that planets are a common occurrence in the universe, the scientific questions from above have boiled down to these three key topics of interests: (1) How do planets form and evolve? (2) What is the diversity of planetary systems and their architectures? (3) Can we find habitable planets with signs of biosignatures and life ?

Thanks to the fast pace of discoveries and innovations, we are able, for the first time in human history, to find answers to these questions.

1.1 Extrasolar Planets

The exciting field of extra-solar planets started approximately 30 years ago with the discovery of the first planet outside of our solar system, called "exoplanet", around a pulsar, the remnant of a massive star. In 1992, radio astronomers found periodic variations in the radio signals of the pulsar PSR1257+12, located in the Virgo constellation. They attributed those periodic variations to the orbital motion of two small Earth-sized planets with masses of $2.8\,M_\oplus$ and $3.4\,M_\oplus$ around the central pulsar (Wolszczan & Frail 1992). It is surprising and still not fully known how planets can form and survive in this exotic environment since they are bombarded with deadly particles and emissions from the pulsar most of the time, let alone surviving the collapse of the massive star to a pulsar.

A few years later in 1995, Michel Mayor, the 2019 Physics Nobel Prize winner, by monitoring radial velocities of more than hundreds of dwarf stars, found radial velocity variations in the system 51 Peg. His team discovered that those variations are due to a gas giant planet with a mass close to Jupiter's mass in a very close-in orbit with an orbital period of 4.3 days (Mayor & Queloz 1995). Note that the mass of gas giants is commonly given in Jupiter masses, M_{Jup}. 51 Peg b, so the planet's name[1], is the first giant planet discovered around a sun-like star and belongs to the class of hot Jupiters, a type of gas giants with a mass greater than $0.25\,M_{\mathrm{Jup}}$ and orbital periods shorter than 10 days (Dawson & Johnson 2018). They are called hot Jupiters because these planets are in short orbits and close to the star, making them hot from the star's radiation.

Our understanding of planet's formation was limited to our solar system before the detection of 51 Peg b. In the solar system, four rocky planets are located in inner regions whereas the other four ice/gas giants orbit further out on almost circular orbits. The discovery of 51 Peg b with an orbit closer than 1 AU with other discovered hot Jupiters, shows that our understanding of planet formation requires revision.

In recent years, with the launch of several planet-hunting missions such as Kepler, TESS, and the HIRES survey, scientists discovered more than 4300^2 exoplanets with different masses, orbital parameters, and characteristics; showing the great diversity in the exoplanet zoo.

Among the discovered exoplanets, hot Jupiters are relatively rare, makeup only 10% of the discovered exoplanets. Among this class, only 0.4% orbit around stars with spectral type of F, G and K (Zhou et al. 2019).

Despite that, hot Jupiters are easy to detect with radial velocity and transit methods due to their high mass and short period. This led to the rapid discovery and confirmation of the hot Jupiters in the last decade and resulted in a statistic sample of exoplanets which enables astronomers to study their mass distribution and planet-metallicity correlation (Dawson & Johnson 2018). This shows these objects play important role in the field of exoplanets.

However, their formation is still not fully known and its not clear how they have formed in their close-in orbits with their high mass and large radii. One of the suggested explanations is that they have formed further out and migrated closer to the star. Nevertheless, there are several scenarios for their formation which will be reviewed in the section 1.3.

---

[1]Note that planets are enumerated with lower case letter, starting always with *b*.
[2]Nasa Exoplanet archive `https://exoplanetarchive.ipac.caltech.edu` (01.03.2021)

1.2 Detection Methods

In recent years, scientists developed several techniques for finding and characterizing exoplanets. Most of the methods for detecting exoplanets rely on the effect of the planet on its host star. Therefore, by observing and measuring the effect, one can infer information about the existence of the planet. The detection of planets is in principle easy but practically very challenging due to the necessity of extreme precision. Generally speaking, there are three commonly used indirect methods to detect exoplanets: the transit method, the radial velocity method, and astrometry. Most of the discovered planets so far have been discovered through those indirect methods. Because most of the planets are so close to their host star and much fainter compared to it, they are invisible for direct detection. The detectability of planets by indirect methods depends mostly on the instrumentation's capabilities.

Direct methods for detection of exoplanets allow scientists to study aspects of exoplanets that are not accessible in other ways. These methods include direct imaging and optical interferometry. In the following sections, we briefly review the main indirect and direct detection methods as well as their limitations.

1.2.1 Radial Velocity Method

Since the detection of 51 Peg b with the radial velocity method in 1995, more than 800^3 exoplanets have been confirmed with this method so far. This shows that the majority of the exoplanets have been detected through the radial velocity method (also known as Doppler spectroscopy) with ground-based telescopes and it plays an important role in the characterization of exoplanets. Additionally, this technique has been very effective in measuring masses and orbital periods of planets with Earth or Jupiter masses in close orbits.

The fundamental idea behind this method is simple. When a planet orbits around a star, the host star does not remain static but both, star and planet, wobble around their common center of mass. Even though the planet is much smaller in mass, it exerts a gravitational torque on the star, causing it to move slightly.

The important parameter in this technique, the velocity component parallel to the line of sight, can be detected as a wavelength shift, $\Delta\lambda = \lambda \cdot v/c$, in the stellar spectrum, analogously to Doppler spectroscopy. The observed radial velocity amplitude, K, can be expressed as:

$$K[\text{cm s}^{-1}] = \frac{8.95\,\text{cm s}^{-1}}{\sqrt{(1-e^2)}} \frac{M_P \cdot \sin i}{M_\oplus} \left(\frac{M_* + M_p}{M_\odot}\right)^{-2/3} \left(\frac{P}{\text{yr}}\right)^{-1/3} \tag{1}$$

By combining the measurable radial velocity amplitude with other inferred planetary parameters such as the eccentricity e, orbital period P, and the mass of the star M_*, the lower limit on the mass of the planet, $M_p \sin i$ can be derived. As mentioned before, astronomers by using the radial velocity method, revealed the existence of 51 Peg b around its sun-like star. 51 Peg star's radial velocity curve is displayed in Fig. 1.

This method is used more for close-in planets since the gravitational force between star and planet decreases with the square of the distance ($1/r^2$). Also, following Eq. (1), when orbital periods are short, the amplitude is higher, which makes it easier to detect planets with short periods. However, there are several challenges to find exoplanets with this method, especially around young and active stars. Several astrophysical phenomena are occurring inside or outside of the host star that can add noise to radial velocity measurements. Thus, detailed knowledge about these processes are essential for the detection of planets in active systems.

Magnetic fields of young and active stars, mostly solar-type stars or M dwarfs, cause spots on the surface of these stars. In the spot regions, there is a flux deficit that will become blue-shifted and red-shifted as the star rotates. This effects changes the shape of the spectral line differently across the stellar surface and therefore produces modulation in the radial velocity measurements (Boss 1997). Another important phenomena affecting radial velocity measurements are p-mode oscillations caused by convective motions that occur in stars with an outer convection layer (i.e. FGKM stars). Each mode has a radial velocity amplitude of several decimeters per second. The superposition of these modes can change the observable radial velocity up to several meters per second (Lovis & Fischer 2010).

1.2.2 Transit Method

One of the fundamental and obvious methods to detect small planets around stars is the transit method. Like the radial velocity method, this method is efficient for finding short period and close-in planets. Simply put, this technique is about observing stars photometrically over an extended period of time and searching for small dips in their brightness that repeat periodically. Those small dips are caused by an object (in this case the planet) obscuring parts of the stellar disk. They convey information about the planet and its orbital geometry. Most of the discovered planets (namely about 3300^4) today have been detected with
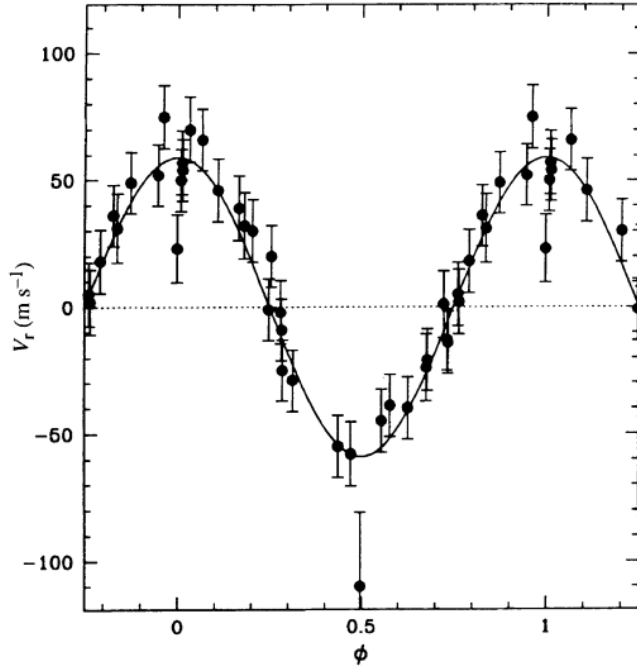

Figure 1: Radial velocity's variations of 51 Peg, caused by the hot Jupiter 51 Peg b. The planet has the lower mass limit of $0.47\,M_{\mathrm{Jup}}$, a period of 4.231 days, and a radial velocity amplitude of $59\,\mathrm{m\,s^{-1}}$. Numbers and figure taken from (Wolszczan & Frail 1992).

this method. However, there are difficulties in confirming planets with this method alone. False positives are one of the common problems. Examples of other objects that can cause transit like dips are eclipsing binaries, occultation by brown dwarf, sub-stellar objects with radii similar to gas giants. One possible way to overcome this problem is by doing follow-up radial velocity observations.

To have some general understanding of the basics of the transit method, we will describe it briefly. A transit occurs when the planet moves in front of the star and blocks the stellar flux. A schematic display on the example of WASP 1b is displayed in Fig. 2. The drop in the received flux is visible in the light curve (time series of photometric measurements) and is proportional to ΔF which is related to the radii of planet R_p and star R_* as:

$$\Delta F \propto \left(\frac{R_p}{R_*}\right)^2.$$
(2)

When the planet starts to occult the star, a small fraction of the total area of the planet blocks the light. This fraction becomes gradually larger while the planet is moving in. In Fig. 2, this corresponds to the time between points 1 and 2. This causes a steep decline in the brightness, corresponding to the relative area of the star that is blocked. When the planet is entirely in front of the star, this steep decline stops. The duration between points 1 and 5 is total transit duration T which will be described briefly after this part.

A transit is usually described by three parameters, the duration of transit T the depth of transit, and the shape of transit. Generally, the shape of the transit in the light curve depends on the properties of the planet, the star, and the orbit. The duration of the transit T for a circular orbit can be expressed as:

$$T \approx \frac{PR_*}{\pi a}\sqrt{\left(1+\frac{R_p}{R_*}\right)^2 - \left(\frac{a}{R_*}\cdot\cos i\right)^2}$$
(3)

and it depends on the star's radius R_*, the orbital period of the planet P, planet's radius R_*, semi-major axis of the planetary orbit, a and the impact parameter, b. the projected distance of the planet's center to the star's equator, b, is given by $b = a/R_* \cdot \cos i$. Accordingly, in the case of a high impact parameter, the duration of the transit will decrease which makes the shape of transit looks more V-shape, similar to the eclipses we see in eclipsing binary stars.

Another crucial parameter that affects the shape of a transit is limb darkening, the effect that a a star is brighter in the center than at the edges. Limb darkening changes the shape of the transit, making it more rounded in the outer bottom parts. It also affects the transit depth, which means the transit depth is slightly deeper than the radius ratio in the case of limb darkening. Scientists infer planetary parameters by
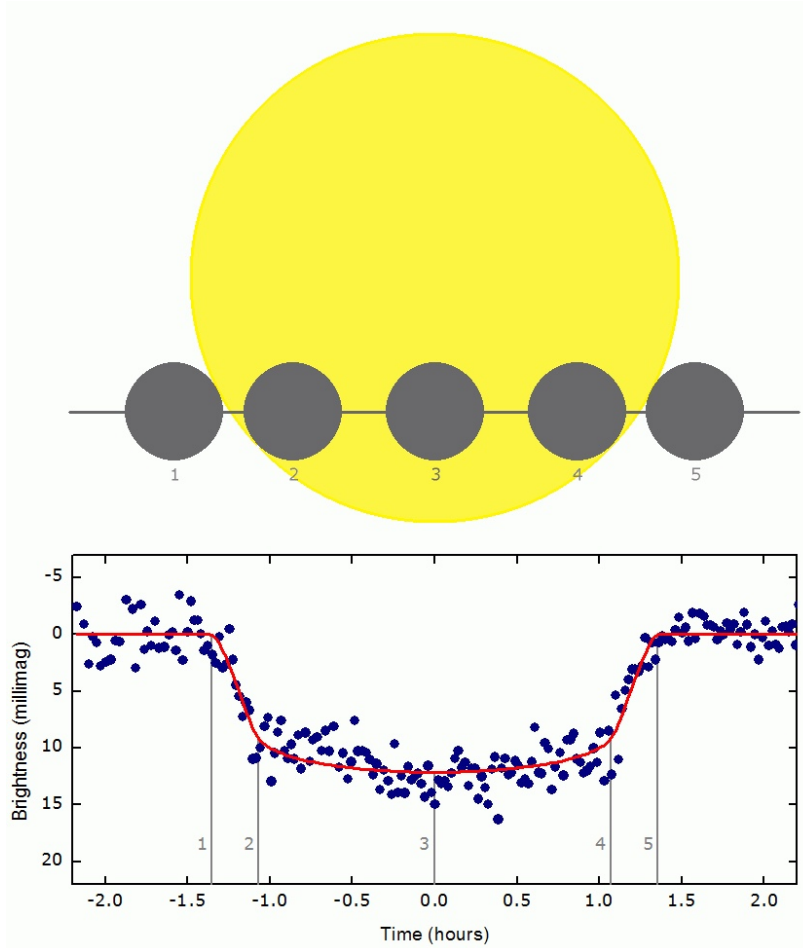
Figure 2: Transit of the Wasp-1b system with an illustration of how the shape of the dip is dependent on the phase of the transit. Image credit: Observatory Jena.

fitting a transit model to the observed light curves. Usually, they set certain planetary parameters as free and others as fixed in the model.

1.2.3 Gravitational Microlensing Method

One of the predictions of Einstein's theory of general relativity is gravitational lensing. In this phenomenon, the light emitted from distant stars bends due to a massive object between background star and the observer. This leads to a magnification of the background star and formation of multiple images of the background source (Mao & Paczynski 1991). In gravitational microlensing, when a compact object or a star passes in front of (in the proper alignment) a distant background star act as a lens, magnify the source and form multiple images of the background object.

However, compared to strong and weak gravitational lensing, in which the lens is massive galaxies or cluster of galaxies, in microlensing the mass of the lensing object is relatively small, in the range of 10^{-6} $\leqslant$ m/M$_\odot$ $\leqslant 10^6$. Thus, the separation between formed images which depends on the lens mass and the geometry is very small and not in the range of the resolution power of the the current telescopes. Therefore, instead of directly studying the formed images, astronomers look for the variation of the brightness of the source over the period of few weeks due to the moving lens in between the source and the observer.

When a lensing object passes the source-earth line of sight, the source brightness increases up to a point and then slowly decreases over a period of few weeks. If the lens is a single and compact object, the light curve of the microlensing events symmetric and simple. But if the lens is of a more complex shape, such as a binary star or a planet-hosting star and the companion is located at the right place, it can act as an additional lens and form an additional image. As a result, we see a small modulation in the apparent brightness of the source which is detectable in the light curve of the source. Fig. 3, shows an example of the event and the brightness modulation caused by the planet.

The parameter that can be inferred from the light curve is the mass ratio between the planet and the host star, $q \approx M_p/M_*$, as well as the angular separation between the star and the planet during the time

4
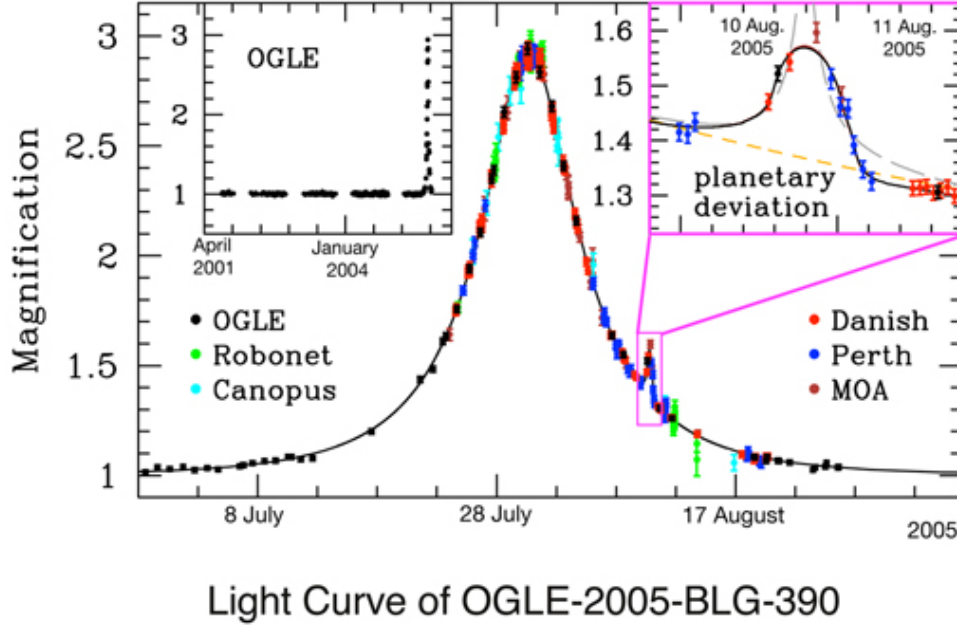
Figure 3: The effect of the planet on the light curve of the star-planet system OGLE–2005-BLG-390LB. The plot indicates a microlensing event with a peak on July 31, 2005, and the small deviation on 10th August indicates the presence of the planet. Image credit: ESO

of the lensing event, $d \approx \theta_{*,p}/\theta_E$ in units of Einstein's radius. The intrinsic mass of the planet cannot be inferred by this method, only in combination with a known stellar mass.

One of the advantages of this method is that it can be used for detecting planets at large distances and even other galaxies in the universe that are not accessible to other methods. Additionally, compared to other methods, gravitational microlensing is more sensitive to small and Earth-sized planets. On the other side, detecting the small modulation in the light curve is very tricky since one might miss it due to inappropriate observation conditions or poor timing. Also, this method is very costly because for detecting one microlensing event, monitoring millions of stars is required. Additionally, since the discovered planets are so distant, the possibilities of follow-up observations with other methods or determining the host star's parameters are challenging. Despite all the challenges, astronomers have discovered today about 100 exoplanets[5] with this method. However, the number will significantly increase with the launch of new and more advanced space-based and ground-based telescopes in the future such as Nancy Grace Roman Space Telescope (previously known as WFIRST) which will launch in 2025.

1.2.4 Astrometry Method

Another old and efficient method to detects planets is astrometry which is based on the same principle as the radial velocity method. As explained before, when there is a object or planet around a star, the star wobbles around common center of mass. By precise measurements of the star's position, we can trace the motion of the star relative to the sky background due to the wobbling motion. This method can be used for systems in which the planet's orbital plane is face-on or perpendicular to the line of sight of the observer.

The amplitude of the astrometric motion α of a star due to a an orbiting planet with mass of M_p, in micro arcseconds is given by:

$$\alpha = 3 \left(\frac{M_p}{M_\oplus} \right) \left(\frac{a_p}{1\text{AU}} \right) \left(\frac{M_*}{M_\odot} \right)^{-1} \left(\frac{D}{1\text{pc}} \right)^{-1} \tag{4}$$

Accordingly, the amplitude increases when orbital period and the mass of the planet increases. But the amplitude decreases with an increase in the distance and star's mass. Therefore, this method provides the possibility to detect Jupiter-mass planets in wide orbits. One of the advantages of this method is that we

---

[5]Nasa Exoplanet archive `https://exoplanetarchive.ipac.caltech.edu` (01.03.2021)

can infer the precise and true mass of the planet. This is not possible via other methods like transit or radial velocity that just provides constrains on the planet's minimum mass.

To have an idea on the limitation and possibility of detecting exoplanets with this method with available surveys, assume a $10 M_{\text{Jup}}$ planet in an orbit of $100\,\text{d}$ around a $1 M_\odot$ star at the distance of $10\,\text{pc}$. The amplitude of the astrometric shift is about 0.4 mas. This shows that the precision we need with this technique to measure the motion of stars relative to the sky background is $\leqslant 1\,\text{mas}$. However, current astrometric surveys, like the Hipparcos mission, which is one of the biggest astrometric surveys, can detect motions with amplitudes at the order of $\sim 1\,\text{mas}$. Also, the Gaia spacecraft which has the mission to perform astrometry for about 2000 million stars, can resolve a double stars that are $\sim 0.1\,\text{arcsec}$ apart. Thus, achieving the required for detection of planets is challenging and today we have detected only one exoplanet[6] with this method.

Nonetheless, this method can be used for follow-up observations and gathering additional information about the systems that has been discovered by other methods.

1.2.5 Direct Imaging Method

One of the exciting and important methods to detect exoplanets is through direct imaging. It enables us to have a more comprehensive picture of exoplanets and confirms their existence straightaway. While other methods, such as radial velocity or transit detection, can be used for planets in edge-one and small orbits, direct imaging can be effectively used for the detection of giant planets with masses greater than few Jupiter masses in wide orbits with a semi-major axis of $> 5\,\text{AU}$ (Fischer et al. 2014). One example is shown in Fig. 4, where a Jupiter-like planet with the mass of $5 M_{\text{Jup}}$ is orbiting around a brown dwarf at a distance of $55\,\text{AU}$ that was discovered with this method by Chauvin et al. (2005). As labeled in the image, the angular distance between the star and the planet is about $778\,\text{mas}$ and the planet is bright due to its thermal flux in the Infrared.
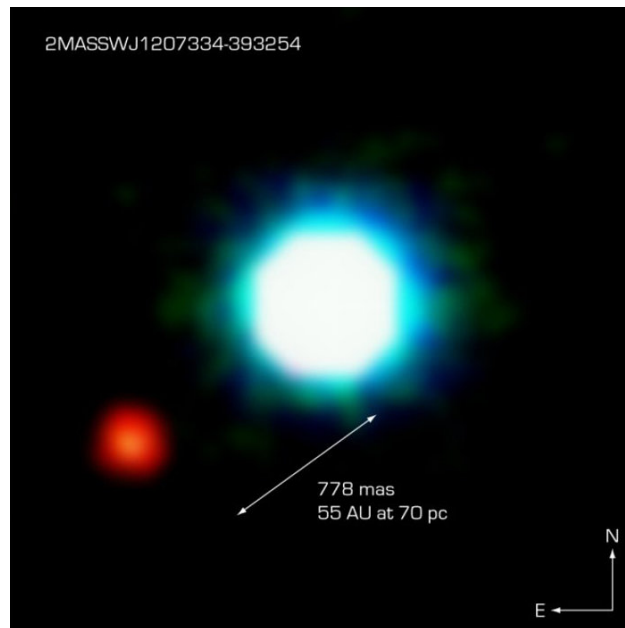

Figure 4: The first image of a Jupiter-like planet outside of our solar system orbiting a brown dwarf at a distance of $230\,\text{ly}$. The star, 2M1207, is the bright white spot in the center, and the orbiting planet is the fainter red spot to the left. The planetary companion is at a distance of $55\,\text{AU}$ from the star. This photo is created out of three near-infrared exposures (in the H, K, and L'' wavebands) with the NACO adaptive-optics facility at the $8.2\,\text{m}$ VLT Yepun telescope at the ESO Paranal Observatory. Image credit: ESO.

This technique is one of the most efficient methods in terms of observations because it requires only 2 observations separated by few months whereas in other methods we need several observations that cover several orbital periods. However, there are problems with this method. The first obvious problem is that exoplanets are very faint compared to the host star. They are about 10^6 to 10^{12} times fainter than the host star which makes it hard to distinguish them. Additionally, we not only have to overcome the strong brightness difference between the star and the planet but also for the planetary orbit, which even for the

---

[6]Nasa Exoplanet archive `https://exoplanetarchive.ipac.caltech.edu` (01.03.2021)

closest stars, is usually within one arcsec. Here one encounters the diffraction limit ($\theta \approx \lambda/D$, where D is the diameter of the primary mirror) of most telescopes if star and planet are to be resolved as individual objects. This means only telescopes with the largest aperture sizes ($> 8\,\mathrm{m}$) can be used for successful detection. Moreover, atmospheric effects, such as seeing, are a problem as well since we need high-resolution images of the star to identify the planet. Interferometry can solve the first problem due to its higher resolution power compared to normal telescopes. This is because the resolution power depends on the distance between the telescopes and not the diameter of the primary mirror. One example of high resolution by this method is the Gravity instrument which can resolve objects with 2 mas resolution. The relative proximity between host and planet (< 1 arcsec) does also show why the use of interferometry is required for such an observation. The second challenge can be overcome with adaptive optics which corrects for the atmospheric effects on the stellar light. Also, observing objects with space-based telescopes instead of ground-based telescopes can be a good option since the effect of the Earth atmosphere will disappear. After all, the future for this technique is very bright since with innovations and progresses in high-resolution imaging, interferometric instruments, and the launch of several surveys like Habitable Exoplanet Imaging Mission (HabEx) or Exo-Earth interferometer, we will have the possibility to have very high-resolution images of exoplanets and study their structure and atmosphere in great details.

1.3   Planet Formation scenarios

It is broad consensus that planets form in the circumstellar disk around a young star, which is the remnant of the star's formation. However, there are two main scenarios for the formation of giant planets in the disk, the core accretion model and the gravitational instability model. The core accretion model proposes the formation of the rocky core through coagulation of planetesimals (solid objects made of dust, rock, and other materials) to the point that it is massive enough ($\gtrsim 10 M_\oplus$) to accrete a gaseous envelope. This is the preferred scenario for the formation of the planets nowadays. See the works of, e.g., Lissauer (1993), Pollack et al. (1996), and Safronov (1972) for a more detailed discussion of this method.

In the gravitational instability model, the giant planets form due to a local gravitational instability in the proto-planetary disk. In regions of the proto-planetary disk where it is cool or massive enough, a gravitational instability can occur and clumps of gas form, which might lead to the formation of gas giants. For more details on this method, see the descriptions of e.g., Boss (1997) and Alibert & Helled (2015). For each of these scenarios, there are supportive evidence and problems as well. However, the formation of hot Jupiters in their close-in orbit can not be explained fully by either of the mentioned scenarios.

Three different classes of mechanisms have been proposed for the origin of hot Jupiter: in situ formation (Bodenheimer et al. 2000), disk migration (Goldreich & Tremaine 1980), and high eccentricity tidal migration. Further discussion of the details of these mechanisms is beyond the scope of this work. However, one important point is the time scale in which planets might form through one of the mentioned scenarios. In the core accretion scenario, the core formation and development of an envelope is expected to take about ~ 10 Myr (Pollack et al. 1996), whereas in the instability scenario, the planets may form within ~ 0.1 Myr (Bodenheimer et al. 2000). Therefore, finding and detecting planets in young systems with disk might help to reveal more about the planet formation. Young T Tauri stars, named after the prototype young star T Tauri in the Taurus star-forming region, are a class of stars in the pre-main-sequence (PMS) phase with an age younger than 10 million years. These stars often have proto-planetary disks, which makes them good candidates for exploring the early phases of planet formation. Detecting young planets in these systems will help to constrain the limits for the time-scales of planet formation and migration. However, due to enhanced stellar activity and planet-mimicking dust features, unambiguously detecting an infant planet around these young disk-bearing stars is difficult. In this work, we explore such a system and investigate the origin of transit signals that may or may not be caused by a hot Jupiter.

2 The young stellar system PTFO 8-8695

Among the various stellar associations in the night sky, the Orion OB1 Associations located at a distance of roughly 400 pc is one of the best-studied associations due to its ongoing star formation and proximity. It is home to stars in different star formation stages and studying it can give us a wealth of information about stars of different ages and populations. Therefore, it has caught a lot of attention in recent years and there have been several surveys to study a wide range of stars located there, from low mass stars with young ages ($\approx 1\,\mathrm{Myr}$) to older ones ($\approx 10\,\mathrm{Myr}$). A skymap with an overview of the dominant subregions in Orion OB1 is shown in Fig. 5.
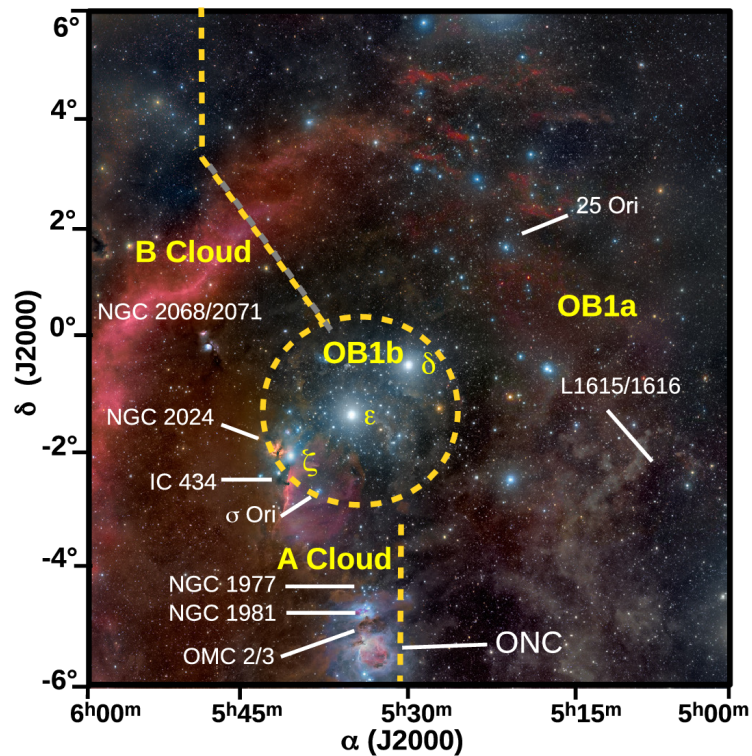

Figure 5: Deep sky image in the optical of the Orion OB1 association with its individual components labeled. The region includes the famous Orion Nebula (M45, bottom) and the δ, η, ζOri, which mark the Belt of Orion (encircled). Figure taken from Briceno et al. (2018).

Among the surveys focused on this region was the Cida Variability Survey of Orion OB1 (CVSO) which was a large optical survey aimed to identify, study, and monitor the low mass star ($\leqslant 1 M\odot$) population in Orion OB1 around the age range of $1-20\,\mathrm{Myr}$ (Briceño et al. 2005). This survey led to the discovery of PTFO8-86995, originally named CSVO30 after their catalog entry, located at 25 Orion-OB1a region (upper right in the figure). This object was identified as a very young and active pre-main-sequence (PMS) T Tauri star. An overview of its fundamental stellar parameters is given in Table 1.

In the next sections we review the studies that have investigated this system, both from planetary and non planetary point of view. However, since during the scientific work of this thesis, several new studies about this star have been published, we include them as well. These new findings will be discussed in the sections 2.2.3 and 2.3.

2.1 Indications for planetary hypothesis

We note that in the following text, we will use the terms *dimming event* and *fading event* interchangeably, always orientating us on the language used in the individual work referenced.

PTFO 8-8695 was monitored by the PTF project for 2 years, starting from December 2009, as part of a study to find young exoplanets in the Orion-OB1 region (van Eyken et al. 2012). It was observed once from December 2009 to January 2010 with Palomar 48" Samuel Oschin telescope which yielded 14 non-consecutive nights of usable data and a second time in December 2010 which resulted in 7 non-consecutive clear nights worth of data. All of the images were taken in the R band and have a typical cadence of $70-90\,\mathrm{s}$.

By using these observations and carefully analyzing the star's light curve, van Eyken et al. (2012) noticed a quasi-periodic variability in the light curve of the star with a period of $\approx 0.45\,\mathrm{d}$ which they attributed to

Table 1: Stellar parameters and magnitudes of PTFO 8-8695 as identified in different studies.

Parameter	Unit	Value	Reference
Spectral Type		M3	1
Sub-class		WTTS	1
T_{eff}	[K]	3470	1
R_*	$[R_\odot]$	1.39	1
M_* (Baraffe/Siesse)	$[M_\odot]$	0.44/0.34	1
$v\sin i$	[km s^{-1}]	80.6 ± 8.1	2
Distance	[pc]	323^{+233}_{-96}	1
Age	[Myr]	2.6	1
V	[mag]	16.26	1
R	[mag]	15.19	2
I	[mag]	13.74	2
J	[mag]	12.232 ± 0.028	3
H	[mag]	11.559 ± 0.026	3
K	[mag]	11.357 ± 0.021	3

References: (1) Briceño et al. (2005); (2) van Eyken et al. (2012); (3) Skrutskie et al. (2006)

Notes: The two different stellar masses are derived based on two different stellar evolution models, Baraffe et al. (1998) and Siess et al. (2000), by Briceño et al. (2005).

the spot-modulation signal of the star from its rotation. Additionally, there exists periodic events in the light curve which were superimposed on the quasi-periodic stellar variability of this system. The derived duration and period of dimming events to be $\approx 2\,$h and $\approx 0.45\,$d, respectively. We note that the supposed spot-modulation and the dimming events occur at almost the same period. However, their periods are very much not identical.

In February 2011, the star was observed with the Las Cumbres Observatory Global Telescope Network (LCOGT) which resulted in higher quality observations and the data was used for confirmation of the previous year's detection of a periodic dimming event.

But the system seemed to have its mysteries to itself: van Eyken et al. (2012) found in the PTF data that the transit shapes are changing over the 2 years of monitoring. The transit events in the 2009 data had a flat bottom shape and were longer in duration, whereas transit shapes changes to a U-shape in the 2010 data. Additionally, the transit events didn't occur at the predicted time according to the period of dimming events or even disappeared in some intervals of time. In Fig. 7, we show three different recorded transit events over the span of roughly a year. The predicted time of transit is highlighted in gray and it can be seen that the left panel does not show a transit.
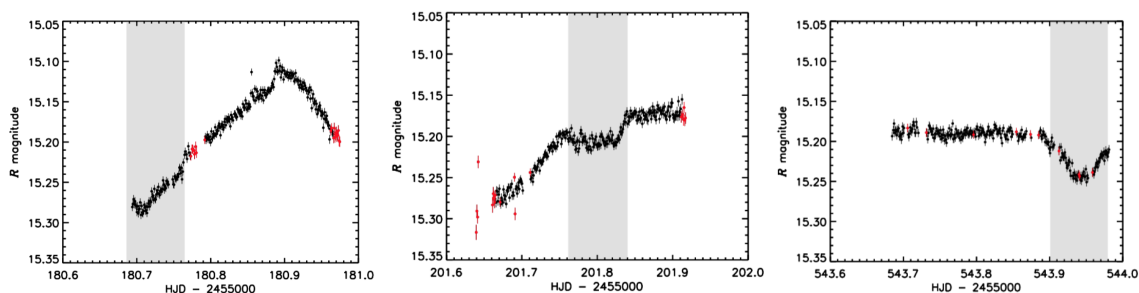

Figure 6: Three light curves from the PTF survey of . Highlighted in gray are regions of a predicted transit. The middle and right panel show a transit at the predicted time, whereas there is no transit at the right time in the left panel. Figure taken from van Eyken et al. (2012).

They examined whether there is the possibility of existence of a binary star in the system that could cause the observed dips. Thus they captured adaptive optic images of the star by using the NIRC2 camera on the 10 Keck II telescope and they found no star that has the proper magnitude to cause the observed dips with depth of 3.0% to 4.0% in the proximity. However, they mentioned that if there is any binary closer than 0.25", it would have been beyond the detection limit of the used instrument. Furthermore, they performed spectroscopy with the high-resolution spectrograph HIRES, mounted at the Keck telescope and measured the radial velocity (RV) amplitude of 2.4 km s^{-1} from the spectra. We know that the RV amplitude scales

with the mass of the companion and if the measured signal would be due to a stellar object, the amplitude of the RV signal would be higher. Therefore, they estimated the possible amplitudes for two example stars with different masses to see if the RV is due to a binary star rather than a planet. Their estimation of a RV curve for a $13\,M_{\mathrm{Jup}}$ object with deuterium-burning core or a slightly more massive brown dwarf star with a mass of $25\,M_{\mathrm{Jup}}$ lead to the range of $5.7\,\mathrm{km\,s^{-1}}$ to $11\,\mathrm{km\,s^{-1}}$. This is significantly larger than the measured value of $2.4\,\mathrm{km\,s^{-1}}$. With that, they concluded, a putative transiting object would be of planet size.

In order to obtain planetary parameters, they fitted a transit model to the light curves and the resulting fit is displayed in Fig. 7. The orbital inclination i, the star-to-planet radius ratio k, and the limb darkening coefficients were set as free parameters for the fit. From the resulting parameter they derived a semi-major axis of the orbit $a = 1.80 R_{\odot}$ and an orbital inclination of $i = 61.8^{\circ} \pm 3.7^{\circ}$. Additionally, combining the RV amplitude with the derived inclination yields an upper mass limit of $M_p \leqslant (5.5 \pm 1.4) M_{\mathrm{Jup}}$. We note one important caveat, their found fit did not match the data for second year of observation. They argued that a fit to the second year yields similar parameter for the transit. However, the fit predicts a stellar radius about $10\,\%$ smaller.
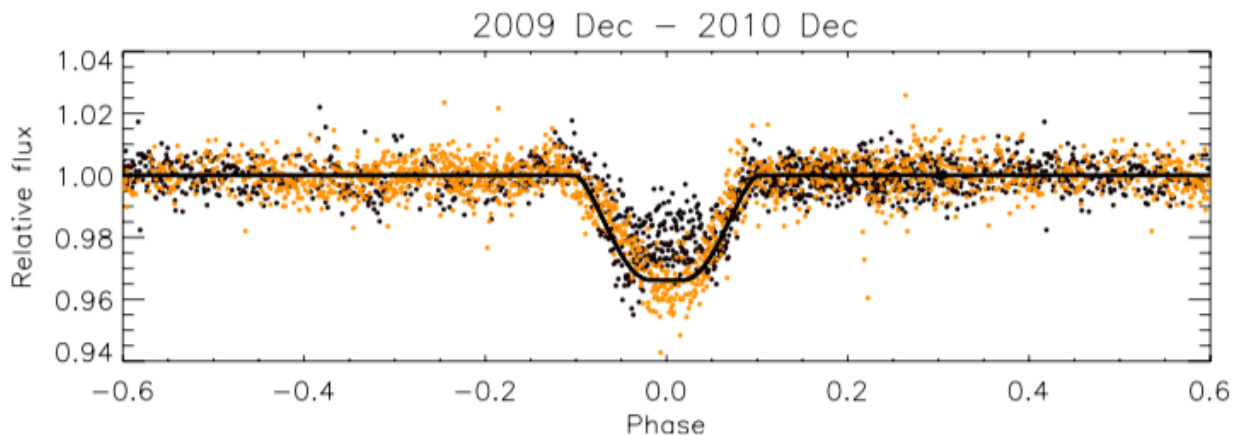

Figure 7: Phase folded light curve of with the period of $P = 0.448413\,\mathrm{d}$ based on the PTF data. The orange dots corresponds to the data from the first year (Dec. 2009 to Jan. 2010) and the black dots are data from Dec. 2010. The change in the overall shape of transit during 2 years is evident. Overplotted as black line is the transit fit to the first year's data. Figure taken from van Eyken et al. (2012).

To derive the period of the putative planet more accurately, they performed Fourier analysis on the data and created a periodogram in which they identified one peak at $0.448413\,\mathrm{d}$. Furthermore, they found two more periodic signals in their periodogram at $0.4481\,\mathrm{d}$ and $0.9985\,\mathrm{d}$, which they attributed to spot modulation period and an artifact from observations, respectively. Given the proximity of putative planet and star, they estimated the Roche radius of the planet to see if the planet radius exceeds it and mass transfer would occur. They calculated $R_{\mathrm{Roche}} \approx 1.92 R_{\mathrm{Jup}}$ which is nearly identical to the found planetary radius of $R_P = 1.91 R_{\mathrm{Jup}}$. This means that the planet would fill its Roche volume and may have undergone mass loss in the past due to Roche-lobe overflow. Additionally, they note a misalignment between the putative planet orbital inclination and the stellar inclination, suggesting a possible misalignment in the system. They argued that this misalignment could explain the changes in the transit shape, assuming the planet to be on a precessing orbit around a gravity-darkened star.

Barnes et al. (2013) investigated this possibility further by fitting the theoretical model on the photometric data taken by van Eyken et al. (2012). They developed a theoretical model for a hot Jupiter with the assumptions that (1) there is a misalignment between the planet's orbit and the star's equatorial plane which causes orbital nodal precession, (2) the planet and the star both have similar angular momentum magnitudes, and (3) star is a gravity-darkened object. Latter is argued because, according to them, a gravity-darkened star that rotates fast enough to show oblateness have brighter poles and dimmer equatorial regions. Hence, the traverse of the planet across different regions of this stellar disk might result in different asymmetric transits or the disappearance of transits. They aimed to explain all data simultaneously with the created model and tested a wide range of parameters, once for a stellar mass of $M_* = 0.34 M_{\odot}$ and once for a stellar mass of $M_* = 0.44 M_{\odot}$. The fit that explains the observed data was found for both masses which yielded precessing periods of $293\,\mathrm{d}$, and $581\,\mathrm{d}$, respectively. However, they note that they were only able to find a solution that assumes a stellar radius of $R_* = 1.03 R_{\odot}$ in both cases.

Another important study of this system by Ciardi et al. (2015) reveals more interesting facts. They monitored the system with different telescopes to confirm the planetary nature of the observed transits and detect the secondary eclipse of the sub-stellar object. Their data consists of observations with the Spitzer

Space Telescope, KECK-II NIRSPEC, and the LCOGT telescope network between Apr. 2012 and Nov. 2013 in the r' filter. They were able to detect one transit in the SPITZER data at the time close to the predicted time by the van Eyken et al. (2012) ephemeris, see left panels in Fig. 8. However, the transit depth was just 0.6%.
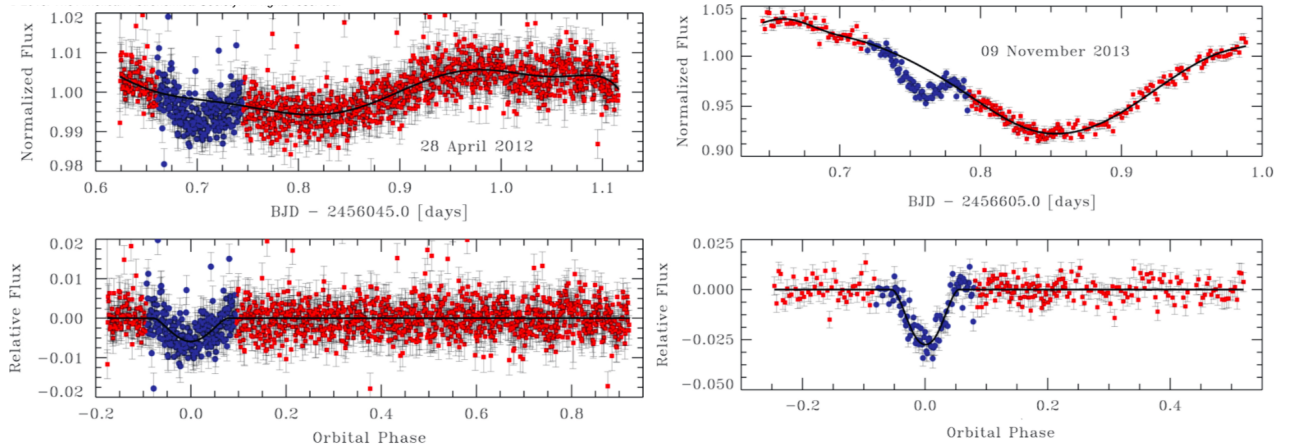

Figure 8: Spitzer IRAC4 $4.5\,\mu$m (left panels) and LCOGT (right panels) light curves taken from of at times as indicated. The upper panels each shows the raw light curves which includes the intrinsic stellar variablitly. In the lower panels, this variability was removed using an eighth-order polynomial (black line). The blue circles indicate the data points predicted to be within the transit window from the PTF ephemeris (van Eyken et al. 2012); the red squares are outside the transit window. The transit event with a depth of 0.6% (left) and 2.7% are evident in the light curves. Figures taken from Ciardi et al. (2015)

Follow-up observations with the LCOGT telescope network 1.5 yr after the first transit in the SPITZER data, led to the detection of another transit with a depth of 2.7 % (shown in the right panels of Fig. 8). This event happened again close to the time predicted by the van Eyken et al. (2012) ephemeris. Interestingly, they also reported a brightening event in one of the nights (see their Fig. 3). They confirmed with these data the disappearance and reappearance of transit events and the change in shapes and depths as reported earlier by van Eyken et al. (2012). However, their data did not support the gravity darkened model of Barnes et al. (2013).

At the same time, Yu et al. (2015) monitored PTFO 8-8695 as well, to find pieces of evidence for the precession model proposed by Barnes et al. (2013). They carried out photometric observations between 2012 and 2015 with the Fred Lawrence Whipple Observatory (FLWO) 1.2 m telescope (in the i' band and some cases in the g' band) and the Transiting Planets and Planetesimals Small Telescope (TRAPPIST) 0.6 m telescopes (in $I+z$ filters) which led to the detection of 28 fading events. Through photometric observations, they discovered that the fading events are not strictly periodic and transits start to happened earlier than predicted. An example of the observed transits is shown in Fig. 9. Therefore, they proposed that a quadratic function might explain the periodicity of transits more accurately than linear relation and refined the ephemeris as

$$t_n = t_0 + P_0 n + \frac{1}{2}\frac{dp}{dn}n^2 \tag{5}$$

where

$$t_0 = 2455201.790 \pm 0.006\,\text{d} \tag{6}$$
$$P_0 = 0.448438 \pm 0.000006\,\text{d} \tag{7}$$
$$dP/dn = (-2.09 \pm 0.25) \times 10^{-8}\,\text{days epoch}^{-1}. \tag{8}$$

Accordingly, the period of a planetary object will go to zero after $\approx 10^4$ years.

Further studies done by Raetz et al. (2016) confirmed previous findings and provided more accurate information about the period of the object. Raetz et al. (2016) monitored this object with five telescopes in Asia, Europe, and America over three years as part of the *Young Exoplanet Transit Initiative* (YETI) survey. The observations were done in the R band filter in different seasons, starting from winter 2010/2011 to Feb. 2013. The observation campaign yielded to 144 observations across 42 usable nights. In 33 nights, they were able to detect transit events. They completeted this data with follow-up observations at Observatorio de Sierra Nevada (OSN) and the 2.2-m MPG/ESO telescope at La Silla.
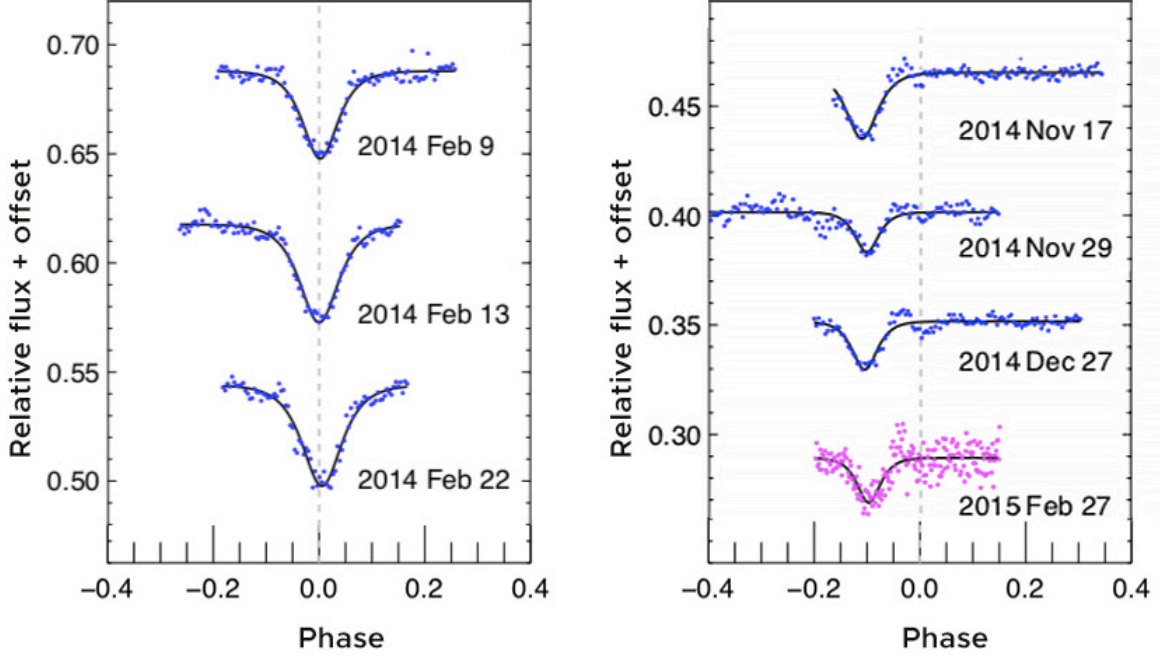
Figure 9: Selected light curves from the Fig. 2 in Yu et al. (2015). The observation times are as indicated, all light curves were subjected to the same ephemeris.

Interestingly, the depths of dimming events were changing from 2.2% to 4.7% during this time. Additionally, 3 of the dimming events had U-shapes whereas the rest are V-shaped. Besides, some of the dimming events showed asymmetric profiles which were not reported before. Selected transits are shown in Fig. 10.
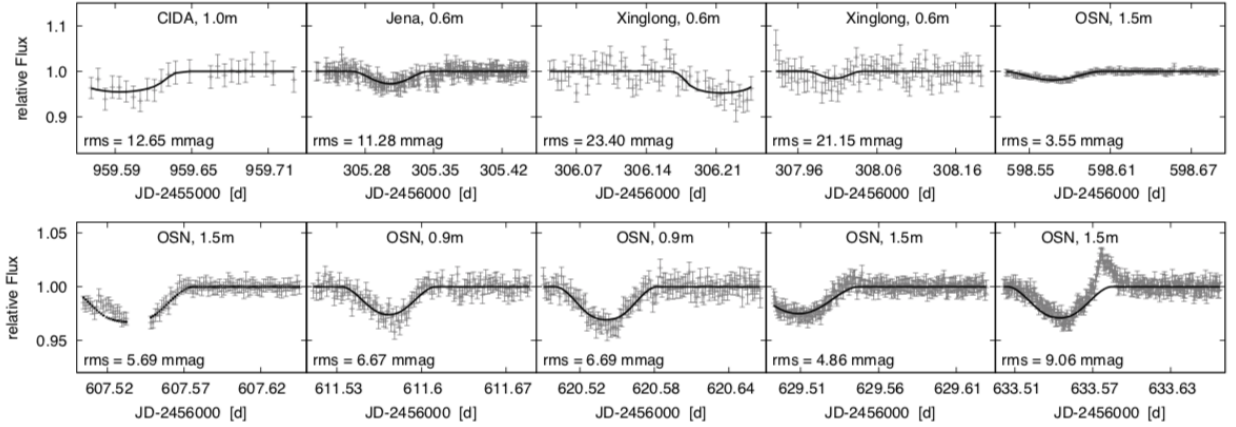

Figure 10: Light curves that show the observed dimming events of PTFO 8-8695 object in R together with a fitted model shown with black line. The dimming events at $JD = 2456607$ and $JD = 2456629$ nights are U-shaped. The dimming event in the night $JD = 2456305$ has a smaller depth compared to the others. A semi-flare feature in night of $JD = 2456633$ is evident. Figure taken from Raetz et al. (2016).

They detected one transit with depth of 3% in both, R and B bands in the La Silla data (see Fig. 2 of Raetz et al. 2016). The argued that the fact that the transit has been observed in 2 bands is in the favor of planetary hypothesis, since the signal due to a star spot is color dependent and would show different depths in different filters.

Additionally, they calculated the mid-time of detected transits and refined the transit ephemeris based on that to

$$T_c[BJD_{TDB}](E) = 2455543.9420\,\mathrm{d} + E \times 0.4483973\,\mathrm{d}, \tag{9}$$
$$\pm\, 0.0007\,\mathrm{d} \pm 0.0000004\,\mathrm{d}$$

13

with the number of orbits E since $T_0 = 2455543.9420$. The orbital period based on the new ephemeris is 1.36 seconds shorter than the period derived by van Eyken et al. (2012). Unlike Yu et al. (2015), they did not find the period of the object to decrease over time.

Fitting models on the transit events led to more precise planetary parameters compared to parameters obtained by van Eyken et al. (2012) as well (see Table 5 in Raetz et al. 2016).

Additionally, they computed Lomb-Scargle periodogram for their data to give a better measurement of the stellar rotation period and they found a strong peak for the period of $P_* = 0.49927$ d which they attributed to the stellar rotation period. This period is slightly different from the stellar rotation period of 0.448 d reported by van Eyken et al. (2012). They also detected a semi-flare feature in one of the transit times, which was reported by Ciardi et al. (2015) as well. They mentioned that the depth of the fading events is higher in the seasons that the stellar activity is stronger.

Another study of this system has been done by Schmidt et al. (2016), in which they performed photometric and spectroscopic observations with the Very Large Telescope, the Keck telescope, and the Calar Alto observatory. By combining spectroscopy with direct imaging of the system, they reported the existence of a second candidate planet, PTFO 8-8695 c with a mass in the range of 4-5 $M_{\rm Jup}$ in a very wide orbit of 662 AU and orbital period of 27250 year. For more details about the planetary parameters see their Table.4.

2.2 Problems and possible alternative explanations

We have reviewed indications for the planetary hypothesis. However, as mentioned, there have been several shreds of evidence in the different studies that put the planetary hypothesis into doubt, such as the disappearance of transits, changes in the transit shape and depths. There are several ways to test the existence of the planet in the system. The first way is through planet occultation. Hot Jupiters have a high effective temperature due the stellar irradiance and emit in the infrared due to the planet's black body radiation. When the planet is obscured by the star, a small dip in the light curve of the star and planet appears, the secondary eclipse. Observing the system in the infrared covering the predicted time of occultation can verify the presence of such a planet. Infrared observations at the time of the occultation were done by Ciardi et al. (2015) and Yu et al. (2015) and both show no sign of the planet occultation.

Also, if the assumption of the precession of the orbit is correct, we should observe several phenomena in this system as a result of the precession. Transit disappearance for some time, variations in the planetary orbital inclination, and variation in the stellar inclination are the result of the precession. The change in the orbital inclination can be identified by radial velocity measurements. The change in the stellar inclination is detectable through variations in the sky-projected rotation rate $v \sin i_*$. Additionally, the spin-orbital misalignment can be tested via the so-called Rossiter-McLaughlin effect. The Rossiter-McLaughlin effect is the spectroscopic anomaly in the line shape due to the stellar rotation during the transit of the planet. However, high-resolution spectroscopy didn't show any sign of the aforementioned phenomena (Yu et al. 2015; Ciardi et al. 2015).

Given this deficiencies, it is reasonable to consider other possible phenomena for the observed dimming events in the system. In this section, we will review indications and reasoning behind various non-planetary hypothesizes.

2.2.1 Star spots or accretion hotspot

One of the possible origins of the observed transits are star spots. Given the young age of the star (2.6 Myr), this is plausible since young stars are very active and their surfaces are covered with large scale spots at young ages that can cover almost en entire hemisphere. The similarity between periods of the star and dimming events strengthens this hypothesis as well. Differences may be explained by differential rotation. Additionally in some studies, the fading events were wavelength-dependent and were shallower in redder bands compared to bluer bands . Yu et al. (2015) observed this system between 2012-2015 years in i', g', Gunn r', and $I + z$ bands. Transit events were 30-50% deeper in the g' band compared to i' and also $20-30\%$ deeper in the $I+z$ band compared to r' band, with the notable exception for one night which they had similar depth. The observations are shown in Fig. 11 and the night in which the depths are similar in both bands, shown in the upper right panel.

This phenomena were evident in other works as well. Onitsuka et al. (2017) conducted simultaneous observations in different color bands on 2016 Feb. 9th and found vastly different transit depths in each band (cf. Fig. 12). They found transit depths of 3.1%, 1.7% and 1.0% for g', r', and z bands, respectively, which again shows that the transit depths decrease towards redder wavelengths.

However, there is a shortcoming to this hypothesis. If there is a starspot on the surface that produces the observed transits, it is visible on just one side of the star, and therefore, the timescale for the transits in its maximum, is half of the stellar rotation period, as pointed out by Yu et al. (2015). However, the duration of the observed transits is about 1.8h which is $\pm$ 15% of the rotation period. Additionally, spots near the poles
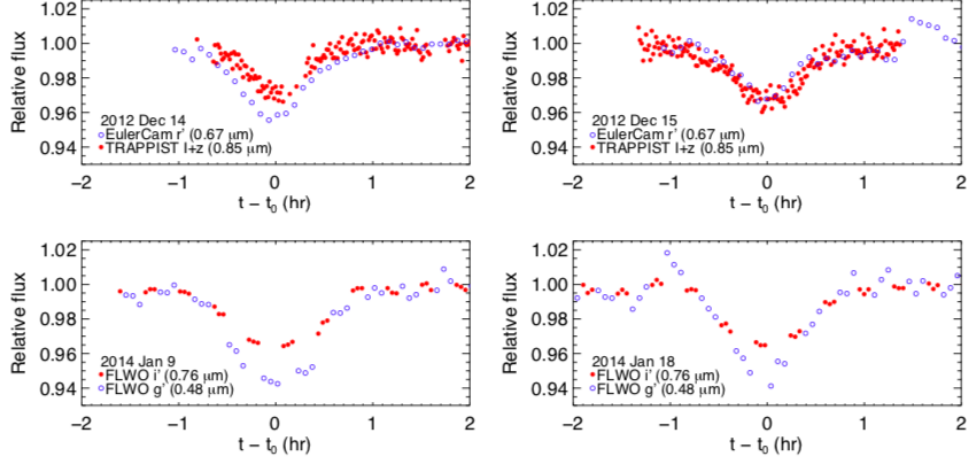
Figure 11: Photometric observations of PTFO 8-8695 between 2012 - 2015 in different bands.The top panels shows observations in r' (blue) and $I + z$ (red) filters. In the lower panel, the observations in g' and i' band are shown with open blue and filled red circles. Figure taken from Yu et al. (2015).
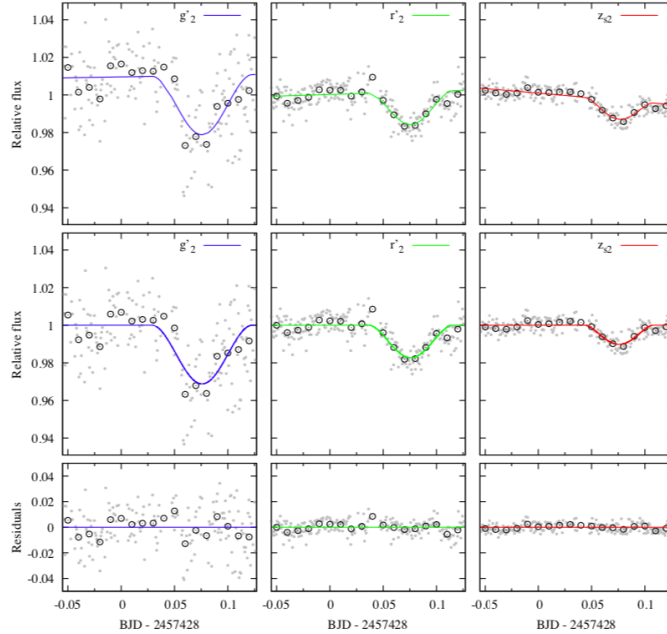

Figure 12: Observations of PTFO 8-8695 in different bands in February 2016. Raw and binned data are shown with gray dots and open black circles, respectively. A Model is fitted to each (blue, green, and red lines) with the corresponding filter indicated. The top panel shows the raw light curve, the middle panel shows the light curve corrected for the intrinsic stellar variability with a low order polynomial, and the bottom panel shows the residual between model and observations. Figure taken from Onitsuka et al. (2017).

have their problems to produce the observed transits with a few percentage dip over several years, since it's unlikely for starspots to remain near poles for several years. With all being said, an accretion hotspot might provide a better explanation.

In classical T Tauri stars which have an accretion disk, an accretion hotspot might form along the stellar magnetosphere. This phenomenon can happen in WTTS as well if an optically thin disk still exists. Also, ongoing accretion in the system has been reported by Ciardi et al. (2015) and Yu et al. (2015) due to detection of time-variable Hα emission in the spectra and detection of brightening events.

Thus, Yu et al. (2015), proposed that the fading events might arise from occultation of an accretion hotspot due to an optically thin disk. Accordingly, they assumed a luminous hotspot with effective temperature up to 10^4 K on the surface of the star which is visible for $\pm 85\%$ of the rotation period (due to the high latitude), might have caused the observed transits. They estimated the possible accretion rate to be $\approx 10^{-9}\,\mathrm{M}_\odot\,\mathrm{yr}^{-1}$. However, since the accretion hotspot and the transits caused by them are still unknown,

confirming this hypothesis is challenging. Nevertheless, they preferred this scenario for the origin of their observed dips since its consistent with their observations and estimated accretion rate.

2.2.2   Occultation of circumstellar dust clump

Another probable and possible origin for the observed transits is the circumstellar dust clump. The dust clump or material in the accretion disk might cause periodic transit events.

Hernández et al. (2007) based on SPITZER observations of PTFO 8-8695 in different IRAC bands and lack of IR excess, classified this system as a disk-less system. Additionally, the spectral energy distribution of the system (SED) analyzed by Yu et al. (2015), shows no signs of infrared excess as well. Despite that, the possibility of the existence of an optically thin disk or small remnant of dust/clump around the system is there, since optical spectra (Yu et al. 2015) indicate Hα line emission in the system. In addition to that, Johns-Krull et al. (2016) observed Hα emission profiles from the system that exhibit a radial velocity shift.

As shown in Fig. 13, the velocity profile of the Hα line has been extended to 300 km s^{-1} which means there exists material around the star that falls onto the star with this free-fall velocity. The material could be a dust clump which caused the observed transits as well. Onitsuka et al. (2017) based on the detection of the wavelength dependence of the fading events, stated dust clump as the possible origin for the observed transits since it is the most consistent scenario with their observed dips.
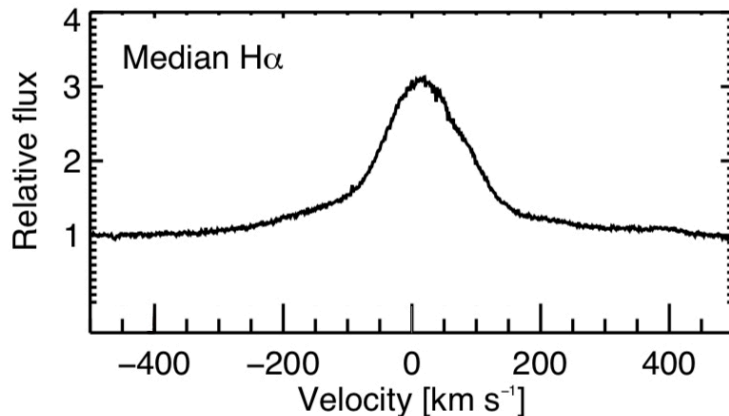

Figure 13: The median profile of Hα line for all spectra taken on 12 December, 2013. This is one of the indication for the accretion disk. Figure taken from Yu et al. (2015)

Several studies of T Tauri stars in the star-forming regions of clusters have shown a fraction of T Tauri stars, called 'transient dipper stars', exhibit irregular short-duration and shallow periodic dimming events similar to the PTFO 8-8695, (Stauffer et al. 2015; David et al. 2017). These stars have rotation periods at the order of $3 < P < 11$ days and the rotation period of the star and dimming events are similar. Also, the depths of dips are changing over time. However, all of these stars exhibit infrared excesses in their SEDs due to the existence of an accretion disk, which is not the case for the PTFO 8-8695. Additionally, the rotation period of PTFO-88695 is shorter than these stars. Nevertheless, Yu et al. (2015) mentioned that their observations of PTFO 8-8695 show similarities between PTFO 8-8695 and these stars. Interestingly, infalling dust clumps that are located in the accretion disk were the proposed scenario for the origin of dips in these stars (McGinnis et al. 2015).

2.2.3   Stellar binary

Another interesting hypothesis is the possibility in which system is a binary indeed and not a star-planet system. Bouma et al. (2020) investigated this possibility by analyzing the recent high precision *Transiting Exoplanet Survey Satellite* (TESS) data and Gaia data.

they analyzed variabilities in the light curves by fitting a model consists of Fourier modes with periods of P_l and P_s as well as a different number of harmonics. They found out that the observed variability in the light curves is due to the two long and short periods, 11.98 hr (0.49911 d) and 10.76 hr (0.44844 d) respectively. While the long variability was always sinusoidal and probably due to the stellar rotation as mentioned by other works previously, the short variability was more complex. Also, they reported small shorter scale variabilities between phases of -0.5 and 0.0.

Additionally, for examining if the system is a photometric binary, they analyzed the Gaia data and found out this object is two times more luminous than a single star in the 25 Ori-1 group (See left panel

of Fig. 14). Moreover, gaia DR2 astrometric modelling shows astrometric excess, meaning the single-star model failed to provide a good fit to the observed astrometric measurements which can be either due to the phtometric binarity or photometric variability (see right panel of Fig. 14). However, they mentioned photometric variability can not be the case since the comparable variable systems did not show such a large astrometric excess. Therefore, they proposed that the observed variabilities might be due to a rapidly rotating M dwarf with the period of 0.44844 d in the system which has similar spectral type to PTFO 8-8695.
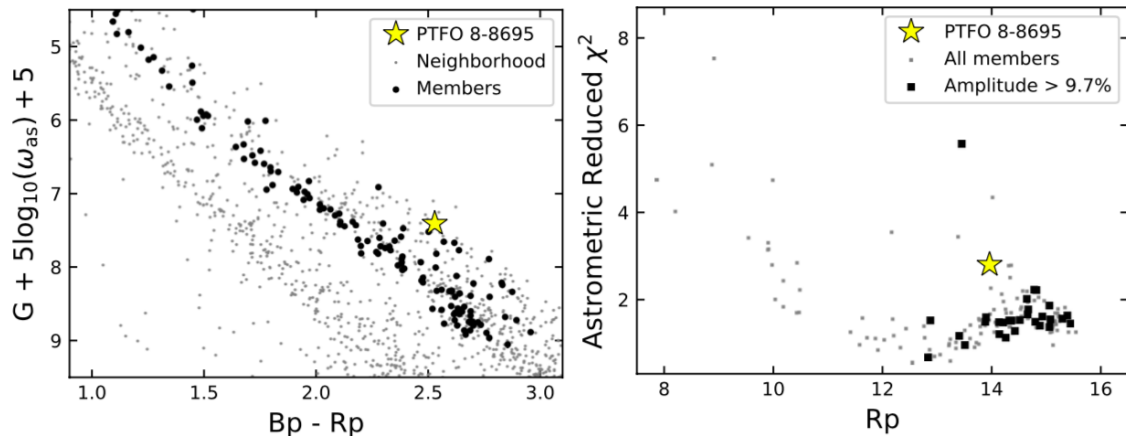

Figure 14: Evidence for the binarity of this system based on GAIA data. In the left panel, the color-magnitude diagram of stars in the 25 Ori-1 group is shown and PTFO 8-8695 is marked as a yellow star. Black circles are members of the 25 Ori-1 group whereas the gray circles indicate the neighborhood stars, members of the Orion complex. In the right panel, the goodness of fit for astrometric fitting against Rp color is shown. It can be seen easily that the one-single star astrometric model gives a higher squared-fit for PTFO 8-8695 compared to fit for other objects in the cluster.

At the same time, Koen (2020) by performing Fourier analysis on the TESS data, found two signals with periods of 0.4990 d, and 0.4486 d respectively. Their found periods are similar to the results of Bouma et al. (2020). They concluded PTFO 8-8695 is a binary star, probably composed of two T Tauri stars.

2.3 Three different phenomena all in one light curve

Another recent work done by Tanimoto et al. (2020) shed new light on the nature of this system. They monitored this system for over five years, from Feb. 2014 to Dec. 2018 in two different optical and infrared bands with the Kanata telescope at the Higashi-Hiroshima Observatory.

In their observations, they reported the split of fading events after Dec. 2014 into two shallower dips. They suggested that there are three different types of dips in the system, each reflecting a different phenomenon. The observed transits are shown in Fig. 15 and these dips have different phases and depths each. They examined different scenarios for each dip based on the wavelength dependence of the dips. Based on the transit times of the dip B, they refined the ephemeris of the system as follow:

$$T_{0[BJD]} = (2455543.943 \pm 0.002)\,\text{d} \tag{10}$$
$$P = 0.4483993 \pm 0.000006.$$

The dip A, located at $\varphi = -0.1$, has depths of $1.37-2.23\,\%$ in the optical and depths of $0.92-1.64\,\%$ in the infrared. This dip shows the wavelength dependence as reported by previous works and has an infrared to optical ratio of 0.7. They investigated different hypotheses for the origin of dip A and based on their analysis, neither hotspot nor starspot can satisfy the observed dip properties in 2014 and 2016. The second hypothesis, the planetary scenario, has been ruled out, too, since the atmosphere on the planet would induce infrared-to-optical depth ratios of about unity. In the seasons 2014 and 2016, it is less than 1.

However, dust clumps might be the origin of dip A, as concluded by Onitsuka et al. (2017). According to Tanimoto et al. (2020), an optically thin dust clump alone can not produce the observed dip depth. This is because they estimated the wavelength dependence of the transit depths due to an optically thin dust cloud (based on the extinction law of an optically thin disk). However, the estimated wavelength dependence is not consistent with the observations as shown in the Fig. 16. Instead, a dust clump consisting of an opaque core and an optically thin dust halo (which core might collapse into dust cloud), gives a better fit to the observed dip properties in 2014 and 2016.

The second dip B, located at phase 0.0, has depth of $0.6-0.81\%$ in the optical and $0.56-0.63\%$ in the infrared. Based on the observed infrared-to-optical depth ratio of dip B, they attributed this one to a planet
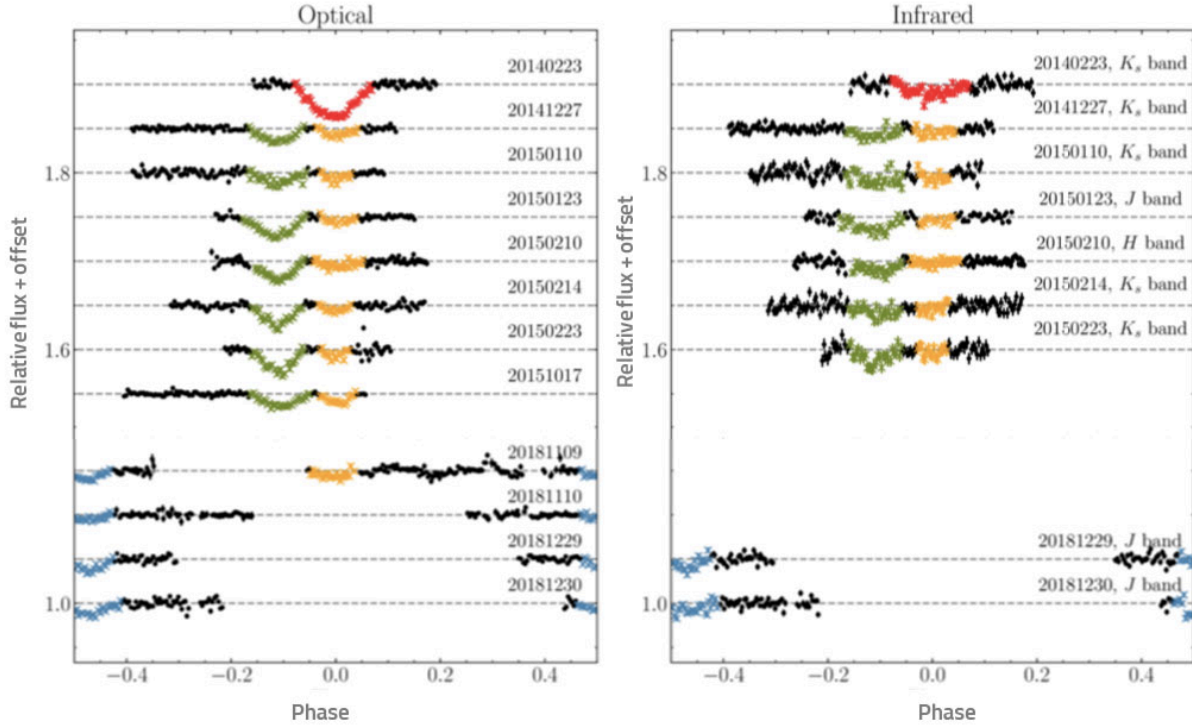
Figure 15: The fading events observed by Tanimoto et al. (2020) in optical and infrared bands. Transit before splitting, "dip-A", dip-B", and "dip-C" are shown with red, green, orange, and blue crosses. The phases are calculated based on their new refined ephemeris.
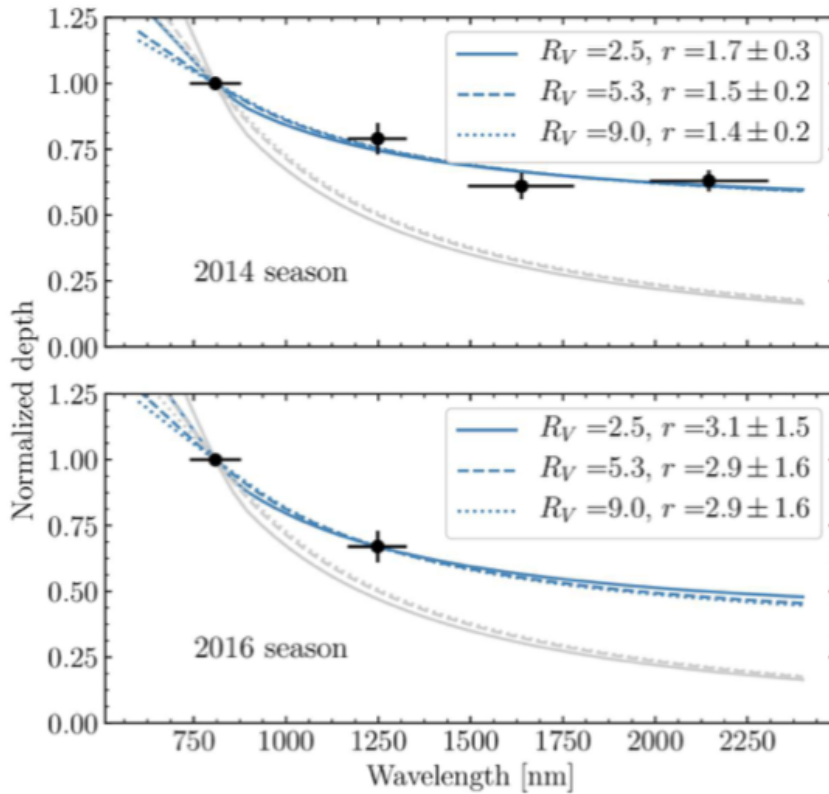

Figure 16: Normalized depth of dip-A versus wavelength for the 2014 (top panel) and 2016 (bottom panel) seasons. Gray lines show the estimated wavelength dependence of an optically thin cloud whereas the blue ones show core-halo dust clump models for different extinction (Rv) parameters.

with an upper mass limit of $4.9 \pm 1.2 M_{\mathrm{Jup}}$ on a precessing orbit. Based on their core-halo dust clump model,

they estimated the potential planet's radius to be around $0.22R_{\mathrm{Jup}}$. Considering this radius, the planet might be a super-Earth or Neptune-sized planet. They also mentioned $0.36 \pm 0.15R_{\mathrm{Jup}}$ as the radius of the potential planet. Further, they derived the inclination angle i of the planet orbit and found the precession period to be $\approx 1411\,\mathrm{d}$.
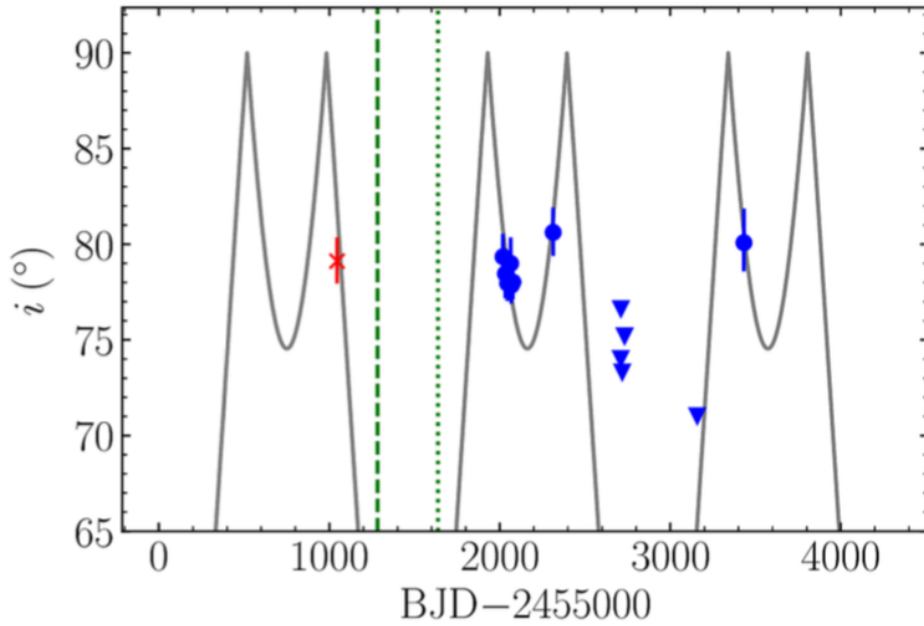

Figure 17: Periodicity of the inclination angle over five years. The solid line shows the fitted sinusoidal function. The circles and triangles show the derived values and their upper limits. The cross is the value derived from Yu et al. (2015), whereas the vertical and dashed lines show the corresponding inclination angles for the Ciardi et al. (2015) and Yu et al. (2015) data.

For the last observed dip, dip C, there is as well an interesting discussion in the paper. This dip has appeared at the phase $\varphi = 0.5$ with a depth of $0.95 \pm 0.09\%$ in infrared and a depth of $1.30 \pm 0.06\%$ in the optical.

They examined hotspots as the origin of this dip based on its infrared-to-optical depth ratio. Since the observed ratio in I and J band satisfies (to some extent) the requirements, they attributed dip C to a hotspot with a temperature of about 3800 K. They added that dust clump may as well account for the origin of dip C.

They argued that their results are consistent with previous observations and that they can explain the non-detection of the RM effect and the planetary secondary eclipse in previous works. The non-detection of RM effect in the works of Yu et al. (2015) and Ciardi et al. (2015) can be due to the small inclination angle at the time of observation which led to no transit detection.

3 Observational data

The data that has been used for the analysis of this object consists of 3 different data sets. Due to the complexity and faintness of this system, high quality and high precision data are needed. In this section, we will describe the data and instruments that data has been taken with.

3.1 STELLA

Observations

We conducted observations of the PTFO 8-8695 with the STELLar Activity telescope (STELLA), located at the Izana observatory, Spain (Strassmeier et al. 2004). The STELLA is a 1.2m robotic telescope which consists of a high-resolution spectrograph (SES) and a wide-field imager (WIFSIP).

Our observing campaign was carried out over $\sim$ 72 nights between 17 January and 24 of April of 2019 in different filters which resulted in 241 images at the end. The observations are taken in two filters of r pirme (r') and H alpha wide ($H\alpha_w$). The STELLA telescope was targeted at the Orion constellation, where PTFO 8-8695 is located, for about two months. To be more specific, the STELLA field of view was centered at RA.(J2000) = '05:25:25.97' and DEC.(J2000) = '01:35:26.6'. Images have been taken with the 'WIFSIP V3.0' Camera. WIFSIP is a wide field STELLA imaging photometer with a large CCD imager and a photometer. The detector captures images with a single 4096 × 4096 pixels thinned CCD. Its field of view is about 22' × 22' and the scale between pixel and sky coordinate is about 0.32 arc second per pixel.

Data reduction

To extract valuable data from the images, we need to perform data reduction on the images. Data reduction has been done by Python. The CCD of the STELLA telescope produces four individual frames, each in the format of 2076 × 2076 pixels. There are over-scan regions in these four frames that one needs to cut them individually. This has been done by cropping 1 pixel from the bottom, 29 pixels from the top, 4 pixels from the left, and 24 pixels from the right side of each frame which reduced the format of the each frame to 2048 × 2046. Additionally, each frame should be rotated accordingly and then stitch together to have one full image at the end. In the next step, the frames have to be rotated accordingly. The first frame has been rotated 90 degrees clockwise. The second one has been flipped and been rotated 90 degrees clockwise. The third frame has been flipped and rotated 90 degrees counterclockwise. The last one, has been rotated 90 degrees counterclockwise. At the end, we stitched the four frames to have a full image. An example of the raw frames and also frames after cropping and rotating, is shown in the Fig. 18.
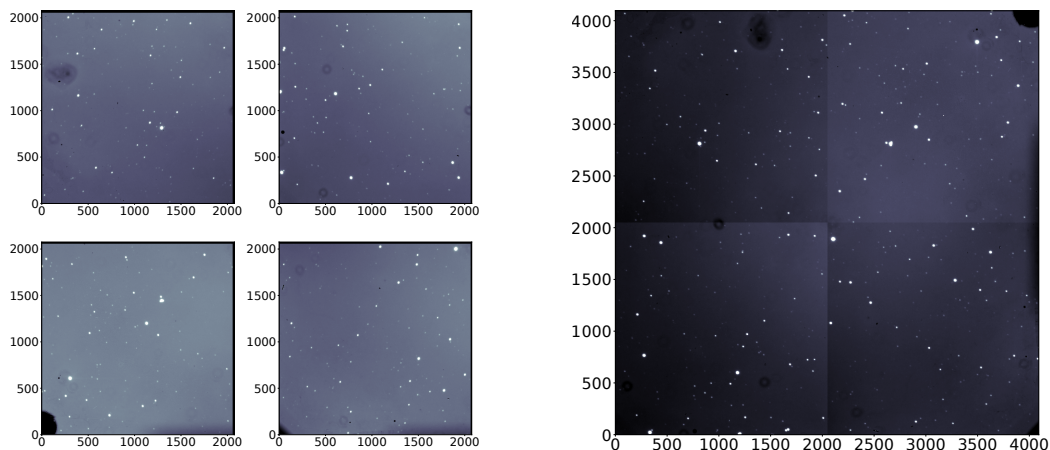

Figure 18: The left panel shows the raw images of the PTFO 8-8695 object taken with the STELLA telescope. The right panel shows the frames after rotating and cropping.

As it is shown in Fig. 18, the raw images contain several noises and artifacts. Additionally, our target is extremely faint which makes the effect of noises more prominent in the scientific analysis. Thus, in order to get the most out of data, sky and technical noises that have been added to images during observations and afterward should be identified and corrected.

In general, the unwanted noises and artifacts in the images can be categorized into three different sources:

- Sky background: Cosmic rays, optical light

- CCD chip and ADC charge count: Hot pixels, dark current, dust donuts, read-out noise

- Telescope: Vignetting, reflections

Eliminating sky background noises can be done by aperture photometry on the images which will be discussed in Sect. 4. However, the noises associated with the CCD chip and telescope can be diminished with image corrections. This usually is being done by subtracting the image frames from the science image data. These image frames that have been taken in the absence of the science signal only represent the systematic noises and are called bias, dark frames, and flat fields.

Bias frames correct for the read-out noise. Read-out noise is associated with the chip amplifier which converts the number of photons (electrons) that hit the CCD chip into analog voltage and CCD output and there is a small difference at the order of $\pm$ 3e between the output value and the actual number of photons that hit the CCD. Bias frames contain only read-out noise and being taken with zero exposure time and closed shutter. By subtracting the bias frame from the science image, we remove the bias values.

Dark frames correct for the thermal noises or dark current in the raw image. Thermal energy in the CCD chip over some time can lead to the creation of additional electrons which then can be mistakenly counted by CCD as a science signal. Therefore, we need to correct the noises and remove them as much as possible. Additionally, we need to correct for the hot pixels which are pixels that have higher dark current compared to other pixels. This can be done by subtracting dark frames from the science images. Usually, the exposure time for dark frames is longer than bias and flat field. But dark frame should have a similar exposure time with the exposure time of the image it is used to correct for. Thus, one needs to scale the dark frame and the specific image to which dark corrections have been applied on.

Flat field frames correct for pixel sensitivity variations in the CCD chip and dust donuts, scratches, and vignetting by telescope or camera lens. The technique for taking flat field images is to use a halogen lamp that has illuminated the surface of the telescope.

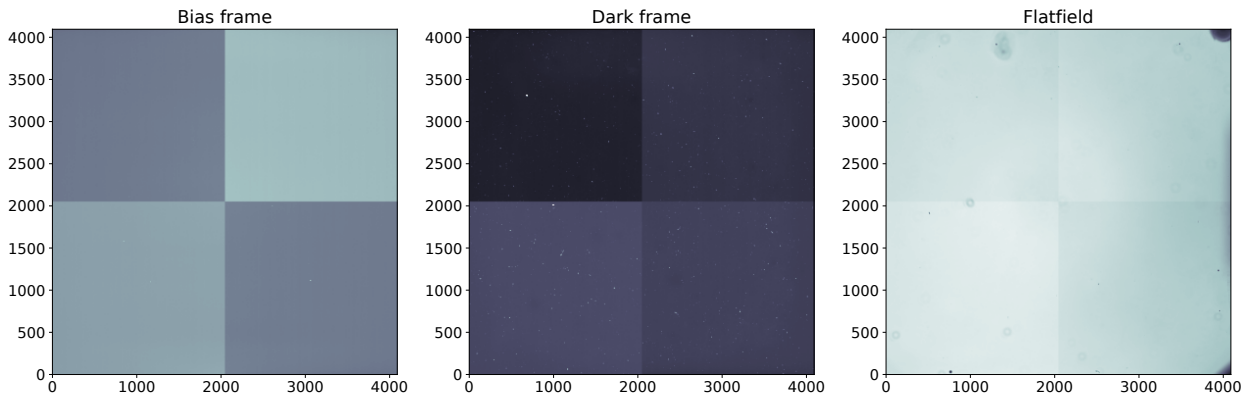One example of the bias, dark and flat field can be seen in the Fig. 19.

Figure 19: Examples of Bias, dark and flat field frames from left to right. Read-out noises in the dark frame can be seen. In the flat field frame, the dust donuts due to the CCD is evident.

For each of the mentioned frames, it is better to capture several images and then combine them either by using median or mean to reduce noises. However, using the median will give a better result since it will remove the effect of outliers.

We captured bias, dark and flat-field frames on different nights. For making master bias and master dark, we combined the dark frames and bias frames using the median.

For master dark, we need to correct for the bias noises, which by subtracting master bias from the dark frame, we applied correction. It is generally better to take dark frames with a similar exposure time as science images. In our case, for the r' filter, the dark frames exposure time is about 1800 s and the science image exposure time is 120 s. For scaling both science images and dark images, we divided the master dark by 15.

For the master flat-field file, however, we need to correct for dark noises as well as bias noises. Since the exposure time of the flat frame is ≈ 5s, we first divide the master dark by 24 to scale the exposure times. Then, we subtracted scaled master dark and master bias from each flat field frame and then combine flat frames using the median. In the end, we normalized the flat field.

For science image data reduction, we have subtracted master files from the raw image as described in the following:

$$\text{Reduced image} = \frac{\text{raw image} - \text{master bias} - \text{master dark}}{\text{Flat field}} \tag{11}$$

In the Fig. 20, one example of a raw image before data reduction and after data reduction applied on it (in r' filter) has been shown.
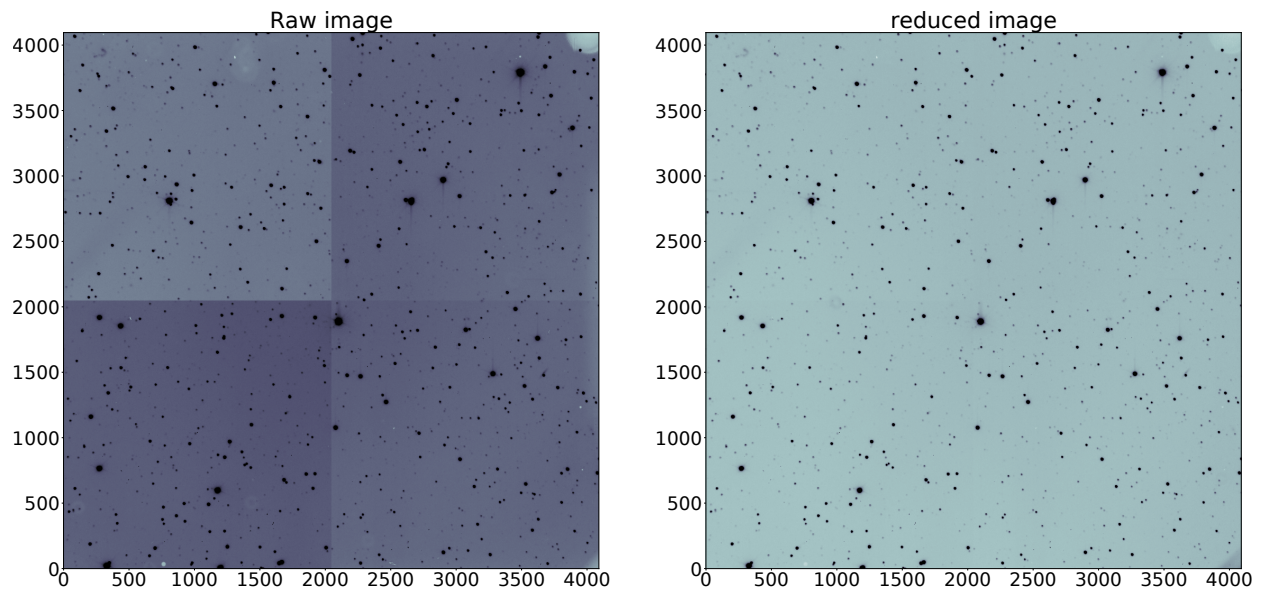

Figure 20: One example of raw image and reduced image after data calibration applied for r' filter. According to the difference in contrast for each segment between raw and reduced image, the effect of dust donuts and noises have been diminished to a good extent in the reduced image. Note that for better visualization, the scales are different.

However, at the time of the scientific analysis, the reduced images with the STELLA data reduction pipeline were ready and in higher quality compared to our reduced images. Thus we decide to do the scientific analysis with the data reduced with the standard pipeline.

3.2 LCO

Observations and data reduction

The observations of the PTFO 8-8695 object have been carried out with the Las Cumbres Observatory (LCO[7]) which is a worldwide network of robotic telescopes in different sites in the world.

The images have been taken with an ANDICAM CCD camera on 1.3 meter SMART telescope. The CCD is a two-dimensional Fairchild 447 with 2048×2048 pixels made of 15-micron pixels. The CCD's field of view is about 2.4×2.4 arcmin and each pixel corresponds to 0.276 arcsec on the sky. The observations took place on January 15, 2017, with the duration of ~ 4 h in an optical R filter. The exposure time for each image is about 90 s. The time between each image is about ≈ 2 min. In the end, we used 85 images for our analysis.

Data reduction has been done with the BANZAI pipeline. Reduced images are in the format of 1024×1024 pixel. However, there are regions in the reduced images which are not exposed to the light and have to be cut from the images. To do so, 100 pixels in both, x and y direction, on the left side of the image are cut. A comparison between a reduced image before and after cropping is displayed in the Fig. 21.
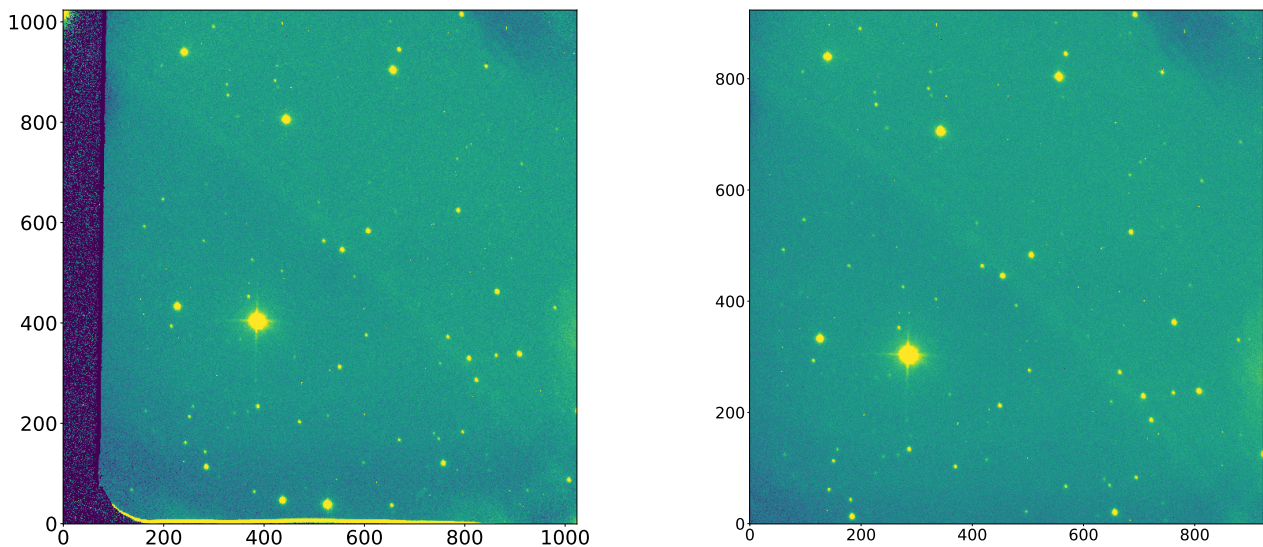

Figure 21: The raw image before cropping overscan regions is shown in the left panel and the edited image after cropping is shown in the right panel.

3.3 TESS

In order to gather more information about the observed transits and their time of occurrence, we analyzed archival data from NASA's Transiting Exoplanet Survey Satellite (TESS) which is publicly available on the The Barbara A. Mikulski Archive for Space Telescopes (MAST[8]). TESS is a mission led and managed by the MIT and NASA's Space Flight Center. The satellite's mission is to detect several small and Earth-like planets around bright and nearby stars by looking for brightness variation in $\sim 10\,000$ stars.TESS achieves an almost all-sky coverage with varying lengths of observational baselines, from 21 d at an ecliptic latitude of $6°$ to almost a year continuous coverage around the ecliptic poles. A $\pm 6°$ band around the ecliptic is not observed. The satellite is equipped with four wide field cameras, each of which has a field of view of $24° \times 24°$ and observes the sky in consecutive sectors of $24° \times 96°$. Full Frame images are available with a 30 min cadence and for a large number of selected targets 2 min cadence observations are available.

PTFO 8-8695 has been observed by TESS satellite for 21 d in sector sixth, from Dec. 15th, 2018 to Jan. 6th, 2019. The aperture photometry on the 2-minutes images was carried out by the Science Processing Operations Center (SPOC) at the NASA Ames Research Center (Jenkins et al. 2016). The resulting light curves are public on the MAST website. We have used the light curves based on the Simple Aperture

---

[7]https://lco.global
[8]https://mast.stsci.edu

Photometry (SAP) flux for our analysis. The original light curve is shown in the Fig. 22. TESS data uses its own time TBJD which is TBJD = BJD - 2457000. For our analysis, we have converted the TBJD time format of data to BJD. To clean the data, we removed the nan value fluxes and their associated times.
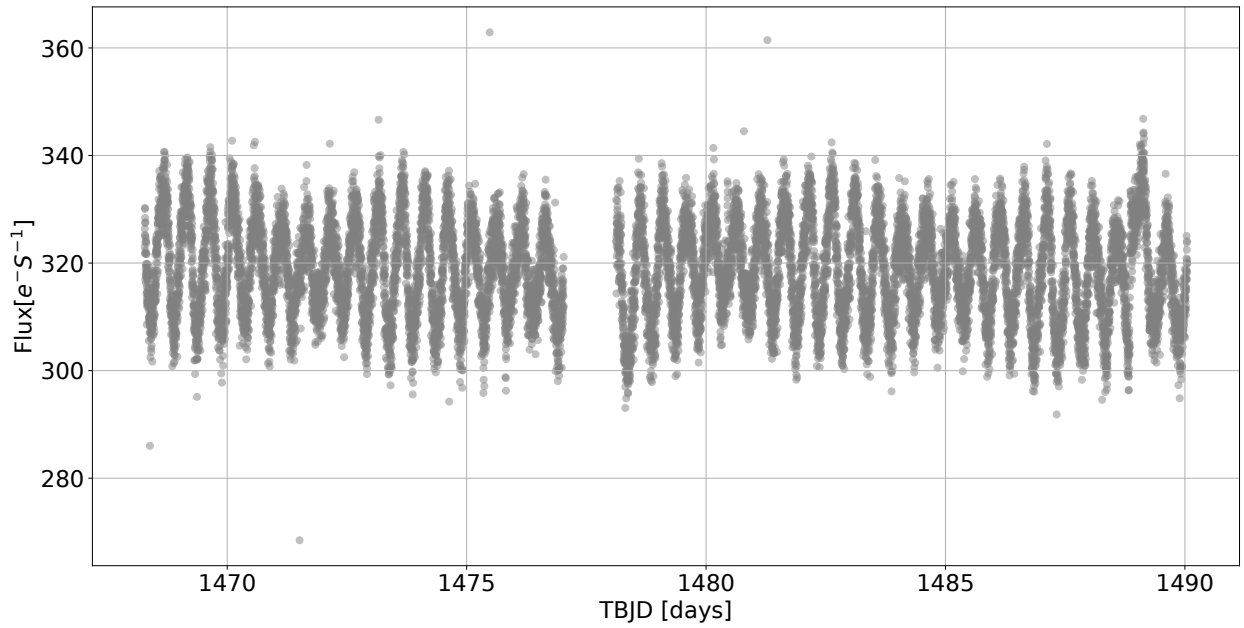

Figure 22: The raw light curve of PTFO 8-8695 with duration of 21 days. The SAP flux is plotted versus the TBJD time.

4 Relative Aperture Photometry

4.1 Relative Aperture Photometry method in theory

One of the first things astronomers noticed was that stars are not eternal, but do change over time. Stars changed their brightness significantly and visibly with the naked eye. In ancient history, people attributed this behavior to a supernatural being and some stars are named according to this, like Algol, which was the *demon's eye* that blinked on the night sky. Today we know more, and the changing brightness of Algol is not a demon, but the fact that it is an eclipsing binary star.

To make such discoveries, astronomers observed stars for a long time and recorded their brightness, from observations by eye in ancient times, to photographic plates and electric photometers and modern detectors nowadays, our way of doing so became more sophisticated. And as such our knowledge of the stars we observed grew as well. However, the fundamental principle has stayed the same since ancient times, we record the brightness of a star as the amount of energy E we receive from them, called stellar flux. We usually record the stellar flux in a certain bandpass or wavelength range. The monochromatic flux by definition is:

$$F_\lambda = \frac{\Delta E}{\Delta A \Delta t \Delta \lambda} \tag{12}$$

Nowadays, we use modern detectors, CCD chips, to record the flux of stars of interest. A CCD image is technically a two-dimensional array that each entry is a pixel count rate. The readout counts N_c in each pixel are proportional to the number of electrons stored which is equal to the number of photons that hit the detector. With the justified assumption that variation of the energy between those photons is small (limited by the used filter), the total received energy and hence the flux is proportional to N_C.

Practically, for measuring flux, we do aperture photometry on each image. This means we sum up all the counts, N_c over illuminated pixels by fixing an aperture on the star with a reasonable radius. However, the received counts should be corrected for instrumental and observational effects which we briefly mention here.

The earth's atmosphere is constantly in motion which makes observations with ground-based telescopes challenging and introduces additional effects to the recorded flux that have to be addressed. There are several atmospheric-related phenomena such as seeing, air mass variations, or scattering which affect the data quality and ultimately our analysis. When the light from celestial objects passes through the atmosphere, there is turbulence in the way. Several patches of air with different temperature and pressure, causes the light being refracted with different refraction index. This leads to two effects. This might change the position of the star on the captured image over several nights or makes the star looks bigger on the image since the counts spread over different pixels. This is called the seeing effect.

Another important effect is air mass variations. When we look at stars with a telescope over several hours, the path that light travels to the telescope is changing due to the change in the altitude of the star. This causes the photons to experience different air mass densities in the way. The more airmass results in more scattering and fewer photons on the detector.

This is where calibration stars come into play to correct for these effects. We usually use stars as comparison stars that have constant brightness and similar magnitude and color to our target by assuming that those stars similarly suffer from those effects as the target. This means if the number of counts for the target in one particular night changes, the number of counts for comparison stars does so in a similar way. Therefore, by dividing their counts, N_t/N_c, we correct for these effects and get the relative flux. This is why this method is called relative aperture photometry. We did aperture photometry on our images with a normal aperture of around 10 pixels to see the effect of airmass variation on the calculated number of counts.

It can be seen in the Fig. 23 the effect of airmass variations on the light curve of stars before and after calibrations. It goes without saying when the airmass is low, the flux is high, and vice versa. Comparison stars have removed the effect of airmass variations to a very good extent.
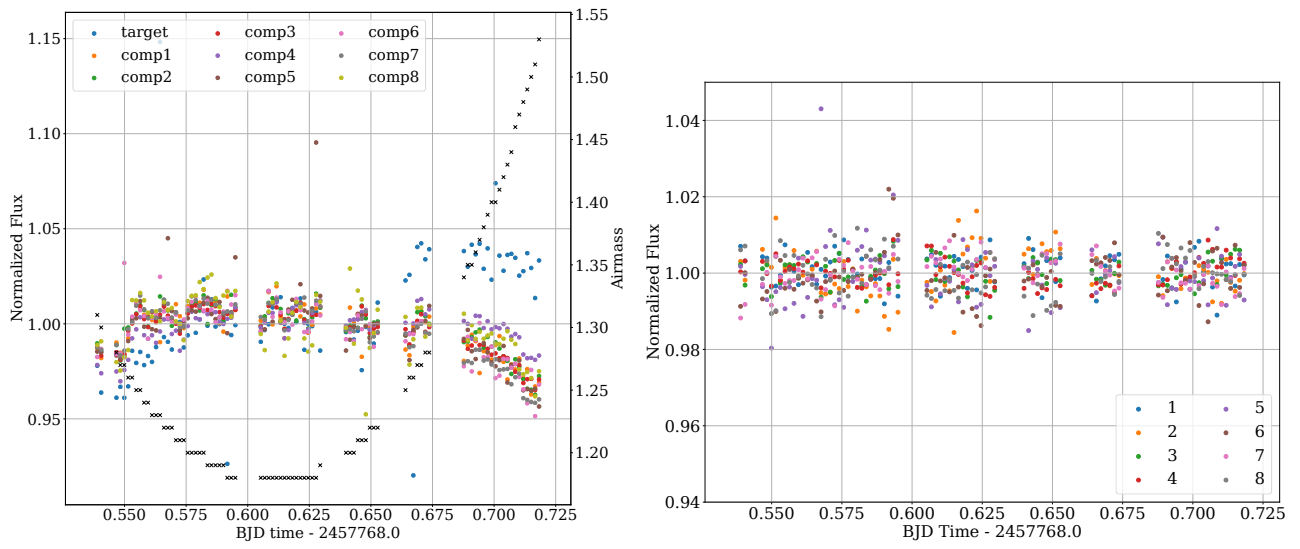
Figure 23: The light curve of comparison stars before and after the calibration process. The raw counts of calibration stars and target are shown in the left panel over the daytime of observation. The variation due to airmass is plotted with black crosses. The right panel shows the calibrated light curves of the calibration stars.

4.2 Relative Aperture Photometry in practice

To study and analyze this system, we need to analyze its light curve. This means we need to extract the flux of the target in each image and plot it against the timestamp of the image.

We used the aperture photometry method to obtain fluxes and remove atmospheric and instrumental effects. The principles of aperture photometry have been discussed in the Section.4. We perform aperture photometry on LCO and STELLA observed images using Photutils Package in Python.

4.2.1 STELLA

Checking images

Before doing aperture photometry, we need to check images individually to avoid adding additional noises into our analysis. Some of the images were not useful for our analysis due to the high airmass during observation night or improper observational conditions and we discard using them. Some of the examples of the not proper images that we have not used have been shown in the figure below.
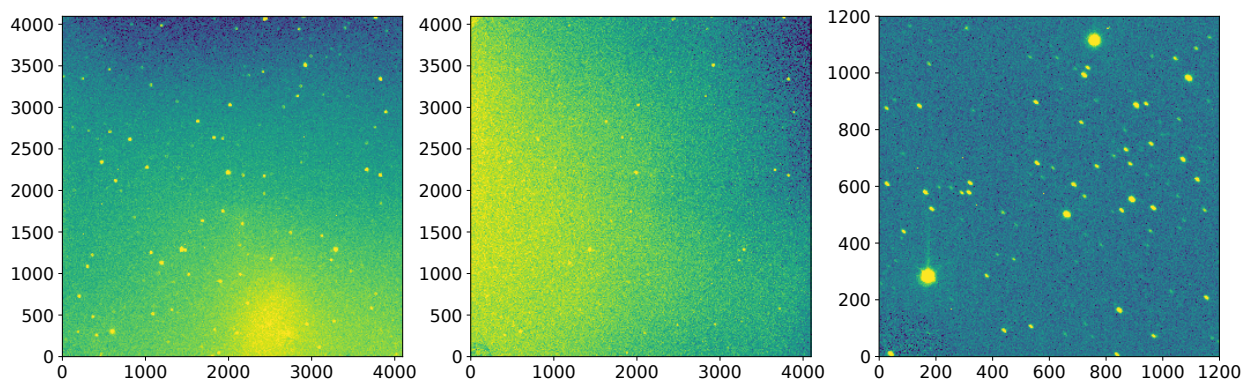

Figure 24: Three examples of images that have been taken during inappropriate observational conditions. The first image from the left contains a high amount of background noises and clouds as well. The second image suffers from high air mass. In the third image, the star profiles are elongated due to the slight movement of the camera during observations.

Calibration stars

We selected stars for calibration that have a similar brightness and magnitude in r' band and also similar color over different bands as PTFO 8-8695. Additionally, these stars are neither saturated nor intrinsically variable. The selected stars are listed in Table 4.2.1.

Table 2: Selected comparison stars for the calibration of the STELLA light curve. Parameters are taken from the *Gaia* catalog DR2 (Gaia Collaboration (2018))

Object	Gaia ID	Ra (J2000) [°]	Dec (J2000) [°]	G_{RP} [mag]	$G_{BP} - G_{RP}$ [mag]
PTFO 8-8695	3222255959210123904	81.281484	1.5734303	13.96	2.52
calib1	3222258501830719616	81.25858304071	1.62251294768	14.00	2.50
calib2	3222210192038426240	81.34526960187	1.5587897356	14.69	1.32
calib3	3222256027929421568	81.24959955150	1.56592300713	14.63	1.29
calib4	3222255203295716352	81.22183367290	1.51491854326	14.91	1.20
calib5	3222255787411256960	81.24462862087	1.55334277397	14.55	1.03

Aperture size

The aperture sizes we used for the aperture photometry is about 5.0 pixels for PTFO 8-8695 object and calibration stars as well. For removing background noise, we used an aperture size of 4.0 pixels around the target and stars.
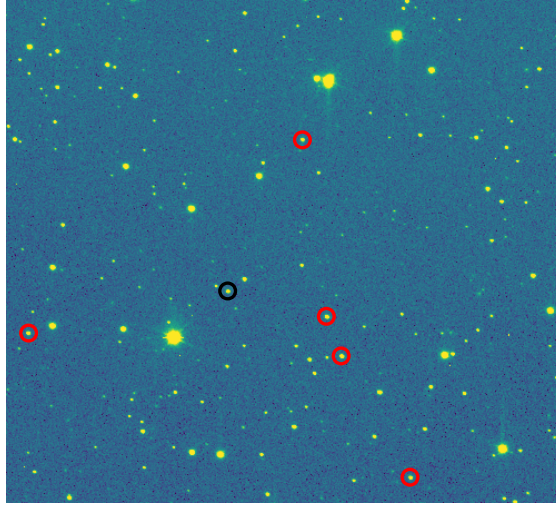
Figure 25: Target and calibration stars marked with black circle and red circle respectively.

Light curve analysis

The final light curve in both rp and haw filters is displayed in the figure below. Additionally, light curves phase folded with stellar rotation period as well as planetary periods are displayed in the lower panels of Fig 26. As can be seen, the scattering is high in the light curves. However, due to the inadequate quality
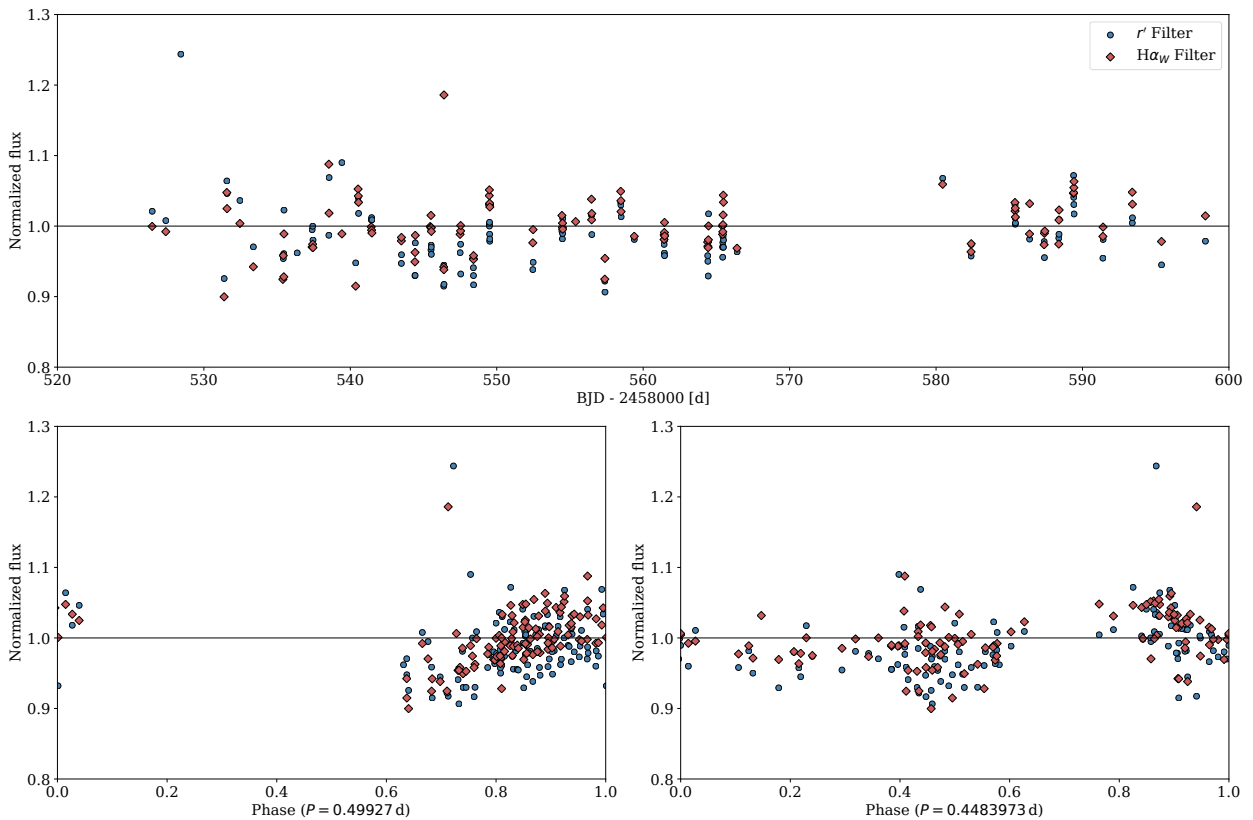

Figure 26: The extracted light curve from STELLA observations. The upper panel shows the light curve in both r' and $H\alpha_w$ filters. The lower left and right panels show the phase folded light curves with stellar and planetary periods respectively.

of the light curves, we discarded doing further analysis regarding the planetary nature of the PTFO 8-8695 system.

4.2.2 LCO

Checking images

In the first step, we check the individual images by eye to see if there are any airplanes, satellites, clouds, or cosmics close to any of the comparison stars or the target. All images have been checked and we find only one image where a cosmic is close to the image of our target but it is easily outside the chosen aperture. Hence, we are safe to use all 85 images for our analysis

Identification of stars

The first step for performing aperture photometry is the identification of stars in the images. For that, we use the DAOStarFinder algorithm which is part of the photutils package for python. In short, it identifies stars using a gaussian kernel (in our case here), where the user specifies input parameters such as the threshold and the FWHM of the gaussian. We used the method to find stars in the image that has FWHM of ≈ 5.5 pixels and their brightness density amplitudes is greater than 4σ.
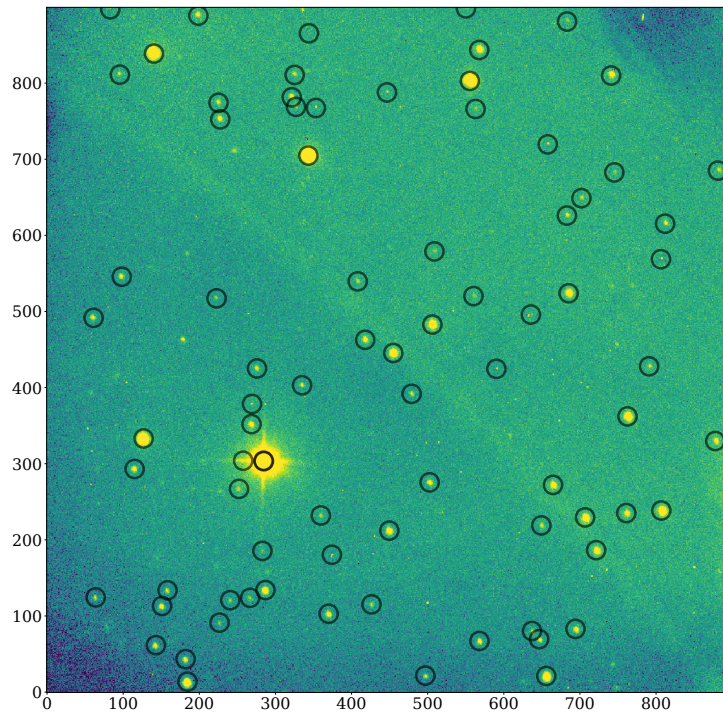

Figure 27: Identified stars by using DAOStarFinder method are marked with black circle

Calibration Stars

As mentioned earlier, we need to use comparison stars to minimize the atmospheric effects. Ideally, it is better to use as many comparison stars as possible to separate intrinsic stellar variability from atmospheric effects. In principle, all stars suffer from the same atmospheric effects. However, the occurring changes vary with color. Therefore, we select a sample of stars for calibration that have a similar brightness and color over different bands as PTFO 8-8695 and are furthermore neither saturated nor intrinsically variable. The selected stars are listed in Table 4.2.2.

One should consider the fact that depending on the field of view, there are always limitations in the availability of good comparison stars that fulfill above mentioned criteria. PTFO 8-8695 is a particularly very red star ($V - K = 4.903$) and no star in the field of view is even close to this color. Additionally, most of the visible stars that are bright enough are part of the young stellar association 25 Ori which means they are generally active and hence variable themselves.

We chose stars that have similar brightness, $1-2$ difference in Rp magnitude to our object, and also has close color to our objects in several color bands. We select the eight stars as comparison stars which represent the best possible match to our target. Their Gaia ID, color, and magnitudes are listed in Table 4.2.2. Their position in the field of view is indicated in Fig. 28.

Table 3: Selected comparison stars for the calibration of the LCO light curve. Parameter taken from the *Gaia* catalog DR2 (Gaia Collaboration (2018))

| Object	Gaia ID	Ra (J2000) [°]	Dec (J2000) [°]	G_{RP} [mag]	$G_{BP} - G_{RP}$ [mag]
PTFO 8-8695	3222255959210123904	81.281484	1.5734303	13.9618	2.52953
calib1	3222255959209939200	81.2763260	1.57748	14.7596	0.9839
calib2	3222257604180874880	81.315029	1.612898	13.1199	0.81987
calib3	3222257745916330240	81.272273	1.6106537	12.848	0.9906
calib4	3222257471038421504	81.29376	1.599760	12.207588	1.332
calib5	3222255787411256960	81.2437198	1.552897	14.5703	1.06128
calib6	3222256027929421568	81.249597	1.5659271	14.6459	1.32169
calib7	3222210363837122048	81.3148374	1.5607262	12.8782	1.69474
calib8	3222208645850209792	81.307889	1.52800	14.4971	1.24174
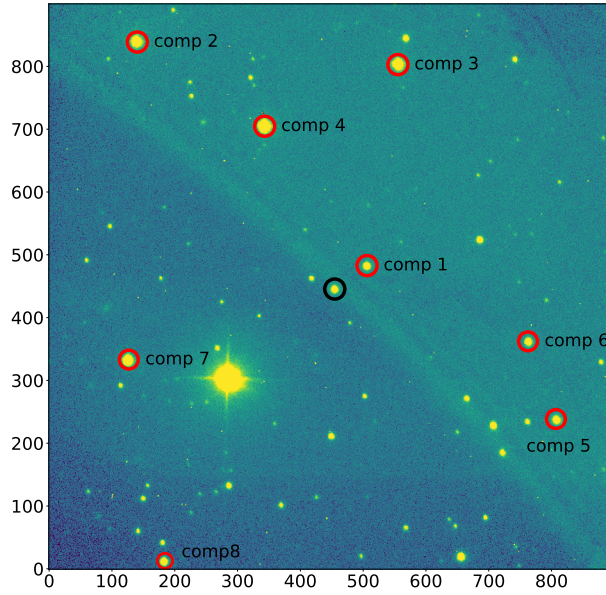
Figure 28: One of the images with the target and the selection of comparison stars indicated (black and red circles, respectively).

Optimal aperture size

To minimize the effect of noise in the extracted light curve we need to use an optimal aperture size for all objects. The optimal aperture size is a compromise between being too small (covering enough of the stellar flux) and too large to not add too much background noise. And that light contamination from nearby sources has to be avoided, too. Therefore, optimal aperture size helps to minimize the remaining scatter due to the noise and the effect of cosmic.

There are several different ways to determine the optimal aperture size. The method we use here is to measure the standard deviation in the light curve of the target for a range of aperture sizes and to find its minimum.

We did relative aperture photometry on our images by using a range of aperture sizes from 2 to 15 pixels in steps of 0.5 and we use the same aperture for all stars in each step. We also removed sky background from

obtained counts by using a 5.0 pixel annulus around each object. This will be explained in the next section. The target light curve is then calibrated with an averaged light curve of all calibration stars. We note that we normalize all calibration star light curves to their respective median before averaging them. We note further that we calibrate the target light curve with the average calibration light curve, both normalized to their median. The standard deviation of the resulting target light curve is plotted against its corresponding aperture in Fig. 29. The minimum of the resulting distribution is for an aperture of 4.0 pixel which we then adapt for all further steps.

We noticed that the used aperture is smaller than our target and some calibration stars too, but since we are interested in the relative change in flux rather than absolute value, we are safe to use a small aperture.
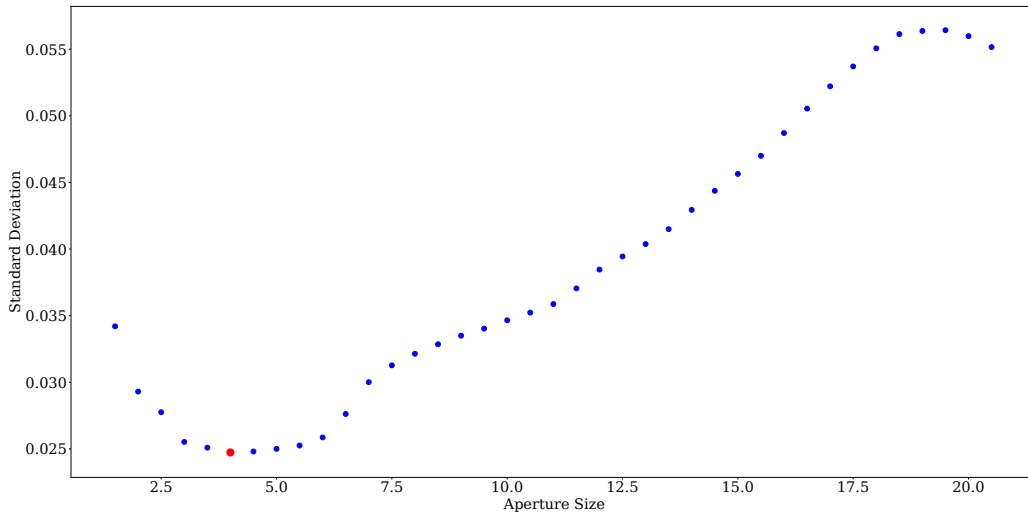

Figure 29: Measured standard deviation for a range of different aperture sizes. The optimal aperture size is marked red.

Sky background measurements

After calculating the counts inside of each pixel, by doing aperture photometry with optimal aperture size, we need to remove sky background from the counts of target and comparison stars. For doing so, one needs to measure the sky background per pixel around each object individually and subtract it from the source's counts inside the aperture. This step is necessary since we have background variations across the total image as can be seen in Figure.31. We estimated the sky background per pixel by using the Annulus Function of Photutils which sum up the total counts inside an annulus around each source for a given width. We use the width of $4.0 - 5.0$ pixels for our stars and then divide it per aperture area. In our dataset, there are plenty of noises and cosmic rays close to each source. To avoid including them in sky background calculations, we shifted our annulus apertures within few pixels for each image carefully to a reasonable distance from the star's profile.

Atmospheric variations and calibration

The 85 images taken with LCO span about the duration of one night in which the target crosses a large fraction of the night sky. This causes a large variation in air mass in the course of the observation. However, thanks to the aperture choice we made, it is not visible in the un-calibrated light curve (Fig 32). For larger apertures this effect is visible again, and, becomes the dominant trend in the data, see Fig 23 where we over plotted the light curves extracted with an aperture of 10 and the approximate airmass during the observation.

We noted in our selection criteria for calibration stars above that they are ideally without intrinsic variation. However, it is tricky so far to tell if they are or not and we need to check this. Possibly, stars can be not intrinsically variable but the counts we detect from them change due to the atmospheric effects. It can be seen from the Fig.32, that target and comparison star both show similar patterns in their light curve which are not intrinsic to them. This can be due to seeing effects that are stronger in smaller aperture sizes. In Fig 32, we show the light curves of the calibration stars, each calibrated by the average of all other calibration stars.
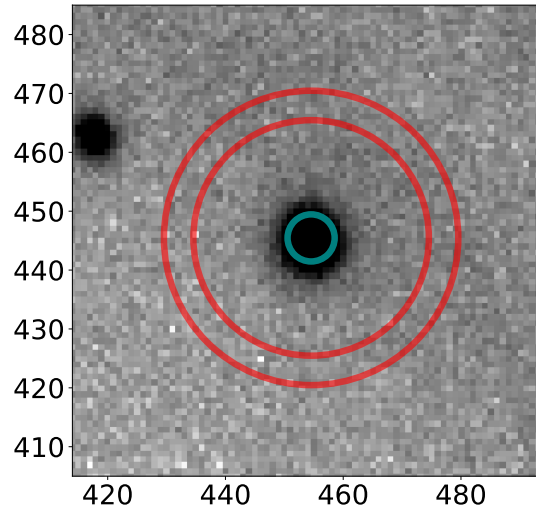
Figure 30: Cut out of one image around PTFO 8-8695. The red ring marks the outer and inner border for the chosen annulus aperture and the green circle denotes the chosen aperture for star.
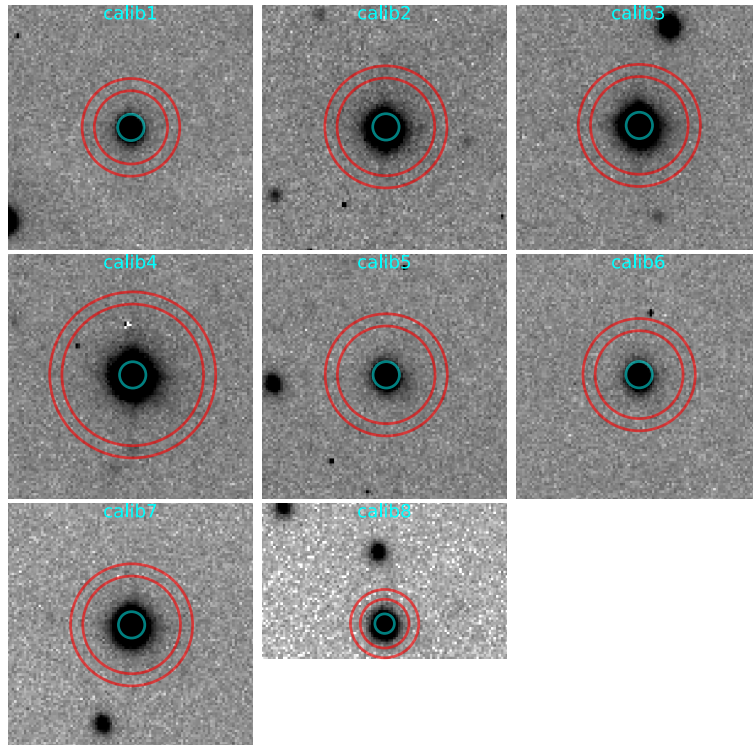

Figure 31: The red ring marks the outer and inner border for the chosen annulus and red green ring denotes the chosen aperture.

By looking closer at Fig. 33, we find that the calibration stars themselves are not as constant as we wish them to be. Therefore, we calibrate first each calibration star with the help of the remaining ones,
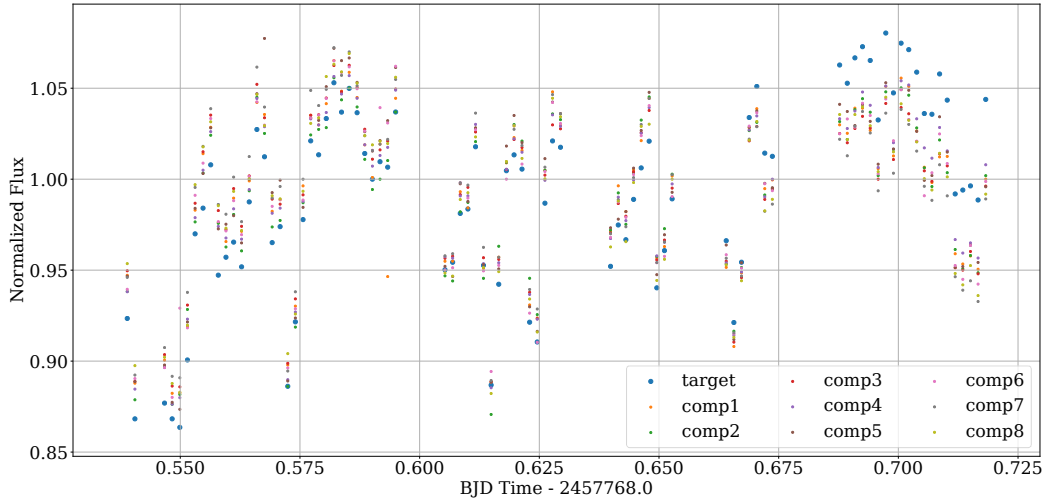
Figure 32: Raw and non calibrated flux of target and comparison stars. Target is marked with blue circles.

identify a linear trend in the residual, and remove this trend from its uncalibrated light curve. Such prepared calibration star light curve is, in good approximation, free of intrinsic variation of the calibration stars. Those we use them for the calibration of our target.

Figure 33: Calibration stars light curves before removing the linear trend. Each star is calibrated with the other remaining calibration.

With all those corrections at hand, we finally produce the calibrated target light curve, as displayed in the Fig. 34. As we can see in the figure 34, the transit is superimposed on the stellar activity sinusoidal variations which w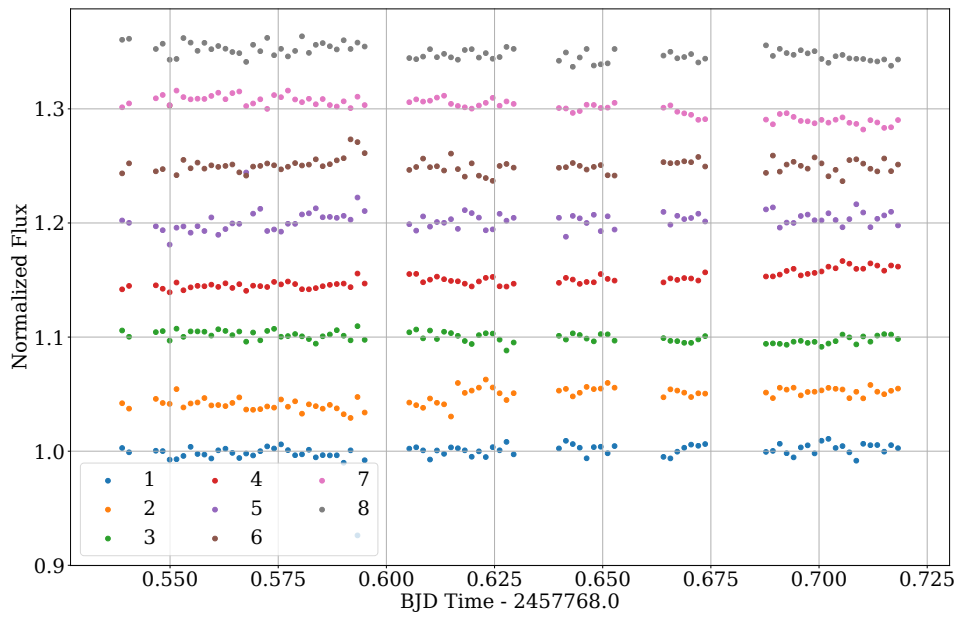e expect it from this star according to the previous works. However, this trend is a linear trend to a good approximation and we can remove it.
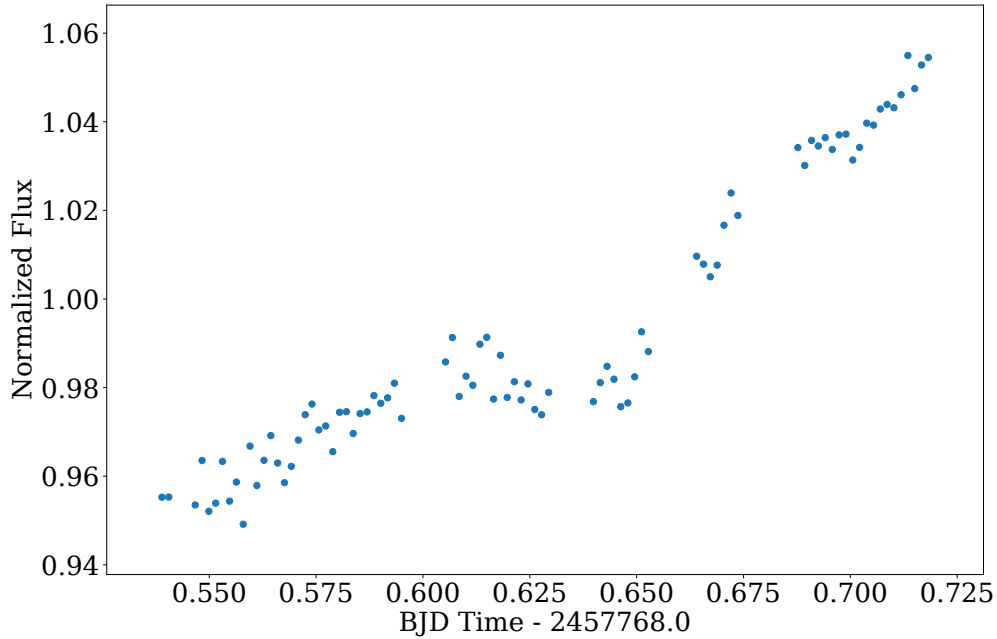
Figure 34: The light curve of PTFO 8-8695 after calibration process with the stellar trend.

We fitted a simple linear curve on the light curve. The line we used for detrending is :

$$y = 0.52737964 \cdot x + 0.953$$

The light curve is divided to this line and 1.0 is added to it for correcting the scale. The final light curve with depth of 3% is displayed in Fig. 35.

Figure 35: Extracted light curve of PTFO 8-8695 after removing the trend, showing dimming event with depth of $\approx 3\%$

5 Analysis

5.1 Transit model

One way to analyze the light curve of a star-planet system showing a transit is to fit a transit model, a theoretical calculation of a light curve that accounts for the nature of star and planet and the orbital properties.

Fitted parameters can provide system parameters such as the inclination of the orbit towards the line of sight i, the ratio between star and planet radii R_p/R_*, and the transit midpoint T_0.

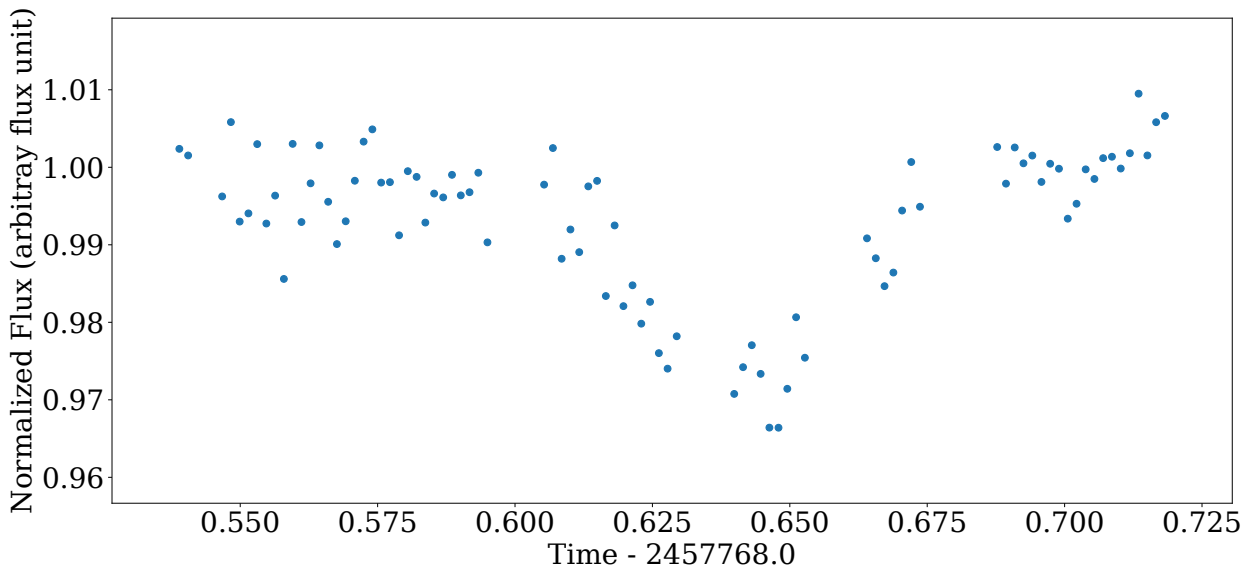We fit a model to accomplish two goals. The first goal is to identify whether the observed dip in our light curve is the one caused by the proposed planet in previous work on this object. To do so, we calculated a transit model with parameters derived by Raetz et al. (2016) to see whether the model reproduces (closely but not perfectly) the observed shape. Second, we are interested to examine whether the transit midpoint has shifted compared to the predicted time of transit.

Hereby, we use the python implementations of the analytical models described by Pál (2008) which is used in the `Pyastronmy package`.

The Pál (2008) model requires information about center-to-limb intensity variations since the shape of an observed transit depends also on the center-to-limb brightness variation of the star. Therefore, limb darkening is a key ingredient to all transit modeling and its effect has to be taken into into account.

We choose a quadratic description of the limb darkening for its wide range of applicability across different stellar colors and band passes, shown in equation.

$$I(\mu)/I(1) = 1 - c_1(1 - \mu) - c_2(1 - \mu)^2, \qquad \mu = cos(\theta) \tag{13}$$

We obtain the two coefficients, c_1 and c_2, from the Exoplanet Characterization ToolKit (ExoCTK[9]). ExoCTK calculates the coefficients based on a synthetic model spectrum of the star in a relevant band pass using Sing (2010) coefficients. We use the Kurucz ATLAS9 model grid (Kurucz 2014) for the selection of spectrum from given parameters. For the selection of a synthetic spectrum in the model grid, we provide parameters listed in the table which were taken from Kounkel et al. (2018) and Raetz et al. (2016). Since the metallicity of this star has not been determined yet, we set it to solar metallicity. The bandpass we choose to calculate Limb darkening coefficients is according to the wide optical R filter of Andicam Camera which the filter curve is shown in the Fig. 36. We used a box filter, as the closest available approximation, in the ExoCTK toolkit with the wavelength range according to the filter curve as shown in the figure. The results of the limb-darkening calculation are listed in Table 4.
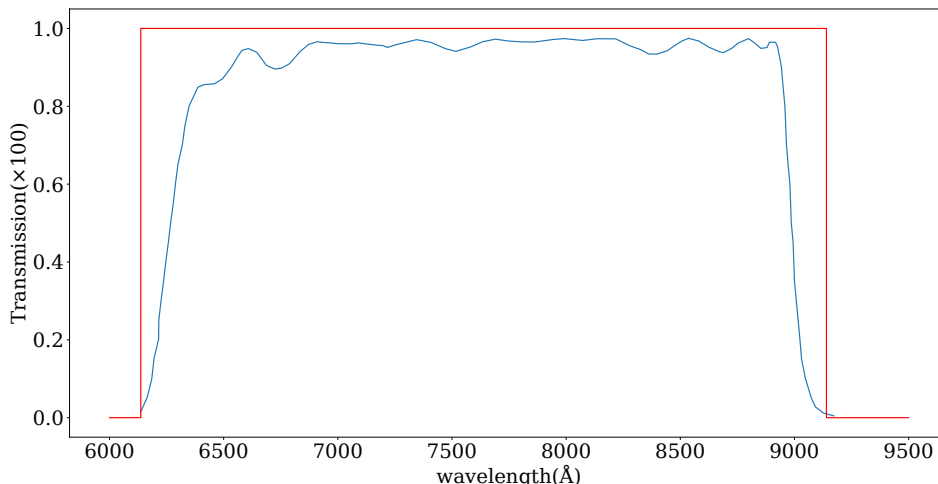
Figure 36: The blue curve shows the filter curve for Wide R band filter of Andicam camera. The red line shows the box filter curve in ExoCTK toolkit with the wavelength range of 6137 to 9140 Å.

The transit model has the following parameters: the mid-transit time T_0, the orbital period P, the radius ratio $R_p/R_* = p$, the semi-major axis in stellar radii a/R_*, the orbital inclination i, and the quadratic coefficients c_1 and c_2. We use the findings of Raetz et al. (2016) as values for orbital period, semi-major axis

---

[9] `https://exoctk.stsci.edu`

Table 4: Limb darkening coefficients and the input parameters for calculating them

Parameter		value	Ref
T_{eff}	[K]	3832 ± 15	Kounkel et al. (2018)
$\log g$		4.65 ± 0.05	Kounkel et al. (2018)
μ_{min}		0.0	minimum angle to consider while calculations
λ_{min}	[μm]	0.6137	
λ_{max}	[μm]	0.9140	
c_1		0.277 ± 0.035	
c_2		0.39 ± 0.041	

and radius ratio as input parameter. Inclination has been set according to van Eyken et al. (2012) work. All the mentioned parameters are listed in Table 5.

Table 5: Input parameters for transit modeling

Input parameters Parameter	unit	value
P	[d]	0.4483973 ± 0.000040
i	[°]	61.8 ± 3.7
a	[R_*]	1.80629 ± 0.00036
R_p	[Rjup]	$1.87 + 0.08 - 0.09$
R_*	[$R_\odot$]	1.00 ± 0.04
R_p/R_*		0.18784

In order to derive the transit midpoint and the radius ratio by fitting a model to our light curve, we set T_0 and p, as free parameters while fitting. However, there are evidences that the planet moves on a precessing orbit. So once we set inclination as a free parameter addition to the T_0 and p, and run the model. The value we got for inclination is about $\approx 61.4°$, which is somewhat similar to the value listed in the van Eyken et al. (2012).

In the second run, we fixed all the parameters, including i, and set T_0 and p as free parameters. Best fitting parameters for the transit mid time and p are as follow:

$$T_0 = 2457768.6413466 \qquad \text{and} \qquad p = 0.183$$

The transit depth is about $\approx 3.0\%$ and it has the duration of $\approx 1.8\,\text{h}$. The extracted light curve and the fitted model are plotted in the Fig. 37.
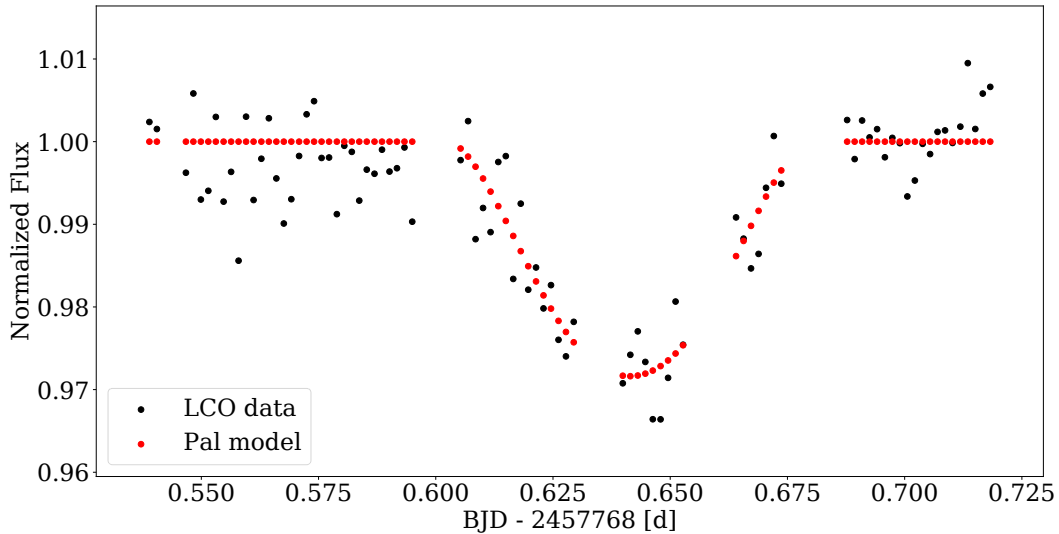
Figure 37: Extracted light curve of PTFO 8-8695 (black dots) and the fitted Pàl model (red dots) with mentioned input parameters listed in Table 5. The dip with the depth of $\approx 3.0\%$ is evident in the light curve.

Since our light curve inhibits a relatively large scatter, we estimate the confidence interval, using the Pyastronmy package, for the derived T_0 as an indicator for its reliability. The package uses a χ^2 minimization

to estimate the goodness of the fitted model on the extracted light curve as the sum over the differences of N data points between model E and observation O as

$$\chi^2 = \sum_i^N \frac{E_i^2 - O_i^2}{E_i^2}.$$

It uses linear extrapolation to find points in x axis (our case T) that have a given offset from the minimum χ^2. The resulting χ^2 is plotted against T_0 (cf. blue line in Fig. 38). The result is a quadratic distribution for χ^2 around the minimum χ^2_{min} at $T_0 = 24557768.6413466$. A corresponding 1σ error is given by the points T_σ at which

$$\chi^2(T_\sigma) = \chi^2_{min} + 1.0 \cdot \chi^2_{min} = 2\chi^2_{min}$$

We find $T_{\sigma,1} = 24557768.631461$ and $T_{\sigma,2} = 24557768.650635$ (cf. the dashed red lines in Fig. 38). This corresponds to an uncertainty in the transit midpoint of $\Delta T = 0.009\,\mathrm{d} = 13.8\,\mathrm{min}$.
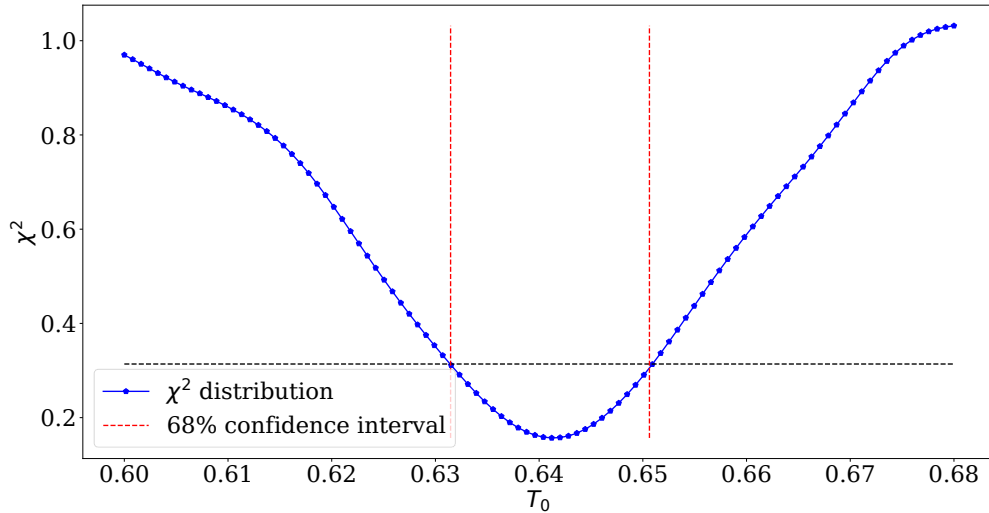

Figure 38: χ^2 plot versus transit mid time. The 2 vertical red lines show the interval corresponding to a 1σ error or 68% confidence. The black line indicates the offset corresponding to 68% confidence from the minimum value of χ^2.

39

5.2 Light curve analysis

We have seen from our review of previous work on this system (c.f. Section. 2) that different individual works came to different and partially conflicting conclusions. In this section, we will investigate the timing of the observed dips in newly acquired LCO and TESS data based on the various ephemerides reported. According to the previous works on this system, the transit in the system appeared earlier than predicted or even disappeared in the predicted time. Therefore, it is important to see whether the observed transit in our data (LCO and TESS) has occurred in the predicted time or not. Thus, we conducted a timing analysis on the data by calculating the phase of the LCO's dip and phase folding TESS light curve based on the available ephemerides in the literature. The results of the calculation for both data sets with different ephemerides are presented as follow.

The Raetz et al. (2016) ephemeris

We recall the derived ephemeris by Raetz et al. (2016):

$$T_c[BJD_{TDB}](E) = (2455543.9420 + E \times 0.4483973) \text{ d.} \tag{14}$$
$$\pm 0.0007 \pm 0.0000004$$

Comparing the predicted time of a transit based on this ephemeris with the observed time of the dip in the LCO data shows that the dip occurs at a phase of $\varphi_{\text{lco,Raetz}} = -0.447 \pm 0.005$ for the epoch $n = 4961$. Since we subtract the observed time from calculated time, negative phase means the observed dip happened later than predicted. Also, we phase fold the TESS light curve with this ephemeris and, as shown in Fig. 39, several different dips and features become apparent in the light curve.
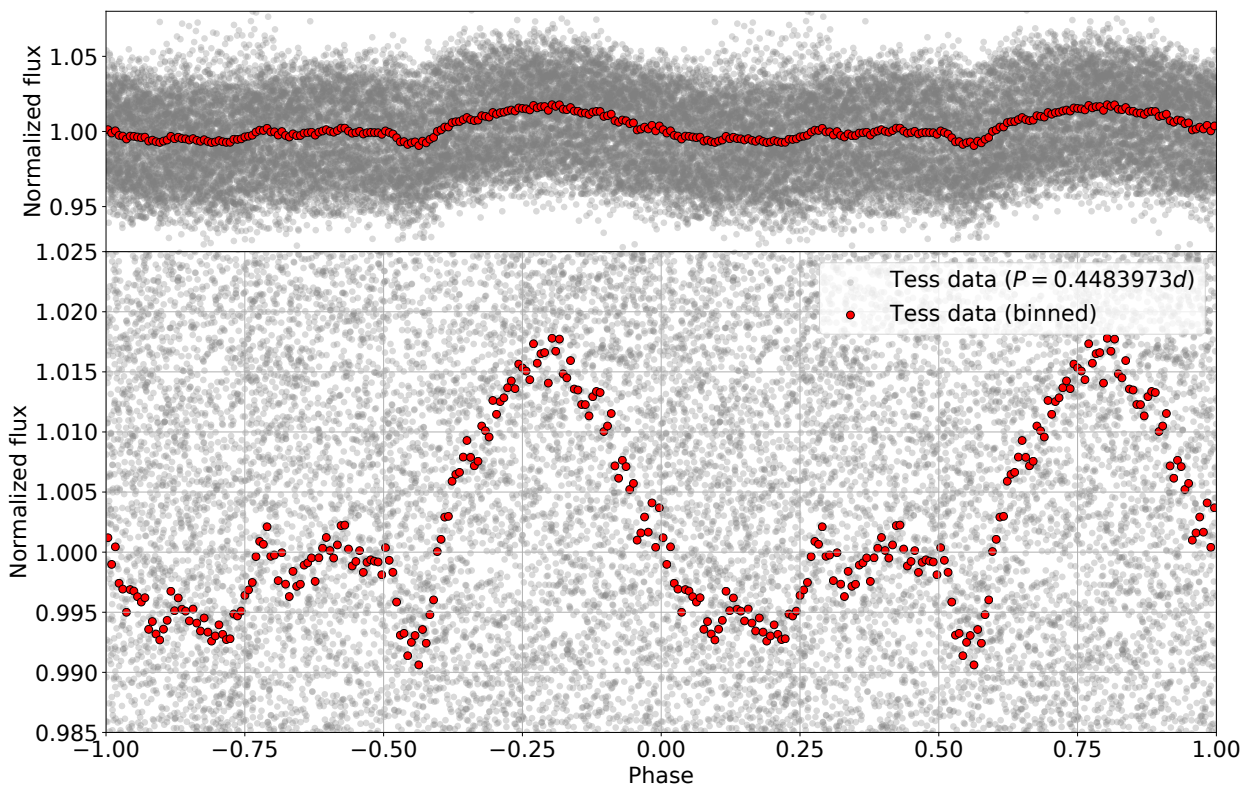
Figure 39: The phase folded light curve with derived planetary period in Raetz et al. (2016, see legend, gray). Upper and lower panel, both show the same data, the original TESS lightcurve from Fig. 22 in gray and binned (after phase folding) to 150 data points in red. The lower panel is an enlarged view of the upper panel to highlight small scale variabilities.

Several light curve features in the phase-folded light curve at around phases of -0.50, 0.25 and 0.35 exist. For better visibility Fig. 40 showes zoomed plots around those. In the left panel of Fig. 40, a dip with the depth of $\approx 1.0\%$ occurs at around the phase of ≈ -0.45 with a duration of about 0.1 in phase space, or 1.08 h. We will refer to this dip in the following as the dip I.

In the right panel, there is a shallow dip at a phase of ≈ 0.2 with a depth of about 0.5% (This dip will be referred as the dip II below). An estimate of the duration from the plot gives about ≈ 0.2 in phase

Figure 40: Zoom-in plot of the phase folded light curve with the ephemeris of Raetz et al. (2016). Data and color coding as in Fig. 39.
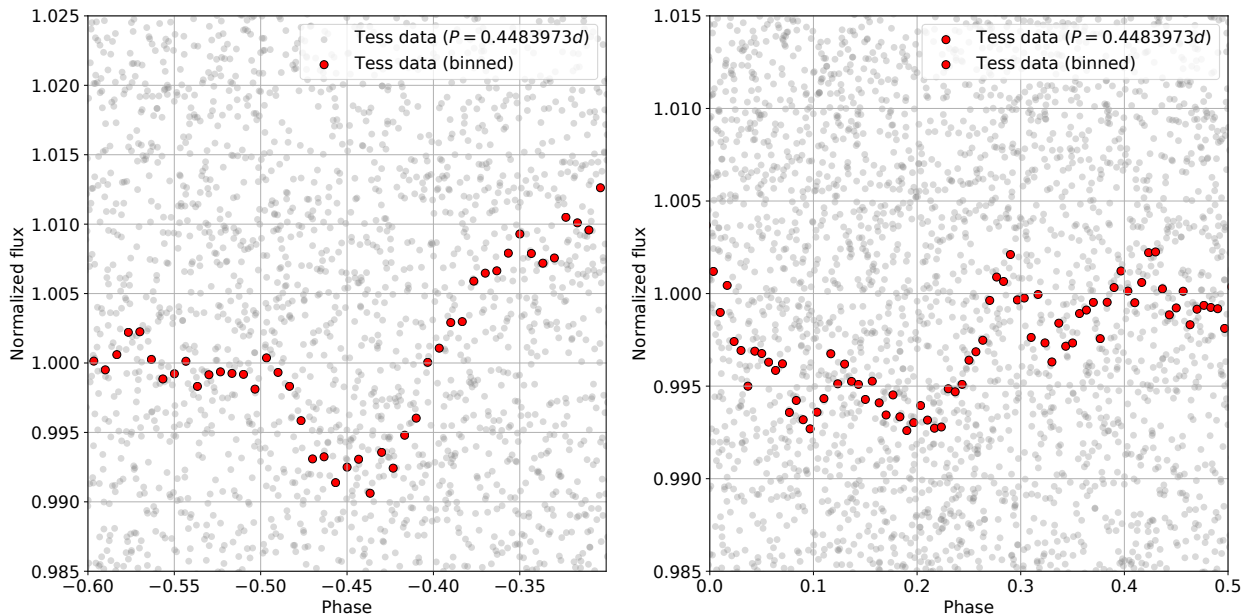
space. Between the phase of 0.3 and 0.4, we observe another shallow and asymmetric variability that is very irregular and have duration of 0.1 in phase. Its depth is not clear from the plot and it might be only due to short term variability. At around the phase of 0.1, we also observe another variability that is to weak and insignificant to deserve the name. Its depth of less than 0.05% is much weaker than other dips and it has a very short duration compared to other dips.

The Yu et al. (2015) ephemeris

One of the hypotheses for observing transits in different times suggested by Yu et al. (2015), as mentioned earlier, is the change in the period of the transiting object. In their observed transits, dimming events started to occur earlier than expected in their second observing run. Thus they proposed that this might be due to the decrease of the period of transiting object over time. However, as Tanimoto et al. (2020) later mentioned, the dip happened earlier is a different dip. By looking at their dips (c.f. Fig. 9), one can see that the dips at phase -0.1 is shallower and shorter compared to the dip at phase 0.0 (c.f. Fig. 9). However, with the assumptions that the dips are changing depths and shapes, Yu et al. (2015) designed their ephemeris with period decay in a way that explains the both their sets of data. This means, their P_0 probably refers to the period of the dip that is at around the phase 0.0. So it would be interesting to see what the phase of the dips will be if one does not consider the decrease in the period over time. With all of this in mind, we analyze the phase of the dips in the data once with the assumption that the period is decreasing and once with the assumption that the period is constant and thus we don't include the decrease part in our calculations. (This means we take only the constant part of Eq. 17 and set $dP/dn = 0$). We recall the non-linear ephemeris of Yu et al. (2015):

$$t_n = T_0 + P_0 n + \frac{1}{2}\frac{dp}{dn}n^2,$$ (15)

where

$$T_0 = 2455201.790 \pm 0.006\,\text{d},$$ (16)
$$P_0 = 0.448438 \pm 0.000006\,\text{d}$$

and

$$dp/dn = (-2.09 \pm 0.25) \times 10^{-8}\,\text{days epoch}^{-1}.$$

For the case that the period is decreasing, we need to derive the epoch of the transiting object during LCO observations for the non-linear ephemeris. We solve Eq.(15) for n and find $n = 5724$. The corresponding

phase of the LCO dip for this epoch is about $\varphi_{lco,yu} = -0.75 \pm 0.12$ which considers the error on the parameters in the equation and period decrease rate. We perform a similar calculation for the TESS light curve. However, this time select one of the transits covered during the TESS baseline, starting at $T_{BJD} = 2458468.3$ and ending on $T_{BJD} = 2458490.05$. For phase-folding the TESS light curve with the non-linear ephemeris, we also calculate at which epoch the transiting object were during TESS observation. There are several dips in the original and non-phasefolded TESS light curve and by picking one of the transit times, we can have aa rough estimate of the epoch and with that the current period. For the epoch of $n = 7287$, the estimated period based on the (15) is $P_{yu} = 0.448286 \pm 0.000019$. In the resulting phase-folded light curve (as shown in the Appendix in Fig. A.1), the dip I occurs at around the phase of -0.57.

However, if we don't include the decrease in the period over time, the calculated phases are somewhat different. For the LCO's dip, the phase based the first part of the Eq. (15) (T_0 and P_0) for $n = 5724$ is about $\varphi_{lco,yu2} = 0.02 \pm 0.08$. Additionally, we phase fold the light curve with the T_0 and P_0 in the Eq. (17) as well. As shown in the Appendix in Fig. A.2, the dip I is at around the phase -0.05 and the dip II is at around the phase -0.4.

Tanimoto et al. (2020) Ephemeris

Addition to previous ephemerides, we also used the ephemeris in the new study of the system done by Tanimoto et al. (2020) published and the derived ephemeris which is based on the 5 years of observation, might be more accurate. Thus we use their ephemeris to calculate phases as well. They proposed the following ephemeris with a constant period as:

$$T_{0[BJD]} = (2455543.943 \pm 0.002)\,\mathrm{d} \tag{17}$$
$$P = 0.4483993 \pm 0.000006.$$

The dip in the LCO data is at the phase of $\varphi_{LCO,\,yuta} = -0.422 \pm 0.008$ based on this ephemeris. Interestingly, in the phase folded TESS light curve based on this ephemeris, the dips and features occur at similar phases compared to the Raetz ephemeris (c.f. Fig. 39) but show a slight missmatch towards the phases derived based on the Yu ephemerides (c.f. Appendix Fig. A.3).

For having an idea of exact phases and also comparing them with other phase folded light curves, a zoom-in plot is shown here in the Fig. 41. The mentioned dips have shifted by ≈ 0.02 in phase, so the dip I is at around the phase -0.47. And the dip II is at around the phase 0.18 in the phase folded light curve. As last point, one should note, that since the stellar activity signal does exist in the TESS -folded light curve, the mentioned depth for each transit, is just an estimate and the accurate transit depths might be different.
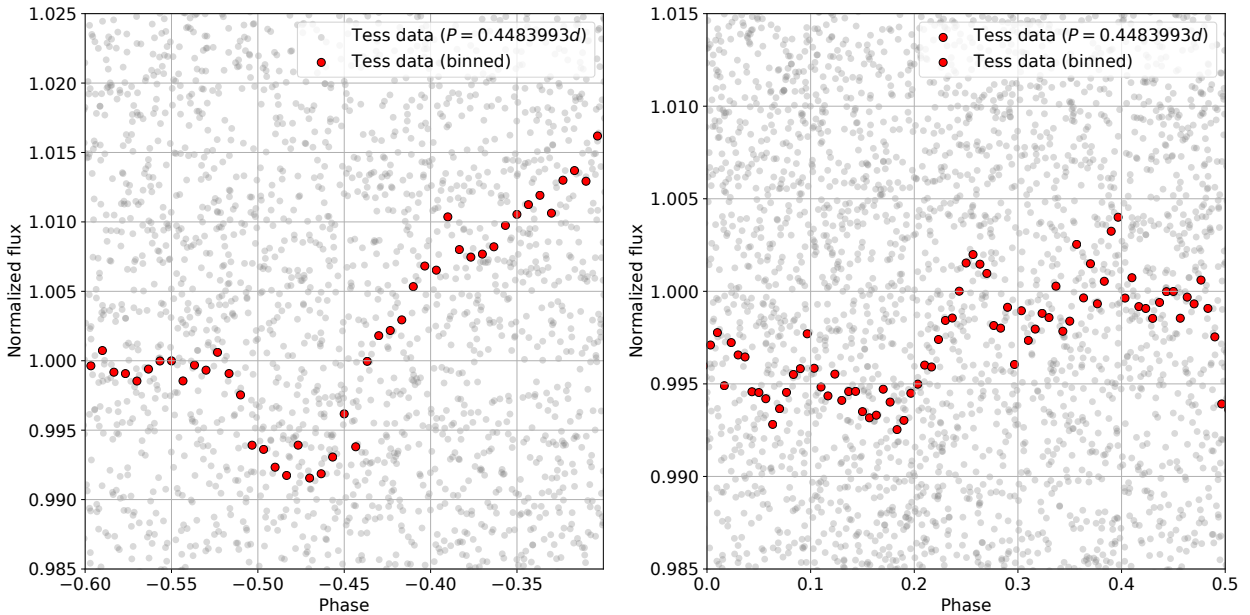

Figure 41: The Zoom-in plot of the phase folded light curve with the ephemeris of (Tanimoto et al. 2020). The data binned to 150 points (red).Data and color coding as in Fig. 39.

For having a general overview of the ephemerides and the corresponding phases, a table with the results of timing analysis is shown in the below.

Table 6: Overview of the ephemerides from selected papers and the results of the timing analysis for observed LCO and TESS transits.

Ephemeris	Type of ephemeris	T_0	P_0	dP/dn	LCO		TESS dip I
		[BJD$_{TDB}$]	[d]	$[\frac{d}{epoch}]$	phase	orbit	phase
Raetz et al. (2016)	linear	2455543.9420 ±0.0007	0.4483973 ±0.0000004	—	-0.447 ±0.005	4961.0	-0.45
Yu et al. (2015)	non-linear, decay	2455201.790 ±0.006	0.448438 ±0.000006	$2.09E^{-8}$ $\pm0.25E^{-8}$	-0.75 ±0.12	5724.0	-0.57
Yu et al. (2015)	non-linear, no decay	2455201.790 ±0.006	0.448438 ±0.000006	0.0	0.02 ±0.08	5724.0	-0.05
Tanimoto et al. (2020)	linear	2455543.943 ±0.002	0.4483993 ±0.0000006	—	-0.422 ±0.008	4961.0	-0.47

5.3 Analysis of spot distribution

There are evidences that WTTS have large and long-lived starspots (e.g., Mahmud et al. 2011). The spot modulation signal is clearly visible in the phase folded TESS light curve, see Fig. 42. It is caused by stellar rotation with a period of $P = 0.49927$ d (Raetz et al. 2016).
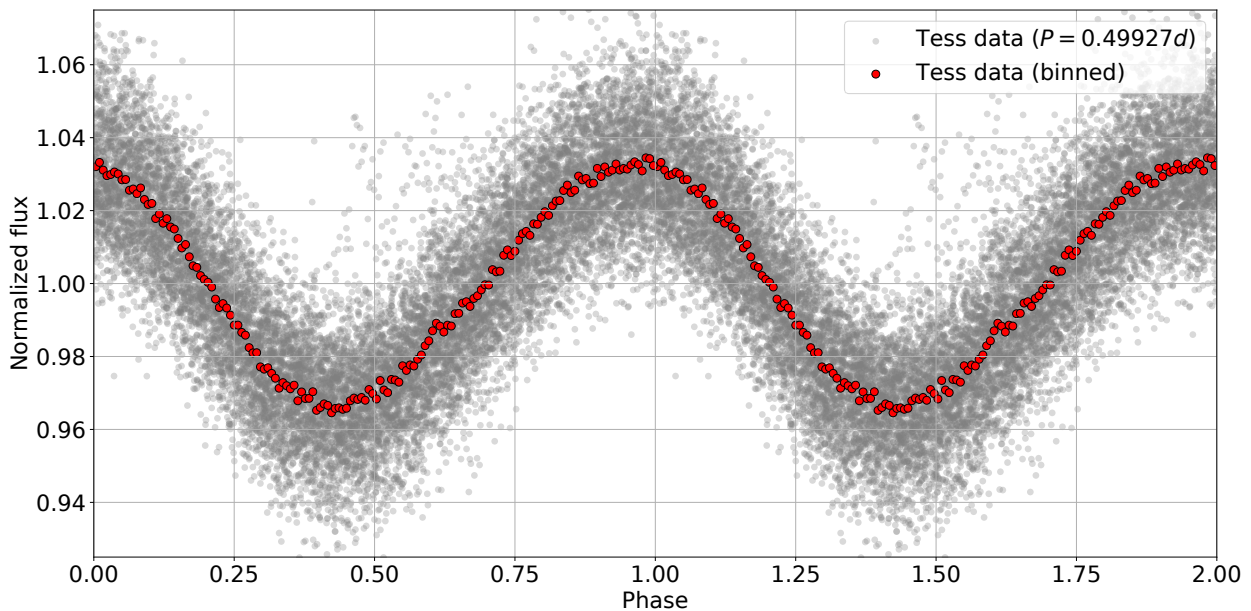

Figure 42: The phase folded light curve with derived stellar period in Raetz et al. (2016, see legend, gray) and the data binned to 150 points (red). The spot-modulation signal with peak-to-peak amplitude of 8% evident in the light curve.

Spots in very late type stars are believed to survive for long times more or less unchanged due to the strong magnetic fields that are causing them. In order to examine if the spot distribution and amplitude has been remained persistent since the original detection of this system by (van Eyken et al. 2012) and between December 2018 (TESS observation) and April 2019 (STELLA observations), we have compared the STELLA light curve with TESS light curve.

We compare the variability amplitude, which indicates whether the spot coverage has changed during this time. A difficulty arise from the very different sampling rate and base line for the TESS and STELLA observations. Thus, we shift the TESS data points in time by integer multiples of the rotation period of $P = 0.49927$ d. to times covered by the STELLA data in order to allow comparison. As can be seen in Fig. 43, the peak-to-peak variability of the fluxes are similar for TESS and STELLA, despite the significant differences in data coverage. In the middle and lower panels, e.g., times between 2457768.796 and 2457768.798 or 2457768.817 and 2457768.822, it is apparent that the STELLA fluxes follow the sinusoidal pattern of the spots clearly outlined in the TESS data.
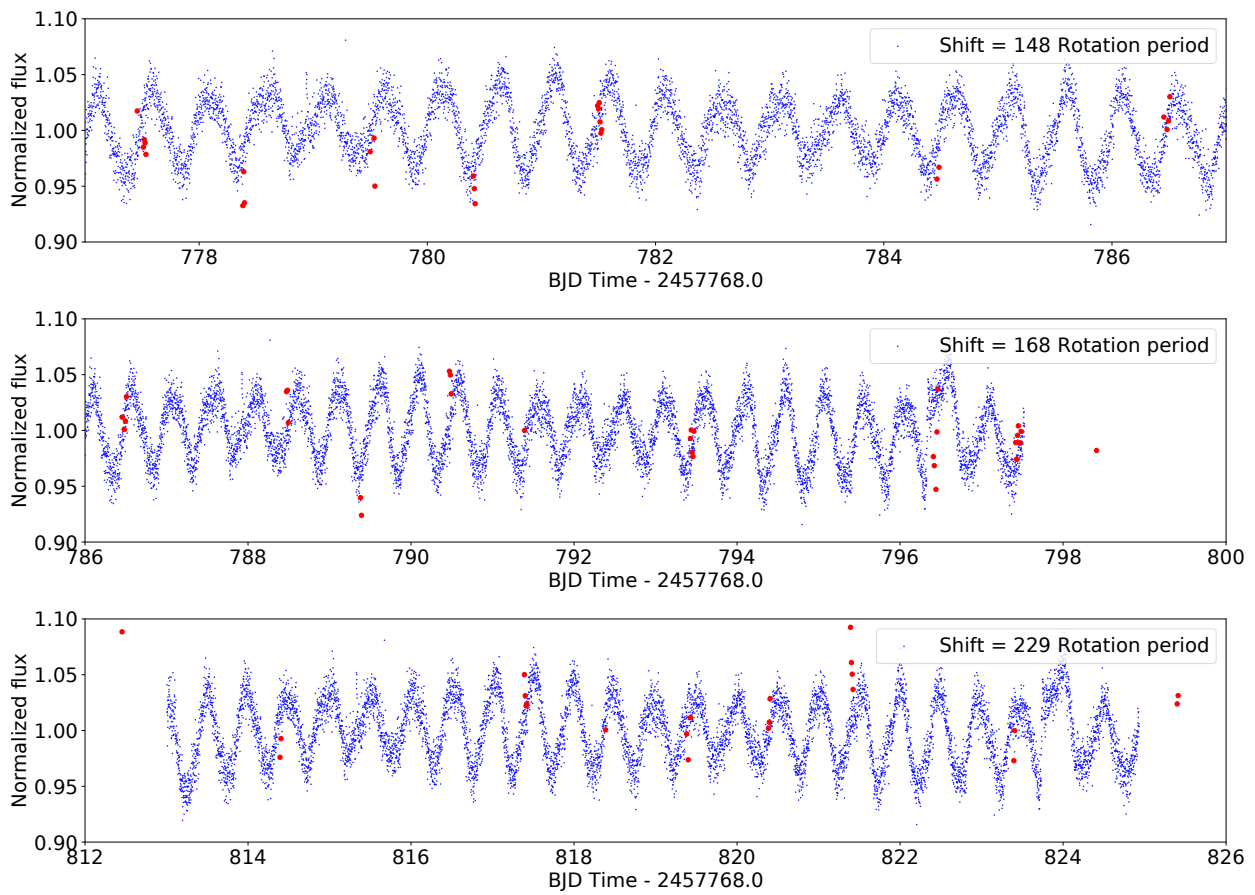
Figure 43: STELLA and TESS light curve overplotted on each other. The blue and red dots indicates the TESS and STELLA fluxes respectively.

This indicates that the pattern of the stellar spots has stayed relatively persistent between December 2018 and April 2019. However, future observations will be useful to show whether the future distribution of spots changes or not.

6 Discussion

As we have seen, this system is more complex than originally thought and several dips and phenomena are evident in the light curves, making it harder to reveal its true nature. Despite that, our data still allows us to explore this system and to examine a few scenarios for the observed dips. Given the variety of observations, it is important to clarify if the reported dips across various studies originate from the same phenomenon.

6.1 Are the observed dips related?

After our timing analysis on the data, one of the first questions that come to mind is whether the observed dips in the TESS and LCO data are related. One way to investigate this is by comparing their shapes, phases, and depths. One reason for the difference between the depths of dips could be the difference between bandpasses of TESS and LCO photometers. While not being identical, both have a somewhat reddish bandpass around $600-1000\,$nm. It is unlikely to be the reason.

As can be seen in Table 6, the dip in the LCO data with a depth of 3% and a slight V-shape occurs around phases of -0.447 and -0.42 based on the 2 linear ephemerides in Raetz et al. (2016) and Tanimoto et al. (2020), respectively. Given the range of uncertainties in the calculated phases for both ephemerides ($\sim 0.005-0.008$), this shift cannot be explained simply by the uncertainties in P and T_0. This shows, based on those two linear ephemerides with a time difference of 4 years between them, that the LCO dip does not occur at the predicted time but phase shifted by $\approx 0.4-0.45$. One reason for this phase shift can be the change in the period of the transiting object over time. However, calculating the phase of this dip based on the non-linear ephemeris of Yu et al. (2015), that suggests the decrease in the period, also does not agree with the observed timing of the dip and shows a phase shift of -0.75 ± 0.12 for the epoch of 5724. We pointed out already that this particular ephemeris was created based on a questionable scenario and conclusion based on it have to be adopted carefully.

However, we find that dip I, identified in the TESS data, and the dip in LCO show very similar results when subjected to the ephemerides of Raetz et al. (2016) and non linear ephemeris of Yu et al. (2015) without decrease. Additionally, their phase difference is about 0.05 for Tanimoto et al. (2020) ephemeris as well. (c.f. Fig. 40, Fig. A.2, Fig. 41, Table.6)

The fact that the first dip in the TESS data and the LCO dip have similar phases based on the Raetz et al. (2016) and non linear of Yu et al. (2015) with decay cut off, and a slight V-shape can be interpreted that both arise from the same phenomena in the system, which only has a slightly different period than previously reported. However, since different quasi-periodic variabilities has been observed in the system by previous works, and there is evidence for the change in the shape of the dips, these arguments alone do not prove that the dips are related.

6.2 Are the observed dips not related?

There is also the possibility that the observed dips are not related and are representing different phenomena in the system. One indication could be the small difference between the duration and depth of the dips. While the depth of the LCO dip is about 3.0%, Dip I in the TESS data just has 1.0% depth. Moreover, the duration of dip I is about 0.1 in phase space, i.e., $1.08\,$h, which is about $0.72\,$h shorter than the observed dip in the LCO data. Moreover, their phases differ about 0.05, based on the Tanimoto et al. (2020) ephemeris. Additionally, if we assume they are related, something has to have caused the change in depths from 3.0% to 1.0% between January 2017 to December 2018. But then the dips with depths about 1.0% or less should not be present in the light curve before 2018. However, dips with depths of 1.0% and 1.7% (Onitsuka et al. 2017) in red and infrared, respectively, and dip with depth of 0.6% in 2013 (Ciardi et al. 2015) were observed.

Thus, it is more probable that the observed LCO dip and dip I in TESS data are not related. It is very plausible that they are due to different phenomena and only have very similar periods.

We note that the mentioned phases may vary slightly when calculated for a different orbit. However, the important point is the observed phases for both LCO and TESS data remains significantly different from zero with Raetz et al. (2016) and Tanimoto et al. (2020) ephemerides either way.

6.3 Are the observed dips due to a planet?

The originally proposed explanation for the observed dips in this system is the planetary hypothesis (e.g., van Eyken et al. 2012; Ciardi et al. 2015; Raetz et al. 2016). Due to the fact that the LCO dip shows similar features (3.0% depth, $\approx 2\,$h duration, similar V-shape) to the dips that were attributed to a hot Jupiter before, we investigate this possibility as well.

Recall from the transit model fitting on the LCO data (Sect.5.1) that the transit model for a Jupiter sized planet with previously derived parameters (Raetz et al. 2016) gave a reasonably good fit. Additionally,

the derived radius ratio from the transit fitting is about 0.183599, which is within the error range of the derived radius ratio of 0.18784 by Raetz et al. (2016). Despite that, there is no transit with depth of 3.0% and duration of $\approx 2\,$h in the phase folded TESS data.

One reason for non-existence of such a transit might be the high inclination of potential hot Jupiter during the TESS observations. Precession of the potential hot Jupiter that can cause the variations in the inclinations and with that variations in depth and even disappearance could be the reason for this. However, the nodal precession model of Barnes et al. (2013) has been turned down due to the lack of a secondary eclipse detection by Ciardi et al. (2015) and Yu et al. (2015), the lack of Rossiter-Mclaughlin effect's detection, and lack of variations in the sky-projected rotation rate $v \sin i_*$ (Yu et al. 2015).

Nevertheless, the existence of a smaller sized planet in the system might resolve some of the discrepancies. As mentioned before, Tanimoto et al. (2020) proposed that there could be a smaller planet with radius of $0.36 \pm 0.15 R_{\mathrm{Jup}}$ and a period of $0.4483993\,$d on a precessing orbit with disappearance period of $\approx 1411\,$d. The optical and infrared light curves taken by Tanimoto et al. (2020) are shown in Fig. 15 and among the several identified dips, dip B was attributed to a putative planet, which has the depth of $0.59\% - 0.81\%$ in optical. Comparing our observed dips with dip B, neither the in dip in the LCO data nor the dip I in TESS have the optical depths in this range. This does not match the depth this putative planet would cause.

Furthermore, based on the Tanimoto et al. (2020) ephemeris, neither LCO dip nor TESS dip I have a phase of zero, rather -0.42 and -0.47 phase shifts, respectively. However, the weak and short-term variability around the phases of $0.05 - 0.1$ with the depth of less than 0.5% could be related to this dip B. Since they have proposed a precessing orbit for the planet, it might have a very high inclination during the TESS observations. This, in turn, might lead to shallower depth or even a total transit disappearance.
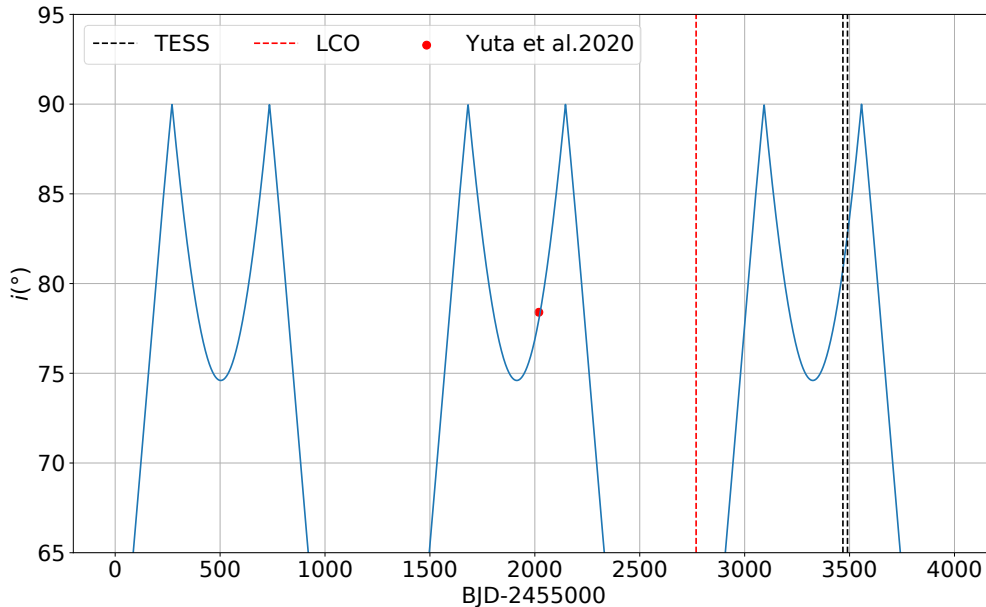

Figure 44: The inclination as a function of time. The time of TESS observations and LCO observations are labeled and shown with dashed lines. The red dot corresponds to the first transit mid time of dip B in the Tanimoto et al. (2020).

We have investigated this possibility by checking the inclination of the putative planet based on the sinusoidal inclination function in their paper. As can be seen in Fig. 44, the transit due to this object should have been present during the TESS observations since the it falls within the appearance window. Thus, the possibility that the short term variability in TESS is due to the putative planet remains. However, as mentioned before, they also proposed a core-halo hypothesis, which refers to a smaller planet with the radius of $0.22 R_{\mathrm{Jup}}$ embedded in dust, as the origin of dip B as well. Although the derived radius and other planetary parameters have large uncertainties, this object might be the cause of the short-term variability between phase of 0.05 and 0.1 since a smaller object would cause a smaller dips. We note that, even though we used the exact Eq. (8) in the Tanimoto et al. (2020), this plot is shifted about $200\,$d to earlier times compared to the original inclination plot in the paper (See Fig. 17). Therefore, it is not accurate to infer any information about the inclination of the putative planet in the TESS time from this plot. However, this does not change the the fact that, the transit due to the planet should have happened during the TESS observations.

As pointed out by Tanimoto et al. (2020), a remaining problem is that the stellar radius as derived from planetary parameter is smaller than the stellar radius derived from stellar luminosity.

As a final note, it is more plausible that the LCO dip and dip I are due to other phenomena and attributing them to a planetary transit might be a false positive. However, there is the possibility that the weak dip at phases of 0.05-0.1 (see Fig. 41) is due to a putative planet with radius of $0.22R_{\text{Jup}}$.

6.4   Are the observed dips due to a dust clump?

Another possibility for the origin of the dips is a circumstellar dust clump. As discussed in previous sections, the fact that is a young weak-lined T Tauri star that exhibits not-strictly-periodic dips with different depths and shapes, Hα emission (Yu et al. 2015; Johns-Krull et al. 2016), and wavelength-dependence transit dips (Onitsuka et al. 2017; Yu et al. 2015; Tanimoto et al. 2020), all could be supportive indications for the dust clump scenario.

In light of Tanimoto et al. (2020) analysis, which concluded that dust clump is the origin of 2 dips out of 3 different dips, our data might help to strengthens their findings or refute some of their interpretations. As mentioned earlier, Tanimoto et al. (2020) proposed that the big dip with a depth of 3.75% split into 2 shallower dips, so called dip 'A and dip 'B'. They also mentioned there exists third type of dip called 'dip C' which started to appear in November 2018 (see Fig. 9). They proposed a dust clump as the possible explanations for the 'dip A' and 'dip C' with depth ranges of $1.37\% - 2.23\%$ and 1.3%, respectively. They suggested accretion hotspot for the origin of the latter.

Comparing our data with their findings, LCO dip's depth differs from the depth of dip A and its phase -0.42 does not match the predicted phase of -0.1 for dip A (based on the Tanimoto et al. 2020, ephemeris). This holds true for the dip C as well, which has a much lower depth compared to the LCO dip, despite the fact that their phases are somehow similar.

The LCO dip has a roughly similar depth of 3.0% to the 3.7% dip before splitting. Additionally, it has a similar shape and its duration of $\approx 1.8\,\text{h}$ is somewhat consistent with the duration of 1.6 h of the big dip. However, the LCO dip occurs in January 2017, after the split in 2014 and its phase of -0.42 does not fit the zero phase of this big dip. For the TESS data, the dip I has similar depths (roughly 1.0%) to dip C and its phase of -0.45 and -0.47 (for the Raetz et al. (2016); Tanimoto et al. (2020) ephemerides respectively) matches the predicted phase of 0.5 for dip C. Furthermore, both have a similar duration of about 0.1 in phase space. Interestingly, dip I in TESS is similar to the observed dip in February 2016 with depths ranging from $1.0\% - 1.7\%$ in the infrared and red bands, respectively (Onitsuka et al. 2017). They concluded that a dust clump or an accretion hotspot is the origin of the observed dips.

There are interesting points for other short variabilities in the TESS light curve to be mentioned. Dip II in the TESS light curve at phase of 0.2 (Fig. 41) has a similar shallow shape to the dip A from Tanimoto et al. (2020) (see Fig. 15). Additionally, the fact that it has the same phase difference of roughly 0.1 to the small dip between phase of 0.05-0.1, might be another indication that it has the same origin as dip A. But its phase of 0.2 does not match the predicted phase of -0.1 of dip A. Additionally, dip A survived only until October 2017 in their observations, while the TESS data is for 2018-2019 years.

One critical point for this hypothesis is whether the dust clump could survive for more than several years at the distance of $\approx 2R_*$. Yu et al. (2015) calculated R_s, the dust-sublimation radius using the Monnier & Millan-Gabet (2002) equation and the resulted value is about $2.7R_*$. But the semi major axis of orbit of the planet or dust clump is smaller than this value and the dust clump might have evaporated. However, Tanimoto et al. (2020) argued that the semi-major axis of the dust clump orbit is larger than $2.7R_*$ and is about $3.94R_*$, based on the 2014 observations. They argued that the dust clump in this large distance might have survived between 2009 to 2012.

One problem for the split scenario is the detection of a dimming event with a depth of 0.6% in Spitzer data (Ciardi et al. 2015, See Fig. 8). This is not consistent with a split scenario, since it occurred before the split in 2012. (Tanimoto et al. 2020) argued that since the attenuation due to the dust clump is negligible in the Spitzer infrared data, this dip belongs to the planetary transit. This means the putative planet would have existed in the system since 2012. Then the question arises why the signature of this planet have not been observed in the previous observations except Ciardi et al. (2015).

Another interesting aspect related to the dust clump hypothesis, is the similarities of this system with other weak-lined T Tauri stars that exhibit quasi-periodic fading events, called *transient dipper stars* (Stauffer et al. 2015; David et al. 2017). Bouma et al. (2020) laid out a detailed overview of the similar transient dipper's light curves to the one of PTFO 8-8695. Based on the common physical features between these stars and PTFO 8-8695, they concluded this star belongs to the "persistent flux dip" subclass. However, despite the similarities between PTFO 8-8695 and these stars, there are a few problems with this hypothesis as well and it is debated whether PTFO 8-8695 belongs to this class of stars. The interesting point is, among the suggested hypothesis by Stauffer et al. (2017) for the cause of persistent flux dips, is warm gas and material clouds that have a structured shape and are located at a radius at which they co-rotate with the star. In the case of the interaction between the star and the material, it is likely that we observe H$_{alpha}$ profiles that show radial velocity shift. This has been observed in this system by Johns-Krull et al. (2016); Yu et al.

(2015). Those clouds can, among other effect, cause a complex light curve in the way we see in our light curves.

To sum it up, the dip in the LCO light curve has roughly similar properties to the big dip in the Tanimoto et al. (2020) data. However, the fact that it happens after the split event in 2014 is in contradiction with split scenario. It is possible that the split scenario is not right. Another option is that LCO dip is due to a dust clump that has disappeared before TESS observations started and is not related to the big dip that split up.

The dip I in TESS, has features that match mostly the features of dip C in the Tanimoto et al. (2020) data and the dimming events in Onitsuka et al. (2017) that have dust clumps as one of the possible origins. But one question remains: how a dust clump could survive for several years in this system ?.

6.5 Are the observed dips due to spots?

Given the young age of the this star, the possibility of existence of several and large spots on its surface is there. Additionally, the synchronization between the stellar period and period of dips might be another indication that the observed dips have a starspot or an accretion hotspot as origin. We will briefly discuss these possibilities in the following paragraphs.

6.5.1 Cool star spots

A combination of several spots with different sizes at different latitudes on the stellar surface might cause the observed quasi-periodic dips. The possibility of star spot for the origin of dips was discussed in previous studies (e.g., van Eyken et al. 2012; Yu et al. 2015; Tanimoto et al. 2020). They argued that the variation in the shape and depth of transits could be due to the gradual change in spot patterns. Additionally, dimming events caused by the star spots are wavelength dependent due to the temperature difference. However, star spots may not justify the physical properties of the dips. Mainly depth and duration were noted as reasons, which caused star spots to be ruled out as the origin of dips (e.g., van Eyken et al. 2012; Yu et al. 2015; Ciardi et al. 2015; Tanimoto et al. 2020). This reasoning appears to be very plausible and as such we will not discuss this possibility for the origin of our observed dimming events any further. However, the spot-modulation signal with rotation $P = 0.49927$ d is evident in TESS light curve and also partially in the STELLA light curve.

6.5.2 Accretion hotspot

Another possibility for the origin of the observed dips is an accretion hotspot. The complex photometric behaviors observed in T Tauri stars could be explained by a hotspot that has formed close to one of the star's magnetic poles, fueled by the on-going accretion from the disk to the star (Herbst et al. 1994). Although this is mostly the case for Classic T Tauri stars (CTTS) due to the presence of the disk in the system, PTFO 8-8695 as a Weak-lined T Tauri star with no disk, also showed signs of on-going weak accretion which strengthens the possibility of existence of accretion hotspot (Ciardi et al. 2015; Yu et al. 2015)

Consensus among the studies that considered this scenario for the observed dips (e.g., Yu et al. 2015; Onitsuka et al. 2017; Tanimoto et al. 2020) is that a high-latitude accretion hotspot can be the origin of the observed dips. Tanimoto et al. (2020) suspected 'dip C' to have an accretion hotspot as origin. As discussed before, dip I in the TESS data has similar features (depth, duration, phase) to 'dip C' and also similar depth and duration to the observed dips by Onitsuka et al. (2017) with depths of 1.7%, 1.0% in red and infrared bands, respectively. However, as mentioned by them, one concern for this scenario is the low temperature of the hotspot. The assumed temperature for the hotspot that caused dip C is less than 3800 K, and with that only 300 K hotter than the stellar temperature of 3500 K, which makes it very cool to deserve the name.

6.6 Are the observed dips due to a binary star?

As mentioned in the second chapter, Bouma et al. (2020) and Koen (2020) recently suggest a vastly different hypothesis, in which the system is in fact an eclipsing binary star system. With a complex Fourier-analysis, Bouma et al. (2020) and Koen (2020) each identified a short period signal of $P_{\mathrm{Bouma}} = 0.44844$ d, and $P_{\mathrm{Koen}} = 0.4486$ d in the TESS data, respectively. Their interpretation is as such that the derived periods are due to two stars in the system with similar luminosities and spectral types. From our data, we can just derive one argument to support this scenario. The two periods, $P_{\mathrm{Bouma}} = 0.44844$ d and $P_{\mathrm{Yu}} = 0.448438$ d, are very similar, thus we compare the phase of the observed dips based on P_{Yu} and T_0. The phase of the observed dip in the LCO light curve and dip I in TESS based on this $P_{\mathrm{Yu}} = 0.448438$ d, and $T_{0,yu}$ is about 0.02 ± 0.08 and -0.05 respectively. This might indicate that there is an object in the system with the period of 0.4484 d. But we don't know if LCO dip is caused to this object or not. Additionally, the large sinusoidal

signal that has been attributed to the binary star in the phase folded TESS light curve is located between phase 0.0 and 0.5 and has duration of $\approx 5.0\,\mathrm{h}$.

It is not scientifically possible to rule out or consider this possibility for the origin of dips due to the limitation of results.

However, it is not clear how the dip due to the binary star could disappear for sometime since the eclipse due to the binary star is periodic. Additionally, Koen (2020) argued that the if the observed periodicities in the system are due to two T Tauri stars, then both probably show Hα emission. However, Johns-Krull et al. (2016) showed that the Hα emission observed from the system disappeared for sometime in between. It is not clear how the Hα emission from both stars could disappear at the same time. This along with the disappearance of the dips in previous papers, might cast doubt on the existence of another T Tauri star in the system.

7 Conclusion

In this study, we investigated the mysterious system PTFO 8-8695, a young T Tauri star whose curious photometric variability has puzzled scientists for almost a decade. Studies have failed to produce a conclusive explanation for all light curve features. We analyzed the data collected by ground-based telescopes, STELLA and LCO, and archival data obtained by TESS and showed that there exist different dips in the system at different phases.

Thanks to the high quality of the TESS data, we identified several different dips in the light curve of the system. The identified dips show some similarities with the several dips reported by Tanimoto et al. (2020) for which they used five years of ground-based photometric monitoring.

We investigated the possibility of the existence of PTFO 8-8695b in the system by transit modeling on the LCO dip and found a similar radius ratio to the derived parameter in Raetz et al. (2016). By timing analysis on all of the dips with available ephemerides in the literature, we showed that the phases of the dips in LCO and TESS data are roughly shifted by about half a period from the reported dips in the literature. We discussed different explanations for each of the observed dips and small variabilities.

The phase jump of the LCO dip, the non-existence of the similar dip in the TESS data, the non-detection of several effects such as secondary eclipse, the so-called Rossiter-McLaughlin effect, and the sky-projected rotation rate ($v \sin i_*$) in previous papers, all together show that the existence of a hot Jupiter in the system is not very plausible. However, the small signal in the TESS data between the phase of $0.05 - 0.1$ can be due to a close-in planet in the system. A candidate would be a Hot Neptune with the radius of $0.22\,R_{\mathrm{Jup}}$ and the other derived parameters of Tanimoto et al. (2020).

Confirming its existence requires additional high-quality data due to the weak nature of the signal. However, we can not rule out its existence in the system based on our data.

Throughout the discussion for each of the observed variabilities in the TESS light curve and the LCO dip, we have seen that none of the proposed explanations can explain the observed variabilities to a full extent. However, there are similarities between the LCO dip and those that are attributed to dust clumps. We also see that dip I in the TESS data has some similarities with one of the dips presented in Tanimoto et al. (2020). It has been attributed to dust clump or accretion hotspot. We find that the explanation given by Bouma et al. (2020) for the transient dips, appears to be the most reasonable. They suggest that PTFO 8-8695 probably belongs to the so-called transient dipper stars. Such a star experiences the occultation by warm gas clouds with a structured shape that are co-rotating with the star (e.g., Stauffer et al. 2017). This scenario is capable of explaining the observed complex dips. Further, it is flexible enough to explain the change in the shapes, depths, and the disappearance of dips.

At this point, we have no further evidence which may be used for greater clarification regarding the nature of this system. We cannot say with certainty if this system belongs to the transient dipper stars despite the similarities mentioned by Bouma et al. (2020) conclusively.

Interferometric observations to image the system at very high spatial resolution will shed light on its nature. Additionally, combining interferometry with radial velocity measurements will likely prove helpful as well. Obtaining more information about Weak-lined T Tauri stars, especially those that are in the later stages of disk evolution will help to reveal the true nature of PTFO 8-8695. The same is true for knowledge regarding transient dipper stars. Also, it would be interesting to investigate whether warm gas clouds have the required physical properties, such as density, size or temperature to stay in shape so close to the star for several years. Only then, they would be able to cause the periodic dips in a way we see in PTFO 8-8695 and other similar systems. However, it is unlikely that PTFO 8-8695 will play a role in research into planet formation scenarios in the future.

References

Alibert, Y. & Helled, R. 2015, Disk Instability, Model for Giant Planet Formation, ed. M. Gargaud, W. M. Irvine, R. Amils, I. Cleaves, Henderson James (Jim), D. L. Pinti, J. C. Quintanilla, D. Rouan, T. Spohn, S. Tirard, & M. Viso, 658–658

Baraffe, I., Chabrier, G., Allard, F., & Hauschildt, P. H. 1998, A&A, 337, 403

Barnes, J. W., van Eyken, J. C., Jackson, B. K., Ciardi, D. R., & Fortney, J. J. 2013, ApJ, 774, 53

Boss, A. P. 1997, Science, 276, 1836

Bouma, L. G., Winn, J. N., Ricker, G. R., et al. 2020, AJ, 160, 86

Briceño, C., Calvet, N., Hernández, J., et al. 2005, AJ, 129, 907

Briceno, C., Calvet, N., Hernandez, J., et al. 2018, arXiv e-prints, arXiv:1805.01008

Chauvin, G., Lagrange, A. M., Dumas, C., et al. 2005, A&A, 438, L25

Ciardi, D. R., van Eyken, J. C., Barnes, J. W., et al. 2015, ApJ, 809, 42

David, T. J., Petigura, E. A., Hillenbrand, L. A., et al. 2017, ApJ, 835, 168

Dawson, R. I. & Johnson, J. A. 2018, ARA&A, 56, 175

Fischer, D. A., Howard, A. W., Laughlin, G. P., et al. 2014, in Protostars and Planets VI, ed. H. Beuther, R. S. Klessen, C. P. Dullemond, & T. Henning, 715

Gaia Collaboration. 2018, VizieR Online Data Catalog, I/345

Herbst, W., Herbst, D. K., Grossman, E. J., & Weinstein, D. 1994, AJ, 108, 1906

Hernández, J., Calvet, N., Briceño, C., et al. 2007, ApJ, 671, 1784

Jenkins, J. M., Twicken, J. D., McCauliff, S., et al. 2016, in Software and Cyberinfrastructure for Astronomy IV, ed. G. Chiozzi & J. C. Guzman, Vol. 9913, International Society for Optics and Photonics (SPIE), 1232 – 1251

Johns-Krull, C. M., Prato, L., McLane, J. N., et al. 2016, ApJ, 830, 15

Koen, C. 2020, MNRAS, 494, 4349

Kounkel, M., Covey, K., Suárez, G., et al. 2018, AJ, 156, 84

Kurucz, R. L. 2014, Model Atmosphere Codes: ATLAS12 and ATLAS9 (Springer), 39–51

Lissauer, J. J. 1993, ARA&A, 31, 129

Lovis, C. & Fischer, D. 2010, Radial Velocity Techniques for Exoplanets, ed. S. Seager (University of Arizona Press), 27–53

Mao, S. & Paczynski, B. 1991, ApJ, 374, L37

Mayor, M. & Queloz, D. 1995, Nature, 378, 355

McGinnis, P. T., Alencar, S. H. P., Guimarães, M. M., et al. 2015, A&A, 577, A11

Monnier, J. & Millan-Gabet, R. 2002, in American Astronomical Society Meeting Abstracts, Vol. 201, American Astronomical Society Meeting Abstracts, 93.14

Onitsuka, M., Fukui, A., Narita, N., et al. 2017, PASJ, 69, L2

Pál, A. 2008, MNRAS, 390, 281

Pollack, J. B., Hubickyj, O., Bodenheimer, P., et al. 1996, Icarus, 124, 62

Raetz, S., Schmidt, T. O. B., Czesla, S., et al. 2016, MNRAS, 460, 2834

Safronov, V. S. 1972, Evolution of the protoplanetary cloud and formation of the earth and planets.

Schmidt, T. O. B., Neuhäuser, R., Briceño, C., et al. 2016, A&A, 593, A75

Siess, L., Dufour, E., & Forestini, M. 2000, A&A, 358, 593

Sing, D. K. 2010, A&A, 510, A21

Skrutskie, M. F., Cutri, R. M., Stiening, R., et al. 2006, AJ, 131, 1163

Stauffer, J., Cody, A. M., McGinnis, P., et al. 2015, AJ, 149, 130

Stauffer, J., Collier Cameron, A., Jardine, M., et al. 2017, AJ, 153, 152

Strassmeier, K. G., Granzer, T., Weber, M., et al. 2004, Astronomische Nachrichten, 325, 527

Tanimoto, Y., Yamashita, T., Ui, T., et al. 2020, PASJ, 72, 23

van Eyken, J. C., Ciardi, D. R., von Braun, K., et al. 2012, ApJ, 755, 42

Wolszczan, A. & Frail, D. 1992, Nature, 355, 145

Wolszczan, A. & Frail, D. A. 1992, Nature, 355, 145

Yu, L., Winn, J. N., Gillon, M., et al. 2015, ApJ, 812, 48

Zhou, G., Huang, C. X., Bakos, G. Á., et al. 2019, AJ, 158, 141

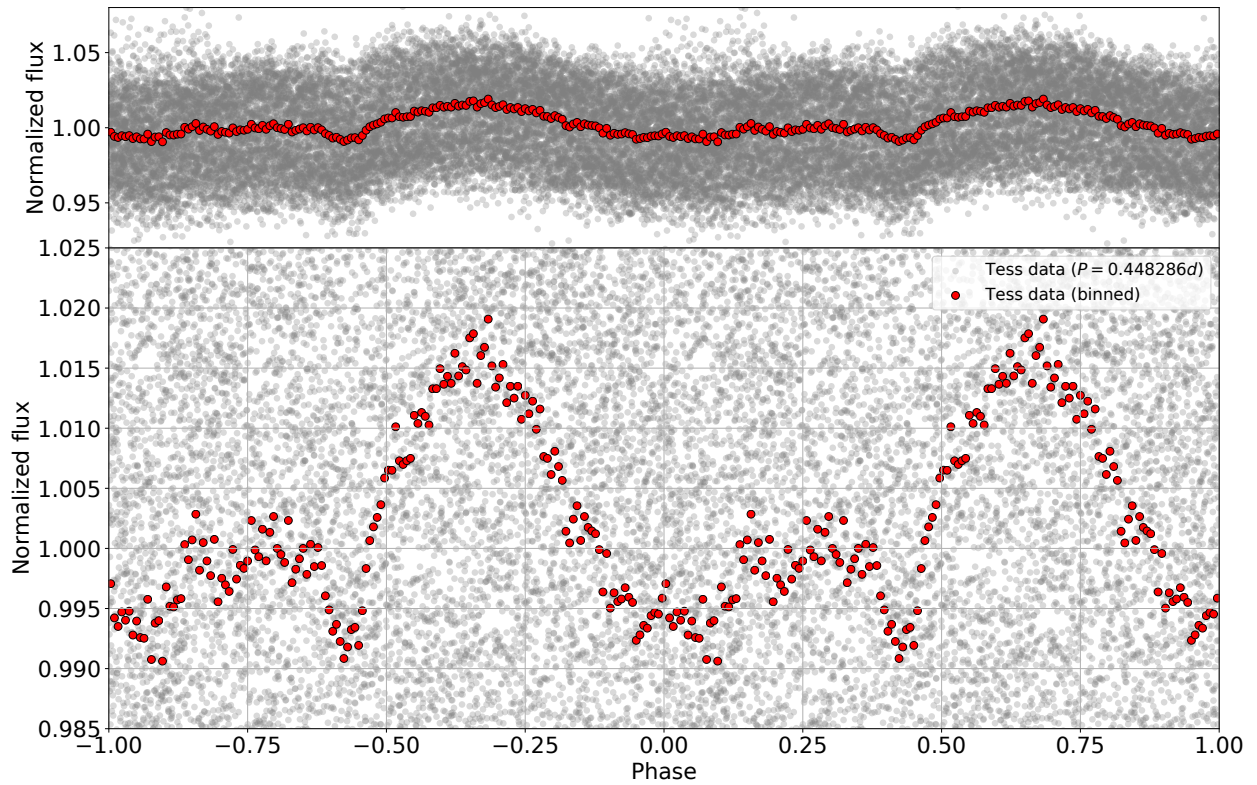# A Phasefolded light curves

Figure A.1: The phase folded TESS light curve based on the Yu et al. (2015) ephemeris. Data and color coding as in Fig. 39.
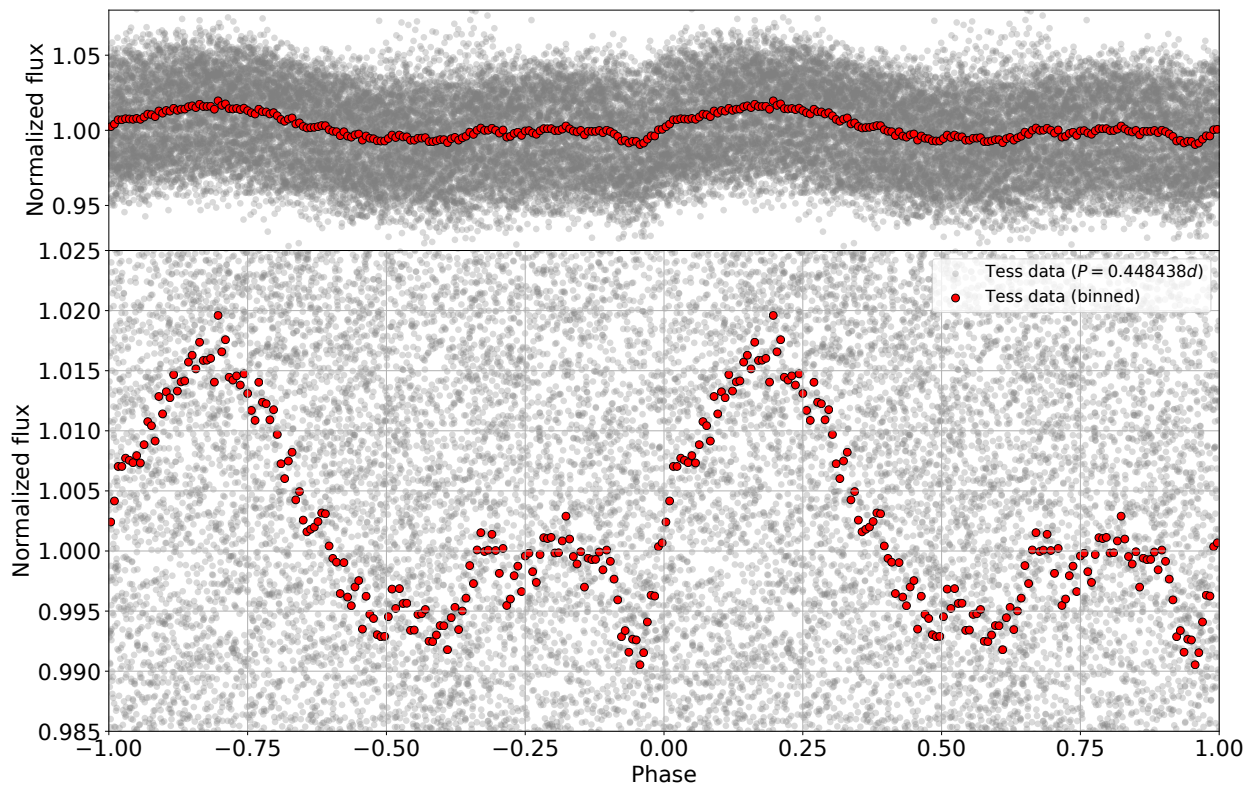

Figure A.2: Phase folded and binned light curve with the period of 0.448438d derived by (Yu et al. 2015). Data and color coding as in Fig. 39.
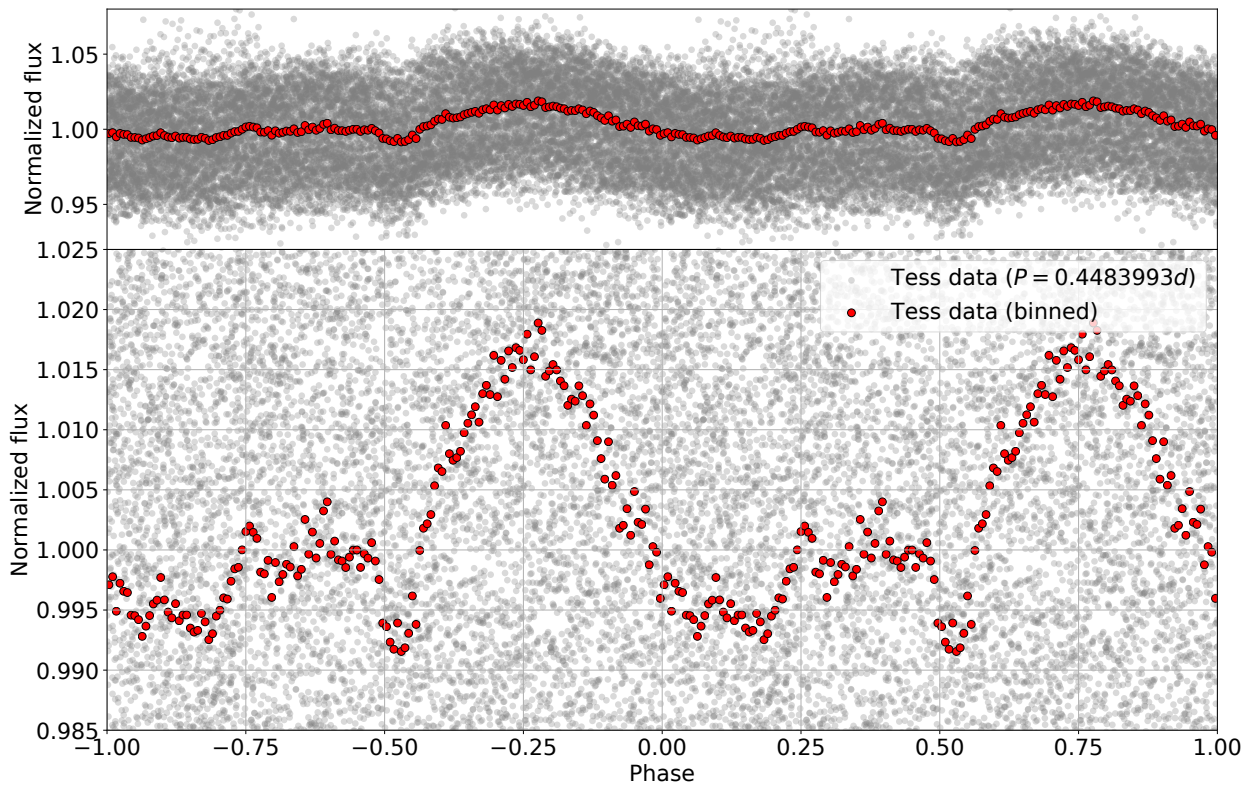
Figure A.3: Phase folded and binned light curve with the period of 0.4483993 d derived by (Tanimoto et al. 2020). Data and color coding as in Fig. 39.

B Deutsche Zusammenfassung

Heiße Jupiter machen etwa 10% aller heute nachgewiesenen Planeten aus. Ein solcher heißer Jupiter erhält seinen Namen einerseits durch seine Natur als Gasriese, ganz ähnlich dem im Sonnensystem hemischen Jupiter und andererseits durch seine extreme Näehe zum Zentralstern, dessen Strahlung ihn aufheizt. Vieles ist unklar über die Art und Weise, auf die sich diese Planeten formen. Insbesondere die Zeitskalen der Entwicklung geben Räetsel auf. Das Studium von heißen Jupitern in sehr jungen Sternsystemen erlaubt Einblicke in die frühen Jahren eines solchen Planeten und fördert unser Verständnis von Planetenentstehung.

Ein solches Studium ist Zentrum dieser Arbeit. Der sehr junge Vor-Hauptreihenstern PTFO-8695 aus der nahe gelegenen Orion OB1 Sternengruppe weißt in seinem Helligkeitsprofil Verdunklungen auf, die einem potentiellen heißen Jupiter, PTFO 8-8695 b, der etwa fünfmal schwerer ist als unser Jupiter, zugesprochen werden. Allerdings ist die tatsächliche Existenz dieses Planeten umstritten. Gelänge es, die Existenz nachzuweisen, erlaube dies ein besseres Verständnis der Entwicklungszeiträume von Gasriesen.

Wir präsentieren in unserer Arbeit neu aufgenommene und partiell unveröffentlichte Daten des STELlar Activity telescope (STELLA) and the Las Cumbres Observatory (LCO), die jeweils Lichtkurven des Sterns aufgenommen haben. Dies kombinieren wir mit Daten des Transiting Exoplanet Survey Satellite (TESS) und den gesammelten Erkenntnissen vergangener Studien um ein möglichst umfassendes Bild zu erhalten.

Dazu nutzen wir Transitmodellierung um eine Bedeckung des Zentralsterns durch PTFO 8-8695b zu simlulieren. Hierbei greifen wir auf Parameter zurück, die in früheren Studien abgeleitet wurden. Des Weiteren füheren eine Analyse der zeitlichen Abläufe und Ereignisse in den Lichtkurven durch.

Die Analyse ergibt, dass der Transit in den LCO Daten ähnlich ist zu denen, die in früheren Arbeiten zu diesem System beobachtet wurden. Es zeigt sich aber, dass der beobachtete hypthetische planetare Transit etwa eine halbe Phase verschoben ist gegenüber jenen früheren Beobachtungen, basieren auf der angenommenen Umlaufperiode.

Ein detaillierte Analyse der TESS Daten, die ersten Daten, die überhaupt mehrere vollsändinge Zyklen umfassenden Einblick liefern, legt offen, dass das System diverse Verdunklungen aufweist und deutlich komplexer als angenommen. Diese Transits weisen ein weites Spektrum an Verdunklungsgraden und Verdunklungsdauern auf. Es zeigt sich aber, dass einer dieser Transits mit der Phase des in LCO beobachteten zusammenfällt. Allerdings stimme beide Transits weder in Form, noch in Dauer, noch in Tiefe überein.

Die Phasenverschiebung zwischen den in zuvor berichteten Transits und denen, die wir in den LCO und TESS Daten beobachten legt, zusammen mit dem Fehlen von jedweden anderweitigen konkreten Hinweis auf einen Planeten um PTFO 8-8695, nahe, dass ein solcher Planet nicht existiert.

Abschließend stellen wir noch die verschiedenen alternative Erklärungsmöglichkeiten für die Beobachteten Helligkeitsveränderungen des Sterns gegeneinandern und diskutieren sie hinsichtich ihrer Plausibilität und Fähigkeit die Beobachtungen zu erklären. Dazu zählen unter anderem Szenarios, nach denen die beobachteten Effekte durch Gaswolken, Sternenflecken oder Gasakkretion verursacht werden. Auch die Existenz eines potentiellen Doppelsterns werden kurz diskutiert. Wir stellen fest, dass keine der vorgeschlagenen Szenarien alle Beobachtungen umfassend erklären kann. Das wahrscheinlichste Szenario, basierend auf den uns vorliegenden Daten, ist eine mit dem Stern ko-rotierende Gaswolke. Es ist unwahrscheinlich, dass PTFO 8-8695 zukünftig eine Rolle in der Forschung bezüglich Planetentstehung spielen wird.

Selbstständigkeitserklärung

Hiermit versichere ich, dass ich die vorliegende Masterarbeit ohne fremde Hilfe angefertigt und keine anderen als die angegebenen Quellen und Hilfsmittel benutzt habe. Alle Teile, die wörtlich oder sinngemäß einer Veröffentlichung entstammen, sind als solche kenntlich gemacht. Die Arbeit wurde noch nicht veröffentlicht oder einer anderen Prüfungsbehörde vorgelegt.

Potsdam, den ...29.04.202...
1

....
(Unterschrift)